TAMPEREEN TEKNILLINEN YLIOPISTO
TAMPERE UNIVERSITY OF TECHNOLOGY

Tuomas Messo

Factors Affecting Stable Operation of Grid-Connected Three-Phase Photovoltaic Inverters

Julkaisu 1227 • Publication 1227

Tampere 2014

Tampereen teknillinen yliopisto. Julkaisu 1227
Tampere University of Technology. Publication 1227

Tuomas Messo

Factors Affecting Stable Operation of Grid-Connected Three-Phase Photovoltaic Inverters

Thesis for the degree of Doctor of Science in Technology to be presented with due permission for public examination and criticism in Sähkötalo Building, Auditorium S2, at Tampere University of Technology, on the 12th of September 2014, at 12 noon.

Tampereen teknillinen yliopisto - Tampere University of Technology
Tampere 2014

ISBN 978-952-15-3325-9 (printed)
ISBN 978-952-15-3377-8 (PDF)
ISSN 1459-2045

ABSTRACT

The amount of grid-connected photovoltaic energy generation has grown enourmously since the beginning of the 21st century. Photovoltaic power plants are interfaced with the utility grid by using three or single-phase inverters which convert the direct current generated by the photovoltaic modules into three or single-phase alternating current. The photovoltaic inverters have been observed to degrade power quality in the grid and to suffer from reliability problems related to their control software. Therefore, the design of these inverters has become a significant research topic in academia and in the power electronic industry.

Control design of a photovoltaic inverter is often based on the small-signal models characterizing its dynamic behavior. In this thesis, the existing small-signal models are upgraded to include the effect of an upstream DC-DC converter and its control mode. In addition, the models are upgraded to include the effect of a phase-locked-loop which is often used as a synchronization method and the effect of the grid-voltage feedforward which is often used to improve the transient performance.

The control mode of the upstream DC-DC converter is shown to have a significant effect on the minimum DC-link capacitance which is required for stable operation due to a RHP-pole in the inverter control dynamics. However, operating the DC-DC converter under input-voltage control is shown to remove the RHP-pole and, consequently, the constraint imposed on the size of the minimum DC-link capacitance.

The phase-locked-loop (PLL) is shown to make the q-component of the inverter's output impedance resemble a negative resistor. Based on the small-signal models, the negative resistance is shown to appear at the frequencies below the crossover frequency of the PLL. Therefore, a wide-bandwidth PLL causes easily instability due to the negative-resistance behavior when the grid inductance is large.

The grid-voltage feedforward is shown to increase the magnitude of both the d and q-components of the inverter's output impedance. The PV inverter with grid-voltage feedforward is shown to be more resistant against impedance-based interactions than an inverter without the feedforward.

PREFACE

The work was carried out at the Department of Electrical Engineering at Tampere University of Technology (TUT) during the years 2011 - 2014. The research was funded by TUT and ABB Oy. Grants from Fortum Foundations, Ulla Tuominen Foundation and Walter Ahlström Foundation are greatly appreciated.

I thank Professor Teuvo Suntio for supervising my thesis and for the guidance throughout the journey toward the doctoral degree. Without his support a lot of interesting phenomena related to the research would have stayed hidden. I also want to thank all the colleaques who have influenced in my doings during the years, PhD Joonas Puukko, PhD Juha Huusari, PhD Lari Nousiainen, PhD Jari Leppäaho, PhD Anssi Mäki, M.Sc. Diego Torres Lobera, M.Sc. Juha Jokipii, M.Sc. Jukka Viinamäki, M.Sc. Kari Lappalainen, M.Sc. Jenni Rekola, B.Sc. Aapo Aapro and B.Sc. Jyri Kivimäki. Without the help of the aforementioned persons this thesis would have only empty pages. The research could not have been carried out without the help of a team of true experts who are devoted to their work and equipped with endless thirst of understanding on how the world around us works. A big thanks goes to Professors Lennart Harnefors, Marko Hinkkanen and Pedro Roncero for examining and criticising my thesis. I thank Pentti Kivinen and Pekka Nousiainen for using their craftmanship in building countless racks and prototypes. I also want to express my gratitude to Merja Teimonen, Terhi Salminen, Mirva Seppänen and Nitta Laitinen for making my work easier by taking care of the practical everyday matters.

I want to thank my parents Pauli and Kristiina, my sister Maria and my brother Markus for encouraging me to finalize the doctoral degree. Moreover, members of the band Herrakerho deserve special thanks for giving me something else to think about besides work. Finally, I want to thank my fiancée Karoliina for being there when I needed support and for having patience when I was finalizing the thesis.

Tampere, June 2014

Tuomas Messo

SYMBOLS AND ABBREVIATIONS

ABBREVIATIONS

A/D	Analog-to-digital converter
AC	Alternating current
CC	Constant current, current controller
CV	Constant voltage
CSI	Current-source inverter
D/A	Digital-to-analog converter
DC	Direct current
DC-DC	DC to DC converter
DC-AC	DC to AC converter
Dr. Tech.	Doctor of Technology
DSP	Digital signal processor
FRA	Frequency-response analyzer
GW	Gigawatt
M.Sc.	Master of science
MPP	Maximum power point
MPPT	Maximum power point tracker
NPC	Neutral-point-clamped
p.u.	Percent unit
PC	Personal computer
PI	Proportional-integral controller
PLL	Phase-locked-loop
PV	Photovoltaic
PVG	Photovoltaic generator
Prof.	Professor
RHP	Right-half of the complex plane
SAS	Solar array simulator
sw	Power electronic switch
TW	Terawatt
U.S.	United States of America
VC	Voltage controller
VSI	Voltage-source inverter

GREEK CHARACTERS

Δ	Determinant of a transfer function
d_α	Alpha-component of the duty ratio
d_β	Beta-component of the duty ratio

Δi_{pv}	Current perturbation around a specific operating point
$\langle i_{\mathbf{L}\alpha} \rangle$	Alpha-component of the inductor current
$\langle i_{\mathbf{L}\beta} \rangle$	Beta-component of the inductor current
Δu_{pv}	Voltage perturbation around a specific operating point
x_α	Alpha-component of a space-vector
x_β	Beta-component of a space-vector
ω_{s}	Angular frequency of the grid
θ_{c}	Phase angle of the control system reference frame
θ_{g}	Phase angle of the grid reference frame
θ_Δ	Angle between two reference frames
Θ	Steady-state angle difference

LATIN CHARACTERS

A	Diode ideality factor
A	Coefficient matrix A of the state-space representation, Connection point for phase A inductor
B	Coefficient matrix B of the state-space representation, Connection point for phase B inductor
C	Coefficient matrix C of the state-space representation, Connection point for phase C inductor
C_1	Capacitance of the DC-DC converter input capacitor
C_{dc}	Capacitance of the DC-link capacitor
C_{f}	Capacitance of the three-phase output filter
d	Differential operator
$\hat{d}$	Small-signal duty ratio of the DC-DC converter
$\boldsymbol{d}$	Duty ratio space-vector
$\boldsymbol{d}^{\mathbf{s}}$	Duty ratio space-vector in synchronous frame
d_{a}	Duty ratio of the upper switch in phase A
d_{b}	Duty ratio of the upper switch in phas B
d_{c}	Duty ratio of the upper switch in phase C
d_{d}	Direct component of the duty ratio space-vector
$\hat{d}_{\mathrm{d}}$	Small-signal d-component of the duty ratio space-vector
d_{q}	Quadrature component of the duty ratio space-vector
$\hat{d}_{\mathrm{q}}$	Small-signal q-component of the duty ratio space-vector
d'	Complementary duty ratio of the DC-DC converter
D	Coefficient matrix D of the state space representation, diode of the DC-DC converter
D_{d}	Steady-state d-component of the duty ratio
D_{q}	Steady-state q-component of the duty ratio
D'	Steady-state complementary duty ratio

$\mathbf{G}$	Transfer function matrix
G_{cd},G_{cq}	Current controller transfer functions
G_{ci}	Control-to-input transfer function
G_{co}	Control-to-output transfer function
G_{c},G_{cv}	Voltage controllers
$G_{\text{ff-d}}$,$G_{\text{ff-q}}$	Feedforward gains
G_{PWM}	Pulse-width-modulator gain
G_{io}	Input-to-output transfer function
H_{d},H_{q}	Current sensing transfer functions
H_{v},$H_{\text{v-dc}}$	Voltage sensing gains
$i_{\mathrm{i=a,b,c}}$	Current of phase a, b or c
I_0	Dark saturation current
i_{C1}	Capacitor C_1 current
$i_{\text{C-dc}}$	DC-link capacitor current
i_{d}	Current of the diode in the one-diode model
i_{dc}	DC-DC converter output current, inverter input current
$\hat{i}_{\mathrm{dc}}$	Small-signal DC-DC converter output/inverter input current
I_{dc}	Steady-state inverter input current
i_{in}	Input current
$\langle \boldsymbol{i}^{\mathbf{s}}_{\mathbf{L}} \rangle$	Inductor current space-vector in synchronous frame
$\hat{i}_{\mathrm{L1}}$	Small-signal inductor L_1 current
$\langle \boldsymbol{i}_{\mathbf{L}} \rangle$	Inductor current space-vector
i_{La}	Inductor L_{a} current
$\langle i_{\mathrm{La}} \rangle$	Average inductor L_{a} current
i_{Lb}	Inductor L_{b} current
$\langle i_{\mathrm{Lb}} \rangle$	Average inductor L_{b} current
i_{Lc}	Inductor L_{c} current
$\langle i_{\mathrm{Lc}} \rangle$	Average inductor L_{c} current
$\langle i_{\mathrm{Ld}} \rangle$	Average d-component of the inductor current space-vector
$\hat{i}_{\mathrm{Ld}}$	Small-signal d-component of the inductor current space-vector
I_{Ld}	Steady-state d-component of the inductor current
$\langle i_{\mathrm{Lq}} \rangle$	Average q-component of the inductor current space-vector
$\hat{i}_{\mathrm{Lq}}$	Small-signal q-component of the inductor current space-vector
I_{Lq}	Steady-state q-component of the inductor current
I_{L1}	Steady-state inductor L_1 current
I_{MPP}	Current at the maximum power point
i_{o}	Output current
$\langle i_{\text{o-d}} \rangle$	Average d-component of the output current space-vector
$\hat{i}_{\mathrm{od}}$	Small-signal d-component of the output current space-vector
$\langle i_{\text{o-q}} \rangle$	Average q-component of the output current space-vector

$\hat{i}_{\mathrm{oq}}$	Small-signal q-component of the output current space-vector
i_{P}	Current flowing from the DC-link toward the inverter switches
$\langle i_{\mathrm{P}} \rangle$	Average current flowing toward the inverter switches
i_{ph}	Photocurrent
$\hat{i}_{\mathrm{pv}}$	Small-signal output current of the photovoltaic generator
i_{pv}	Output current of the photovoltaic generator
I_{pv}	Steady-state output current of the photovoltaic generator
I_{sc}	Short-circuit current of the photovoltaic generator
j	Imaginary part
K	Scaling factor related to space-vector transformation
k_{i}	Scaling factor related to cloud enhancement
L	Inductance of the inverter when all phases are symmetrical
L_1	Inductance of the DC-DC converter
L_{a}	Inductance of phase A of the inverter
L_{b}	Inductance of phase B of the inverter
L_{c}	Inductance of phase C of the inverter
L_{d}	Ratio of the impedance d-components
L_{dc}	DC-link voltage control loop gain
L_{f}	Inductance of the three-phase filter
$L_{\text{out-d}}$	Current control loop gain of the d-component
$L_{\text{out-q}}$	Current control loop gain of the q-component
L_{PLL}	Control loop gain of the phase-locked-loop
L_{q}	Ratio of the impedance q-components
n	Neutral point
N	Negative rail of the DC-link
P	Positive rail of the DC-link
P_{MPP}	Power at the maximum-power point
p_{pv}	Instantaneous output power of the photovoltaic generator
R_1	Equivalent resistance related to the DC-DC converter
R_2	Equivalent resistance related to the inverter
r_{C1}	Parasitic resistance of capacitor C_1
$r_{\text{C-dc}}$	Parasitic resistance of the DC-link capacitor
r_{D}	Parasitic resistance of a diode
R_{d}	Damping resistance
r_{L1}	Parasitic resistance of inductor L_1
r_{La}	Parasitic resistance of inductor L_{a}
r_{Lb}	Parasitic resistance of inductor L_{b}
r_{Lc}	Parasitic resistance of inductor L_{c}
r_{pv}	Dynamic resistance of the photovoltaic generator
r_{s}	Series resistance in the one-diode model

r_{sh}	Shunt resistance in the one-diode model
r_{sw}	Parasitic resistance of the DC-DC converter switch sw
s	Laplace variable
$\hat{\mathrm{u}}$	Column-vector containing input variables
$\mathbf{U}$	Input-variable vector in Laplace-domain
u_{a}	Voltage of phase A
$\langle u_{\mathrm{a}} \rangle$	Average voltage of phase A
$\langle u_{\mathrm{AN}} \rangle$	Average voltage between points A and N
u_{b}	Voltage of phase B
$\langle u_{\mathrm{b}} \rangle$	Average voltage of phase B
$\langle u_{\mathrm{BN}} \rangle$	Average voltage between points B and N
u_{c}	Voltage of phase C
$\langle u_{\mathrm{c}} \rangle$	Average voltage of phase C
$\langle u_{\mathrm{CN}} \rangle$	Average voltage between points C and N
$\hat{u}_{\mathrm{C1}}$	Small-signal voltage over the capacitor C_1
u_{C1}	Voltage over the capacitor C_1
$u_{\mathrm{C\text{-}dc}}$	DC-link capacitor voltage
$\hat{u}_{\mathrm{C\text{-}dc}}$	Small-signal DC-link capacitor voltage
$U_{\mathrm{C\text{-}dc}}$	Steady-state DC-link capacitor voltage
U_{C1}	Steady-state voltage over the capacitor C_1
$u_{\mathrm{i=a,b,c}}$	Three-phase grid voltages
u_{d}	Voltage over a diode in the one-diode model
U_{D}	Diode threshold voltage
$\hat{u}_{\mathrm{dc}}$	Small-signal DC-link voltage
$\langle u_{\mathrm{dc}} \rangle$	Average DC-link voltage
u_{dc}	Instantaneous DC-link voltage
U_{dc}	Steady-state DC-link voltage
$\langle \boldsymbol{u}_{\mathbf{g}} \rangle$	Grid voltage space-vector
$\langle \boldsymbol{u}_{\mathbf{g}}^{\mathbf{s}} \rangle$	Grid voltage space-vector in synchronous frame
u_{in}	Input voltage
$u_{\mathrm{i\text{-}d}}^{\mathrm{ref}}$	Reference of the output current d-component
$\langle \boldsymbol{u}_{\mathbf{L}} \rangle$	Inductor voltage space-vector
u_{La}	Voltage over the inductor L_{a}
$\langle u_{\mathrm{La}} \rangle$	Average voltage over the inductor L_{a}
$\langle u_{\mathrm{Lb}} \rangle$	Average voltage over the inductor L_{b}
$\langle u_{\mathrm{Lc}} \rangle$	Average voltage over the inductor L_{c}
u_{L1}	Voltage over the inductor L_1
U_{MPP}	Voltage at the maximum power point
$\langle u_{\mathrm{nN}} \rangle$	Average common-mode voltage
u_{o}	Output voltage

U_{oc}	Open-circuit voltage of the photovoltaic generator
U_{od}	Steady-state d-component of the grid voltage
$\hat{u}_{\mathrm{od}}$	Small-signal d-component of the grid voltage
U_{oq}	Steady-state q-component of the grid voltage
$\hat{u}_{\mathrm{oq}}$	Small-signal q-component of the grid voltage
u_{pv}	Voltage accross the photovoltaic generator terminals
U_{pv}	Steady-state voltage of the photovoltaic generator
U_{th}	Diode threshold voltage
t	Time
T_{oi}	Open-loop output-to-input transfer function
$\boldsymbol{x}$	Space-vector
$\boldsymbol{x}^{\mathrm{s}}$	Space-vector in a synchronous reference frame
x_0	Zero component of a space-vector
x_{a}	Variable related to phase A
x_{b}	Variable related to phase B
x_{c}	Variable related to phase C
x_{d}	Direct component of a space-vector
x_{q}	Quadrature component of a space-vector
$\hat{\mathrm{y}}$	Vector containing output variables
$\mathbf{Y}$	Output-variable vector in Laplace-domain
Y_{o}	Output admittance
Z_{in}	Input impedance

SUBSCRIPTS

c	Closed-loop transfer function
d	Transfer function related to d-components
dq	Transfer function from d to q-component
f	Variable related to the three-phase filter
inL	Variable related to input terminal of a load system
inS	Variable related to input terminal of a source system
inv	Transfer function related to the inverter
L	Variable related to load
off	Current or voltage during off-time
o	Open-loop transfer function
oL	Variable related to output of a load system
oS	Variable related to output of a source system
on	Current or voltage during on-time
q	Transfer function related to q-components
qd	Transfer function from q to d-component
S	Variable related to source

SUPERSCRIPTS

$*$	Complex conjugate of a space-vector
-1	Inverse of a matrix or a transfer function
c	Variable in the control system reference frame
cc	Transfer function which includes the effect of current control
CL	DC-DC converter operates at closed loop
DC-DC	Transfer function related to the DC-DC converter
DC-AC	Transfer function related to the inverter
ff	Transfer function includes the effect of feedfoward
g	Variable in the grid reference frame
LP	Transfer function includes the effect of low-pass filter
OL	DC-DC converter operates at open loop
ref	Reference value

CONTENTS

1 INTRODUCTION

This chapter provides essential background for the topics discussed in this thesis at general level and discusses on the motivation of the research topics. A short introduction to renewable energy is given, the special properties of a photovoltaic generator are shortly discussed, and the basic power converter topologies used in grid-interfacing of photovoltaic electricity are reviewed. Short literature review on the current research topics related to photovoltaic inverters is presented. The main scientific contributions of the thesis are summarized, and the author's contribution to the papers in which the ideas presented in this thesis are published, is specified.

1.1 Climate change and renewable energy

The quality of life experienced today requires reliable and continuous supply of electrical energy. The electrical energy is consumed in commodities such as, food production, heating and transportation but also in products such as laptops and smart phones, just to name a few. Irresponsible consumption of non-renewable primary energy has led to unforeseen effects such as global warming and climate change that are argued to have a negative effect on our life on Earth.

The global warming effect stands for the rise of the average global temperature which has been observed to change the climate on our planet. According to worst-case scenarios, this may lead to excessive droughts, rise of the sea-level and cause loss of vegetation (Bose, 2010). The average temperature has been increasing ever since the industrial revolution in the 18th century when the wide utilization of fossil fuel reserves, such as oil, natural gas and coal, started. Just a few decades ago there was still a disagreement among the researchers whether the global warming is caused by our actions or not. However, at the present there seems to be a common understanding that the burning of fossil fuels is the main reason to the global warming.

The problem with the fossil fuels is not just the global warming effect but also their limited reserves. The known coal reserves are estimated to last approximately from 130 to 200 years, oil reserves from 42 to 100 years and natural gas approximately 60 years. The known uranium reserves used in nuclear reactors will run out just in 50 to 80 years with the current consumption, i.e., in the lifetime of the current generation as discussed, e.g., in Bose (2013) and Abbott (2010). In other words, we are depleting the resources

which once seemed to be abundant on our planet.

Therefore, it should be of utmost importance to promote renewable energy technologies that do not use the fossil fuels. After all, oil for example is needed in various other processes that are essential in energy production, such as in lubricants that are required by generators.

Renewable energy sources include hydro, wind and solar energy in electrical and thermal form. Although, solar thermal energy might prove to be the only source of renewable energy that makes sense in the long run, as discussed in Abbott (2010), all the renewable energy sources are important, especially, during the transition period from fossil fuel-based economy to a sustainable one. The amount of total renewable energy generation has doubled since the beginning of the century, i.e., between the years 2000 and 2012 as discussed in the report of U.S. Department of Energy (Gelman, 2012). The amount of installed wind power grew by a factor of 16 and the installed amount of solar power by a factor of as large as 49. Currently, approximately 23 percent of all electrical energy worldwide is produced using renewable sources which is a positive sign. Utilization of wind and solar energy has maintained a steady growth in the past few years. The global leader in solar energy generation at the moment is Germany with a total of 32.4 GW peak power. However, there are still a lot of technological and political issues to be solved before the renewable energy sources can be fully exploited.

The most desirable feature of solar power is its natural abundance. For comparison, most of the available suitable sites for hydro energy (dams, tidal energy, etc.) are already occupied which effectively prevents its large-scale utilization in global energy production. On the other hand, the whole worlds's power demand today (approx. 15 TW) could be met simply by covering an area of 100 km by 100 km with solar cells which have an efficiency of 20 percent (Abbott, 2010). The irradiance arriving from the sun is clearly a tremendous source of energy which should be exploited to meet the requirements of a sustainable economy of the future.

1.2 Properties of a photovoltaic generator

Photovoltaic cell is a silicon-based device which converts irradiance directly into an electrical current. The process is called photovoltaic effect and was first discovered by a French physicist Alexandre-Edmond Becquerel in 1839. The output current of a modern mono-crystalline PV cell is approximately 8 amperes. The output voltage of a PV cell is less than one volt which is not high enough for most electronic loads and, especially, for grid interfacing where several hundred volts is usually required. Therefore, the PV cells are connected in series to form PV modules which have higher output voltages, typically in the range of 30 to 40 volts. Moreover, the PV modules can be connected in series and in parallel to form larger entities called PV generators.

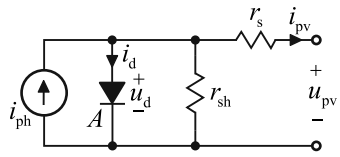

Fig. 1.1: The one-diode model of a PV cell.

The PV cell is commonly modeled using the one-diode model as depicted in Fig. 1.1 (Lo Brano et al., 2010). A forward-biased diode with an ideality factor A is connected in parallel with a current source i_{ph} which corresponds to the photocurrent generated by the irradiance that reaches the surface of the cell. The diode models the recombination of electrons inside the cell, while the resistances r_{s} and r_{sh} model the electrical losses.

The output current of the one-diode model i_{pv} depends on the terminal voltage u_{pv} of the cell and on the nonidealities according to (1.1) where I_0 is the dark saturation current of the diode and U_{th} is the thermal voltage of the diode, respectively.

$$i_{\mathrm{pv}} = i_{\mathrm{ph}} - I_0 \left[\exp\left(\frac{u_{\mathrm{pv}} + r_{\mathrm{s}} i_{\mathrm{pv}}}{A U_{\mathrm{th}}} \right) - 1 \right] - \frac{u_{\mathrm{pv}} + r_{\mathrm{s}} i_{\mathrm{pv}}}{r_{\mathrm{sh}}} \tag{1.1}$$

The operation of a PV generator can be modeled using the one-diode model because it is scalable to higher power and voltage levels. The PV generator produces a DC current i_{pv} which depends non-linearly on the voltage of the generator u_{pv}. The normalized UI-curve of a real PV generator is depicted in Fig. 1.2. The current reaches its maximum when the voltage is zero which is referred as the short-circuit current I_{sc}. The maximum output voltage of the PV generator occurs when the output current reaches zero which is referred as the open-circuit voltage U_{oc}. Maximum power P_{MPP} is generated between these two operating points at the maximum power point (MPP) as discussed, e.g., in (Wyatt and Chua, 1983). The current stays relatively constant at voltages below the MPP. This region is referred as the constant current (CC) region. On the other hand, the voltage stays relatively constant at voltages higher than the MPP and this region is referred as the constant voltage (CV) region.

The output impedance of the PV generator can be approximated by using the dynamic resistance r_{pv}. The dynamic resistance can be derived based on the IU-curve as the incremental resistance of the curve according to (1.2) as discussed, e.g., in (Nousiainen et al., 2013). The dynamic resistance is different for each operating point and depends also on the environmental variables, such as temperature and irradiance, which affect the shape of the IU-curve. The value of the dynamic resistance is the largest in the CC region and the smallest in the CV region. At the MPP, the dynamic resistance equals the static resistance $U_{\mathrm{MPP}}/I_{\mathrm{MPP}}$. The minus sign in (1.2) is required since the current

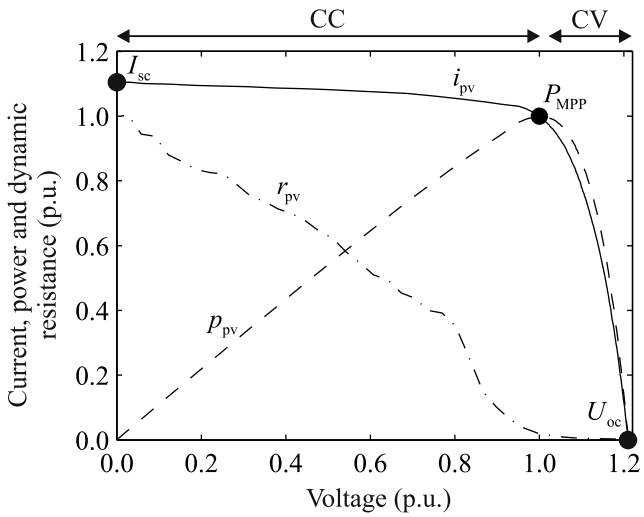

Fig. 1.2: Electrical characteristics of a photovoltaic generator.

flowing out of the generator i_{pv} is defined positive.

$$r_{\mathrm{pv}} = -\frac{\Delta u_{\mathrm{pv}}}{\Delta i_{\mathrm{pv}}} \tag{1.2}$$

A maximum-power-point tracking algorithm (MPPT) is usually used to track the MPP (Femia et al., 2005; Hohm and Ropp, 2000). The operating point of the PV generator is kept at the MPP using a power electronic converter (Villalva et al., 2010). The maximum voltage of the generator depends mainly on the ambient temperature and irradiance has only a slight effect on it. On the other hand, the maximum current of the generator depends directly on the irradiance. In usual operating conditions, the changes in irradiance are much faster than the changes in temperature of the generator (Torres Lobera and Valkealahti, 2013). Therefore, the voltage of the generator is more stable than the current when the environmental variables are considered.

The problem with current control is the fact that a sudden change in the output current of the PV generator due to irradiance change can saturate the controller which causes the operating point to deviate toward the short-circuit operating point I_{sc} (Xiao, W. et al., 2007), away from the MPP. However, the voltage of the PV generator is mainly affected by the ambient temperature and sudden temperature changes are rare in real operating conditions which is the reason why the voltage control is usually preferred.

1.3 Grid-interfacing of photovoltaic generators

Renewable energy sources are interfaced to the utility grid by using power electronic converters. The power electronics allow low conversion losses and the possibility to control critical electrical quantities such as the voltage of the PV generator (Azmi et al., 2013; Blaabjerg, Chen and Kjaer, 2004). Without power electronics, the maximum energy could not be extracted since the PV generator could not be operated at the MPP.

The output current of a PV generator is DC and has to be converted into AC to interface with the utility grid. The conversion is done by using single or three-phase inverters. Single-phase inverters generate ripple in the DC-link voltage at twice the fundamental frequency of the grid voltage due to fluctuating power flow. The voltage ripple has to be attenuated to an appropriate level to avoid additional power losses since the operating voltage of the PV generator would oscillate around the MPP. Large DC-link capacitors can be used to mitigate the ripple (Kjaer et al., 2002) or, alternatively, a power decoupling circuit can be added which removes the ripple from the DC voltage (Krein et al., 2012). However, additional components add the cost of the PV inverter. This is undesirable since power electronic converters contribute increasingly to the total cost of a PV system due to decreasing PV module prices. However, in case of three-phase inverters, the power flow is nearly constant which allows using smaller DC-link capacitors. Moreover, using a three-phase inverter avoids the problem of asymmetry in the phase currents since all three phase currents have the same amplitude in a balanced grid. Therefore, three-phase inverters are often preferred, especially, in high-power applications.

Different three-phase inverter topologies have been developed for PV applications: The neutral-point-clamped (NPC) inverter provides lower harmonics at the switching frequency due to three output voltage levels (Alepuz et al., 1999, 2006; Cavalcanti et al., 2012). However, the control system is more complex since an additional voltage-balancing control has to be used in the DC-link. Other topologies that have caught attention include the current-source inverter (CSI), in which an inductor is used in the DC-link (Chen and Smedley, 2008; Sahan et al., 2008), and the Z-source inverter (Huang et al., 2006). Both of these topologies have an inherent voltage-boost capability which is beneficial in PV applications. However, the CSI has six blocking diodes which add the costs. Moreover, the Z-source inverter requires more passive components and a complex control system. However, in this thesis the focus is on the voltage-source inverter (VSI) since it is the most widely studied topology in the literature (Azmi et al., 2013; Miret et al., 2012).

The conversion from DC to AC can be done directly by using a single-stage inverter as shown in Fig. 1.3 (Jain and Agarwal, 2007) or, alternatively, a two-stage inverter shown in Fig. 1.4 which has an additional DC-DC stage (Carrasco et al., 2006; Ho et al., 2013). Using a voltage-boosting DC-DC converter between the generator and the inverter allows operating the voltage of the PV generator over a wider range, whereas, in

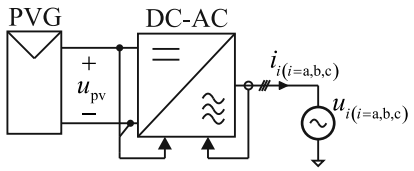

Fig. 1.3: Single-stage photovoltaic inverter.

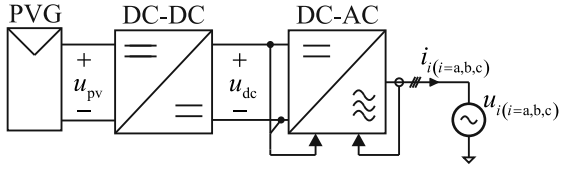

Fig. 1.4: Two-stage photovoltaic inverter.

the single-stage inverter the minimum voltage of the PV generator is constrained by the peak of the grid voltage. Therefore, the two-stage inverter allows using PV generators with lower MPP voltage. Moreover, the wider voltage range allows operating the PV generator with better efficiency when partial shading occurs since the global MPP can be located at lower voltages than in the single-MPP case (Dhople et al., 2010; Ji et al., 2011).

The discussions in this thesis are limited to two-stage inverters based on the VSI topology and a voltage-boosting DC-DC converter. The other topologies are out of the scope of this thesis.

1.4 Issues in photovoltaic inverters

This section shortly reviews the main issues encountered in grid-interfacing of PV generators, such as poor reliability, harmonic currents and instabilities caused by impedance-based interactions.

Reliability

The reliability of grid-connected PV systems is an issue that requires special attention since interruptions in the power generation due to device failure can be costly and the source of malfunction can be hard to identify. Recent studies have shown that the PV module itself is quite reliable and contributes with only a few percent in total failures of a PV power plant (Golnas, 2013). As much as 43 percent of the failures were reported to be related to a malfunctioning of inverter, especially, to its control software. Some commercial inverters have been shown to suffer from interrupted operation and poor

MPP-tracking efficiency as discussed, e.g., in (Petrone et al., 2008).

Robust control design has become one of the most discussed topics related to PV inverters due to the observed problems with the control software. The control of three-phase PV inverters is most often realized by cascading the output current and the DC-link-voltage control loops. It has been shown that a one-stage cascade-controlled VSI-type PV inverter contains a right-half-plane (RHP) pole in its control dynamics when the PV generator operates in the CC region (Puukko, Nousiainen and Suntio, 2011). Similar observations were made in an airborne wind turbine which was connected to the utility grid using a VSI (Kolar et al., 2013). A motor drive operating in the regeneration mode with a VSI-based power stage has also been reported to suffer from instability caused by a RHP-pole (Espinoza et al., 2000).

RHP-poles and zeros can make the control system unstable if they are not taken properly into account in the control design. The small-signal model, on which the control design is usually based, should be verified by using frequency response measurements (Castelló and Espi, 2012). Otherwise, the design might be based on a model that does not give correct predictions on the stability of the control system. The RHP-pole affects also the control dynamics of a two-stage PV inverter and its effect on the sizing of the DC-link capacitance is discussed in detail in Chapter 3.

Harmonic currents

Poor power quality has been reported in areas, where the penetration level of photovoltaic energy is high, i.e., in areas where a large number of PV inverters is connected to the utility grid, as discussed in (Enslin and Heskes, 2004). The harmonic content of the output currents of these inverters was reported to increase and some inverters became unstable when the amount of background distortion was increased up to the maximum allowable limit. The source of the harmonic currents was identified as the parallel and series resonance phenomena between the inverter and the utility grid. A similar resonance issue was demonstrated in (Zhang et al., 2014) related to an inverter which was used to interface a wind-turbine to a long submarine transmission cable. The harmonic currents generated by the switching action can be mitigated using an LCL-filter as discussed, e.g., in (Rockhill et al., 2011). However, the harmonic components that appear at frequencies that are not specific for the used modulation method need special attention.

Impedance-based interactions

The shape of the inverter's output impedance is a determining factor in power quality and stability issues (Hiti, S. et al., 1994; Wen et al., 2012). In fact, the PV inverter should be designed to have high output impedance in order to avoid impedance-based

interactions originating from the AC-side since in real operating conditions the grid is far from ideal voltage source. The output current of a PV inverter has been shown to become unstable when the inverter is connected to a grid which has high inductance (Cespedes and Sun, 2009). Therefore, inverters should be designed so that they can cope with a large variation of grid impedance values (Ledwich and Sharma, 2000; Liserre et al., 2004).

Input impedance of an active rectifier is known to resemble a negative resistor at frequencies below the crossover frequency of the DC-link voltage control (Harnefors et al., 2007; Wen et al., 2013). Recently, similar observations have been made regarding the output impedance of single and three-phase PV inverters (Cespedes and Sun, 2014; Heskes et al., 2010; Visscher and Heskes, 2005). The source of the negative resistance-like behavior has been argued to be the phase-locked-loop (PLL). The PLL is required to synchronize the output currents of the inverter with the grid voltages to operate the inverter with unity power factor (Chung, 2000). The negative resistance has been shown to expose the inverter to impedance-based interactions even with a grid impedance that resembles a passive circuit, such as an inductance. Impedance-based interactions can cause elevated harmonic currents and even make the inverter unstable. An accurate small-signal model which includes the effect of the PLL is needed to predict the behavior of the inverter's output impedance. The model would allow the designers to predict and avoid instabilities and harmonic resonances caused by the impedance-based interactions. A small-signal model of a VSI-based PV inverter with PLL is developed and verified by frequency response measurements in Chapter 4.

Modeling of three-phase inverters

Several modeling techniques have been proposed in the literature, such as the frequency-shift technique (Blaabjerg, Aquila and Liserre, 2004) and the harmonic linearization method (Sun, 2009). In (Rim et al., 1990) the switch matrix of a three-phase converter was replaced with an equivalent transformer. However, three-phase inverters are most often modeled in the synchronous reference frame using space-vectors (Bordonau et al., 1997; Cvetkovic et al., 2011; Harnefors, 2007; Hiti et al., 1994; Yazdani et al., 2011). In addition, the complexity of the small-signal model can be reduced in certain conditions (Mao et al., 1998). However, neglecting critical control loops, such as the PLL or grid-voltage feedforward can hide important information on the dynamic behavior of the inverter. Naturally, such model gives poor predictions, e.g., on the shape of the inverter's output impedance and should not be used in stability analysis. The small-signal models found in the literature are far from complete since a variety of control schemes can be used in the final product. However, this thesis takes one step toward completing the small-signal model by including the effects of the PLL and the grid-voltage feedforward which are described in detail in Chapters 4 and 5.

1.5 Scientific contributions

The main scientific contribution of this thesis can be summarized as follows:

- The effect of the first-stage DC-DC converter on the dynamic behavior of a two-stage PV inverter is clarified.
- The existence of the RHP-pole in the control dynamics of a two-stage PV inverter is shown to be dependent on the control mode of the DC-DC converter. The DC-link capacitance design rule is modified to match the requirement of two-stage inverters.
- The small-signal model of a three-phase PV inverter is upgraded by adding the effect of the PLL. The upgraded model shows that the q-component of the inverter's output impedance behaves as a negative resistor. The negative-resistance behavior can cause instability when the inverter is connected to a weak grid that has large inductance.
- The small-signal model a three-phase PV inverter is further upgraded to include the effect of grid-voltage feedforward. The upgraded model shows that the feed-forward increases the magnitude of both the d and q-components of the inverter's output impedance, thus, making the inverter more resistant to impedance-based interactions.

1.6 List of published papers

[P1] Messo, T., Jokipii, J. and Suntio, T. (2014). "Effect of conventional grid-voltage feedforward on the output impedance of a three-phase PV inverter", in *International Power Electronics Conference, IPEC*, pp. 1–8

[P2] Messo, T., Jokipii, J., Puukko, J. and Suntio, T. (2014). "Determining the value of dc-link capacitance to ensure stable operation of a three-phase photovoltaic inverter", in *IEEE Transactions on Power Electronics*, vol. 29, no. 2, pp. 665–673

[P3] Messo, T., Jokipii, J. and Suntio, T. (2013). "Minimum dc-link capacitance requirement of a two-stage photovoltaic inverter", in *IEEE Energy Conversion Congress & Exposition, ECCE´13*, pp. 999–1006.

[P4] Messo, T., Jokipii, J., Mäkinen, A. and Suntio, T. (2013). "Modeling the grid synchronization induced negative-resistor-like behavior in the output impedance of a three-phase photovoltaic inverter", in *4th IEEE International Symposium on Power Electronics for Distributed Generation Systems, PEDG´13*, pp. 1–8.

[P5] Messo, T., Jokipii, J. and Suntio, T. (2012). "Steady-state and dynamic properties of boost-power-stage converter in photovoltaic applications", in *3rd IEEE International Symposium on Power Electronics for Distributed Generation Systems, PEDG´12*, pp. 1–7

[P6] Messo, T., Puukko, J. and Suntio, T. (2012). "Effect of MPP-tracking dc/dc converter on VSI-based photovoltaic inverter dynamics", in *IET Power Electronics, Machines and Drives Conference, PEMD´12*, pp. 1–6

[P7] Puukko, J., Messo, T. and Suntio, T. (2011). "Effect of photovoltaic generator on a typical VSI-based three-phase grid-connected photovoltaic inverter dynamics", in *IET Conference on Renewable Power Generation, RPG´11*, pp. 1–6

[P8] Puukko, J., Messo, T., Nousiainen, L., Huusari, J. and Suntio, T. (2011). "Negative output impedance in three-phase grid-connected renewable energy source inverters based on reduced-order model", in *IET Conference on Renewable Power Generation, RPG´11*, pp. 1–6

[P9] Nousiainen, L., Puukko, J., Mäki, A., Messo, T., Huusari, J., Jokipii, J., Viinamäki, J., Torres Lobera, D., Valkealahti, S. and Suntio, T. (2013). "Photovoltaic generator as an input source for power electronic converters", *IEEE Transactions on Power Electronics*, vol. 28, no. 6, pp. 3028–3038

The author has the main responsibility on performing the experiments and writing the publications in [P1]–[P6]. Dr.Tech. Anssi Mäki provided the simulation model of a PV generator which was used in [P2]–[P8]. M.Sc. Jokipii contributed to the measurements in [P1]–[P5] and gave valuable insight to overcome numerous encountered challenges related to the experimental setup and helped to develop the small-signal model. M.Sc. Mäkinen helped with the tuning of the LCL-filter and the simulation model in [P4]. Dr.Tech. Puukko provided the results related to the DC-link capacitance sizing of a single-stage inverter in [P2] and helped with the writing process and analysis in [P6]. Dr.Tech. Nousiainen built the three-phase prototype inverter which was used in [P2]–[P4]. Prof. Suntio oversaw the writing process of all publications, gave priceless hints regarding the experiments and theory and helped to refine the publications in terms of terminology and language. The author helped with the dynamic modeling in [P7] and the experimental measurements in [P8] where Dr.Tech. Puukko was the main author. The author helped with the measurements in [P9] where Dr.Tech. Nousiainen was the main author.

1.7 Structure of the thesis

The rest of the thesis is organized as follows; Chapter 2 familiarizes the reader with the small-signal models of the DC-DC converter, three-phase inverter and its output filter

which are used throughout the thesis. In addition, the method to analyze the stability of interconnected DC and AC systems is reviewed. Chapter 3 discusses the effect of the voltage-boosting DC-DC converter on the dynamics related to the DC-link voltage control. The PLL is included in the small-signal model of the inverter in Chapter 4. The effect of grid-voltage feedforward on the small-signal model is discussed in Chapter 5. Final conclusions are drawn and future topics are proposed in Chapter 6.

2 BACKGROUND OF THE THESIS

The purpose of this chapter is to familiarize the reader to dynamic modeling of power electronic converters. The state-space averaging method is reviewed which is often used to model the dynamic behavior of power electronic converters. Moreover, it is shown how the same principles can be used to model also three-phase inverters and three-phase filters by utilizing space vectors. The small-signal models of a voltage-boosting DC-DC converter, three-phase VSI-based inverter, and a three-phase CL-filter are derived. The method to include the effect of nonideal sources on the dynamics of power electronic converters is also reviewed. Finally, simple tools to analyze small-signal stability of interconnected power electronic systems are given.

2.1 Modeling of switched-mode DC-DC converters

Middlebrook introduced the modeling method of switched-mode converters in the 70's (Middlebrook and Slobodan, 1976) which is based on the state-space averaging. The basic idea behind the method is to average the behavior of the currents and voltages of the converter over a switching period and linearize the equations by using the first-order derivatives of the Taylor series. The method has been utilized ever since because it gives accurate estimates on the small-signal behavior of DC-DC converters in the frequency-range up to half the switching frequency.

The converter can be divided into different subcircuits according to the possible states of the power electronic switches. The state-space model is averaged over one switching period, i.e., all the switching states are taken into account. The average model is linearized at a specific operating point yielding the linearized state space as given in a general form in (2.1). The vectors $\hat{\mathbf{u}}$ and $\hat{\mathbf{y}}$ contain the input and output variables and the vector $\hat{\mathbf{x}}$ contains the state variables. $\mathbf{A}$, $\mathbf{B}$, $\mathbf{C}$ and $\mathbf{D}$ are coefficient matrices which include only constants.

$$\begin{aligned} \frac{\mathrm{d}\hat{\mathbf{x}}}{\mathrm{d}t} &= \mathbf{A}\hat{\mathbf{x}} + \mathbf{B}\hat{\mathbf{u}} \\ \hat{\mathbf{y}} &= \mathbf{C}\hat{\mathbf{x}} + \mathbf{D}\hat{\mathbf{u}} \end{aligned} \tag{2.1}$$

The linearized state-space can be transformed into the frequency domain where the

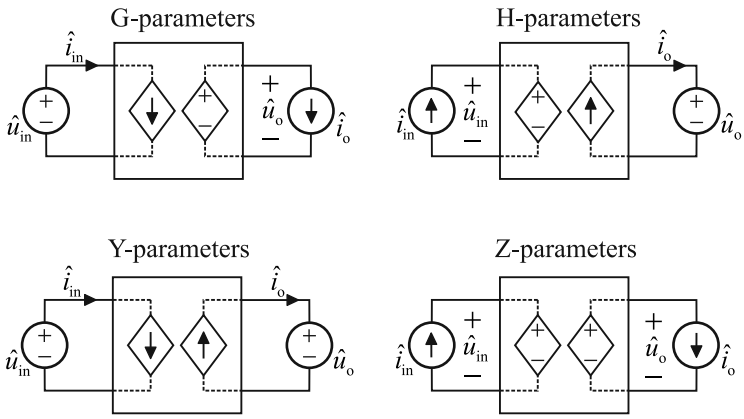

Fig. 2.1: Classification of the network parameters.

mapping between the input $\mathbf{U}(s)$ and output variables $\mathbf{Y}(s)$ can be solved as given in (2.2) where s is the Laplace-variable. The transfer functions representing the dynamics of the converter are given by the matrix $\mathbf{G}$.

$$\mathbf{Y}(s) = \left[\mathbf{C}(s\mathbf{I} - \mathbf{A})^{-1}\mathbf{B} + \mathbf{D}\right]\mathbf{U}(s) = \mathbf{G}\mathbf{U}(s) \tag{2.2}$$

The inductor currents and capacitor voltages are usually selected as the state-variables. Therefore, there are as many state variables as there are inductors and capacitors. The input and output variables are selected according to the application. There are four different ways to select the input and output variables (Tse, 1998). The corresponding four parameter sets are named as G, H, Y and Z-parameters as depicted in Fig. 2.1. The G-parameters are to be used in applications where the source is a voltage source such as a storage battery and the load is an electronic load which draws a constant current. The H-parameters are to be used in PV applications since the source is a current source (the PV generator) and the load is usually a storage battery or an inverter which regulates its DC-side voltage. The Y-parameters are to be used to model a converter which is fed and loaded by a storage battery. And, finally, the Z-parameters are to be used, e.g., to model a stand-alone PV converter which feeds an electronic load.

2.2 Small-signal model of the voltage-boosting DC-DC converter

The power stage of the DC-DC converter studied in this thesis is based on the conventional voltage-fed boost converter where a capacitor C_1 is added at the input of the converter to enable the interfacing of the PV generator. The power stage of the converter

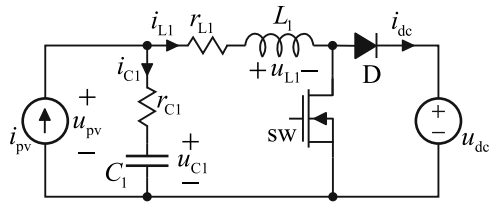

Fig. 2.2: Power stage of the DC-DC converter.

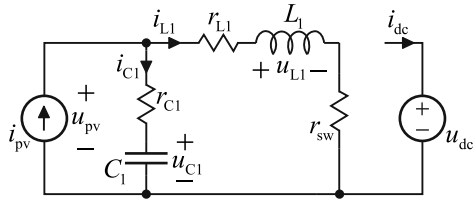

Fig. 2.3: Subcircuit of the DC-DC converter when the switch is conducting.

is depicted in Fig. 2.2. The generator is modeled as a current source to justify the use of input-voltage control of the DC-DC converter and the load is modeled as a voltage source since the inverter controls the DC-link voltage u_{dc}. The current through the inductor L_1 and the voltage of the capacitor C_1 are selected as state variables. The voltage of the PV generator u_{pv} and the output current i_{dc} are selected as output variables. The circuit operates in the continuous-conduction-mode (CCM) which means that the inductor current or the capacitor voltage does not drop to zero during the normal operation.

The power electronic switch 'sw' is switched at high frequency. Fig. 2.3 shows the power stage when the switch is conducting. At the same time the diode is reverse-biased and blocks the current. The switch is modeled using a parasitic resistance r_{sw} to model the conduction and switching losses associated to the switch. The state-space representation of the on-time subcircuit is given in (2.3)–(2.6).

$$\frac{\mathrm{d}i_{\mathrm{L1\text{-}on}}}{\mathrm{d}t} = \frac{1}{L_1}\left[u_{\mathrm{C1}} + r_{\mathrm{C1}} i_{\mathrm{pv}} - \left(r_{\mathrm{C1}} + r_{\mathrm{L1}} + r_{\mathrm{sw}}\right) i_{\mathrm{L1}}\right] \tag{2.3}$$

$$\frac{\mathrm{d}u_{\mathrm{C1\text{-}on}}}{\mathrm{d}t} = \frac{1}{C_1}\left[i_{\mathrm{pv}} - i_{\mathrm{L1}}\right] \tag{2.4}$$

$$u_{\mathrm{pv\text{-}on}} = u_{\mathrm{C1}} + r_{\mathrm{C1}} i_{\mathrm{pv}} - r_{\mathrm{C1}} i_{\mathrm{L1}} \tag{2.5}$$

$$i_{\mathrm{dc\text{-}on}} = 0 \tag{2.6}$$

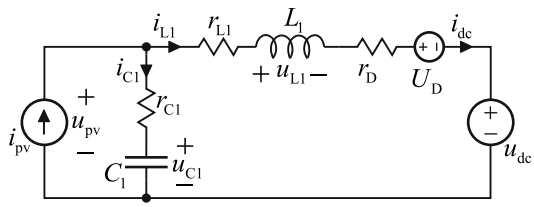

Fig. 2.4: Subcircuit of the DC-DC converter when the diode is conducting.

The off-time subcircuit of the converter is shown in Fig. 2.4. A series connected resistor r_D and a voltage source representing the diode threshold voltage U_D is considered as an adequate model for the diode. The state-space representation of the off-time subcircuit is given in (2.7)–(2.10).

$$\frac{\mathrm{d}i_{\mathrm{L1\text{-}off}}}{\mathrm{d}t} = \frac{1}{L_1}\left[u_{\mathrm{C1}} + r_{\mathrm{C1}} i_{\mathrm{pv}} - (r_{\mathrm{C1}} + r_{\mathrm{L1}} + r_\mathrm{D})\, i_{\mathrm{L1}} - u_{\mathrm{dc}} - U_\mathrm{D}\right] \tag{2.7}$$

$$\frac{\mathrm{d}u_{\mathrm{C1\text{-}off}}}{\mathrm{d}t} = \frac{1}{C_1}\left[i_{\mathrm{pv}} - i_{\mathrm{L1}}\right] \tag{2.8}$$

$$u_{\mathrm{pv\text{-}off}} = u_{\mathrm{C1}} + r_{\mathrm{C1}} i_{\mathrm{pv}} - r_{\mathrm{C1}} i_{\mathrm{L1}} \tag{2.9}$$

$$i_{\mathrm{dc\text{-}off}} = i_{\mathrm{L1}} \tag{2.10}$$

The average model of the converter can be obtained by making the small-ripple approximation which means that the current i_{L1} through the inductor and the capacitor voltage u_{C1} are considered as constants over the switching period. The averaged currents and voltages are denoted using angle brackets. The on-time equations in (2.3) – (2.6) are multiplied by the duty ratio of the switch d and off-time equations in (2.7) – (2.10) are multiplied by the complementary duty ratio $d' = (1 - d)$, i.e., the duty ratio of the diode. The two state spaces are finally added together which yields the average model as shown in (2.11)–(2.14). The equivalent resistance R_1 is defined in (2.15) to simplify the notation.

$$\frac{\mathrm{d}\langle i_{\mathrm{L1}}\rangle}{\mathrm{d}t} = \frac{1}{L_1}\left[\langle u_{\mathrm{C1}}\rangle + r_{\mathrm{C1}}\langle i_{\mathrm{pv}}\rangle - R_1\langle i_{\mathrm{L1}}\rangle - d'\langle u_{\mathrm{dc}}\rangle - U_\mathrm{D} d'\right] \tag{2.11}$$

$$\frac{\mathrm{d}\langle u_{\mathrm{C1}}\rangle}{\mathrm{d}t} = \frac{1}{C_1}\left[\langle i_{\mathrm{pv}}\rangle - \langle i_{\mathrm{L1}}\rangle\right] \tag{2.12}$$

$$\langle u_{\mathrm{pv}}\rangle = -r_{\mathrm{C1}}\langle i_{\mathrm{L1}}\rangle + \langle u_{\mathrm{C1}}\rangle + r_{\mathrm{C1}}\langle i_{\mathrm{pv}}\rangle \tag{2.13}$$

$$\langle i_{\mathrm{dc}} \rangle = d' \langle i_{\mathrm{L1}} \rangle, \tag{2.14}$$

$$R_1 = r_{\mathrm{C1}} + r_{\mathrm{L1}} + d r_{\mathrm{sw}} + d' r_{\mathrm{D}} \tag{2.15}$$

The steady-state operating point can be solved from the average model by setting the derivative terms on the left hand side equal to zero and denoting all the variables by their uppercase steady-state values. The operating point is as given in (2.16).

$$\begin{aligned} D' &= \frac{U_{\mathrm{pv}} - (r_{\mathrm{sw}} + r_{\mathrm{L1}})\, I_{\mathrm{pv}}}{U_{\mathrm{dc}} + U_{\mathrm{D}} - (r_{\mathrm{sw}} - r_{\mathrm{D}})\, I_{\mathrm{pv}}} \\ U_{\mathrm{C1}} &= U_{\mathrm{pv}} \\ I_{\mathrm{dc}} &= D' I_{\mathrm{pv}} \\ I_{\mathrm{L1}} &= I_{\mathrm{pv}} \end{aligned} \tag{2.16}$$

The average model is linearized by developing the partial derivatives at the predefined operating point yielding the coefficient matrices $\mathbf{A}$, $\mathbf{B}$, $\mathbf{C}$ and $\mathbf{D}$ as in (2.17) and (2.18).

$$\begin{bmatrix} \frac{\mathrm{d}\hat{i}_{\mathrm{L1}}}{\mathrm{d}t} \\ \frac{\mathrm{d}\hat{u}_{\mathrm{C1}}}{\mathrm{d}t} \end{bmatrix} = \overbrace{\begin{bmatrix} -\frac{R_1}{L_1} & \frac{1}{L_1} \\ -\frac{1}{C_1} & 0 \end{bmatrix}}^{\mathbf{A}} \begin{bmatrix} \hat{i}_{\mathrm{L1}} \\ \hat{u}_{\mathrm{C1}} \end{bmatrix} + \overbrace{\begin{bmatrix} \frac{r_{\mathrm{C1}}}{L_1} & -\frac{D'}{L_1} & \frac{U_{\mathrm{dc}} + U_{\mathrm{D}}}{L_1} \\ \frac{1}{C_1} & 0 & 0 \end{bmatrix}}^{\mathbf{B}} \begin{bmatrix} \hat{i}_{\mathrm{pv}} \\ \hat{u}_{\mathrm{dc}} \\ \hat{d} \end{bmatrix} \tag{2.17}$$

$$\begin{bmatrix} \hat{u}_{\mathrm{pv}} \\ \hat{i}_{\mathrm{dc}} \end{bmatrix} = \overbrace{\begin{bmatrix} -r_{\mathrm{C1}} & 1 \\ D' & 0 \end{bmatrix}}^{\mathbf{C}} \begin{bmatrix} \hat{i}_{\mathrm{L1}} \\ \hat{u}_{\mathrm{C1}} \end{bmatrix} + \overbrace{\begin{bmatrix} r_{\mathrm{C1}} & 0 & 0 \\ 0 & 0 & -I_{\mathrm{pv}} \end{bmatrix}}^{\mathbf{D}} \begin{bmatrix} \hat{i}_{\mathrm{pv}} \\ \hat{u}_{\mathrm{dc}} \\ \hat{d} \end{bmatrix} \tag{2.18}$$

The mapping between the input and output variables can be solved by transforming (2.17) and (2.18) into the frequency-domain and by applying (2.2). The transfer functions can be collected from the matrix $\mathbf{G}$ and are named according to their physical meaning, e.g., the transfer function between the input current and input voltage is named as the input impedance $Z_{\text{in-o}}$ as shown in (2.19). The transfer functions are given explicitly in Appendix A.

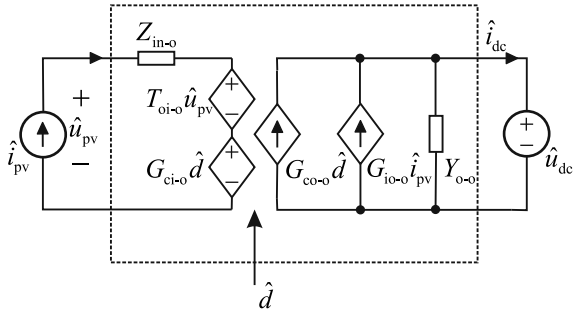

Fig. 2.5: Linear model of the DC-DC converter.

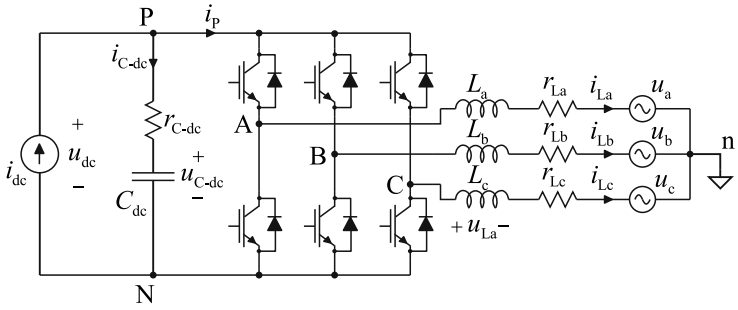

Fig. 2.6: Power stage of a three-phase PV inverter.

$$\begin{bmatrix} \hat{u}_{\mathrm{pv}} \\ \hat{i}_{\mathrm{dc}} \end{bmatrix} = \overbrace{\begin{bmatrix} Z_{\mathrm{in\text{-}o}} & T_{\mathrm{oi\text{-}o}} & G_{\mathrm{ci\text{-}o}} \\ G_{\mathrm{io\text{-}o}} & -Y_{\mathrm{o\text{-}o}} & G_{\mathrm{co\text{-}o}} \end{bmatrix}}^{\mathbf{G}} \begin{bmatrix} \hat{i}_{\mathrm{pv}} \\ \hat{u}_{\mathrm{dc}} \\ \hat{d} \end{bmatrix} \tag{2.19}$$

The transfer functions in (2.19) can be used to construct a linear two-port model of the converter which is depicted in Fig. 2.5. The linear model can be used to include nonidealities, such as a source impedance, in the dynamics of the converter or to study the interactions between other converters or input/output filters.

2.3 Small-signal model of the three-phase VSI-based PV inverter

Power stage of a two-level three-phase PV inverter is depicted in Fig. 2.6. The power stage is fed from a current source to justify the use of DC-link-voltage control and is loaded by balanced three-phase voltage sources that represent an ideal three-phase grid.

2.3.1 Average model of the PV inverter

The small-signal modeling of three-phase two-level inverters has been extensively studied in the literature. The most common method is to transform the three-phase variables into the synchronous reference frame which rotates at the angular frequency of the three-phase grid where the three-phase currents and voltages become DC-valued. Due to this feature, the steady-state operating point can be solved and the average model can be linearized using the state-space averaging method.

A three-phase system can be represented using a rotating space vector which has three components named as alpha, beta and zero component. The space vector can be given as a complex vector and the zero component as shown in (2.20) and (2.21). The scaling factor K determines the type of the transformation, i.e., amplitude or power-invariant transformation. The transformation is amplitude-invariant when the scaling factor is selected as $2/3$ and power-invariant when it is selected as $\sqrt{2/3}$. The amplitude-invariant transformation or Clarke's transformation is used in this thesis (Duesterhoeft et al., 1951).

$$\boldsymbol{x} = x_\alpha + \mathrm{j}x_\beta = K\left(x_\mathrm{a} + x_\mathrm{b}\mathrm{e}^{\mathrm{j}2\pi/3} + x_\mathrm{c}\mathrm{e}^{\mathrm{j}4\pi/3}\right) \tag{2.20}$$

$$x_0 = \frac{(x_\mathrm{a} + x_\mathrm{b} + x_\mathrm{c})}{3} \tag{2.21}$$

The Clarke's transformation can be given in a matrix form as in (2.22).

$$\begin{bmatrix} x_\alpha \\ x_\beta \\ x_0 \end{bmatrix} = \frac{2}{3}\begin{bmatrix} 1 & -1/2 & -1/2 \\ 0 & \sqrt{3}/2 & -\sqrt{3}/2 \\ 1/2 & 1/2 & 1/2 \end{bmatrix}\begin{bmatrix} x_\mathrm{a} \\ x_\mathrm{b} \\ x_\mathrm{c} \end{bmatrix} \tag{2.22}$$

The space vectors can be transformed back into three-phase variables by using the inverse of the Clarke's transformation matrix given in (2.23).

$$\begin{bmatrix} x_\mathrm{a} \\ x_\mathrm{b} \\ x_\mathrm{c} \end{bmatrix} = \begin{bmatrix} 1 & 0 & 1 \\ -1/2 & \sqrt{3}/2 & 1 \\ -1/2 & -\sqrt{3}/2 & 1 \end{bmatrix}\begin{bmatrix} x_\alpha \\ x_\beta \\ x_0 \end{bmatrix} \tag{2.23}$$

The averaged voltages over the inductors can be solved from Fig. 2.6 by using Kirchhoff's voltage law and are as given in (2.24)–(2.26) where d_A, d_B and d_C are the duty ratios of the upper switches in each phase-leg, u_nN is the common-mode voltage as given

in (2.27) and R_2 is the sum of parasitic resistances of a single switch and a single AC-side inductor. All switches and inductors are assumed to be identical.

$$\langle u_{\mathrm{La}} \rangle = d_{\mathrm{A}} \langle u_{\mathrm{dc}} \rangle - R_2 \langle i_{\mathrm{La}} \rangle - \langle u_{\mathrm{a}} \rangle - \langle u_{\mathrm{nN}} \rangle \tag{2.24}$$

$$\langle u_{\mathrm{Lb}} \rangle = d_{\mathrm{B}} \langle u_{\mathrm{dc}} \rangle - R_2 \langle i_{\mathrm{Lb}} \rangle - \langle u_{\mathrm{b}} \rangle - \langle u_{\mathrm{nN}} \rangle \tag{2.25}$$

$$\langle u_{\mathrm{Lc}} \rangle = d_{\mathrm{C}} \langle u_{\mathrm{dc}} \rangle - R_2 \langle i_{\mathrm{Lc}} \rangle - \langle u_{\mathrm{c}} \rangle - \langle u_{\mathrm{nN}} \rangle \tag{2.26}$$

$$\langle u_{\mathrm{nN}} \rangle = \frac{1}{3} \left(\langle u_{\mathrm{AN}} \rangle + \langle u_{\mathrm{BN}} \rangle + \langle u_{\mathrm{CN}} \rangle \right) \tag{2.27}$$

The averaged inductor voltages can be represented using the space vectors as in (2.28) where boldface font is used to denote that the variables are transformed into a space-vector.

$$\langle \boldsymbol{u_{\mathrm{L}}} \rangle = \boldsymbol{d} \langle u_{\mathrm{dc}} \rangle - R_2 \langle \boldsymbol{i_{\mathrm{L}}} \rangle - \langle \boldsymbol{u_{\mathrm{g}}} \rangle \tag{2.28}$$

The common-mode voltage disappears in the transformation since the space vector of the common-mode voltage is zero according to (2.29).

$$\frac{2}{3} \left(\langle u_{\mathrm{nN}} \rangle e^{\mathrm{j}0} + \langle u_{\mathrm{nN}} \rangle e^{\mathrm{j}\frac{2\pi}{3}} + \langle u_{\mathrm{nN}} \rangle e^{\mathrm{j}\frac{4\pi}{3}} \right) = 0 \tag{2.29}$$

The space-vectors of inductor voltages, duty ratios, inductor currents and grid voltages are as given in (2.30) – (2.33)

$$\langle \boldsymbol{u_{\mathrm{L}}} \rangle = \frac{2}{3} \left(\langle u_{\mathrm{La}} \rangle e^{\mathrm{j}0} + \langle u_{\mathrm{Lb}} \rangle e^{\mathrm{j}\frac{2\pi}{3}} + \langle u_{\mathrm{Lc}} \rangle e^{\mathrm{j}\frac{4\pi}{3}} \right) \tag{2.30}$$

$$\boldsymbol{d} = \frac{2}{3} \left(d_{\mathrm{A}} e^{\mathrm{j}0} + d_{\mathrm{B}} e^{\mathrm{j}\frac{2\pi}{3}} + d_{\mathrm{C}} e^{\mathrm{j}\frac{4\pi}{3}} \right) \tag{2.31}$$

$$\langle \boldsymbol{i_{\mathrm{L}}} \rangle = \frac{2}{3} \left(\langle i_{\mathrm{La}} \rangle e^{\mathrm{j}0} + \langle i_{\mathrm{Lb}} \rangle e^{\mathrm{j}\frac{2\pi}{3}} + \langle i_{\mathrm{Lc}} \rangle e^{\mathrm{j}\frac{4\pi}{3}} \right) \tag{2.32}$$

$$\langle \boldsymbol{u_{\mathrm{g}}} \rangle = \frac{2}{3} \left(\langle u_{\mathrm{a}} \rangle e^{\mathrm{j}0} + \langle u_{\mathrm{b}} \rangle e^{\mathrm{j}\frac{2\pi}{3}} + \langle u_{\mathrm{c}} \rangle e^{\mathrm{j}\frac{4\pi}{3}} \right) \tag{2.33}$$

A space vector can be represented in the synchronous reference frame using a direct (d), quadrature (q) and zero components as discussed in (Park, 1929). The space vector can be transformed into the synchronous reference frame using the Park's transformation

given in (2.34) where the superscript 's' is used to denote that the space vector is given in the synchronous reference frame and ω_s is the angular frequency of the three-phase system.

$$\boldsymbol{x}^\mathrm{s} = \boldsymbol{x}\mathrm{e}^{-\mathrm{j}\omega_\mathrm{s}t} = x_\mathrm{d} + \mathrm{j}x_\mathrm{q} \tag{2.34}$$

The derivative of the inductor current can be given in the synchronous reference frame as in (2.35) which is obtained by transforming (2.28) into the synchronous reference frame by using (2.34).

$$\frac{\mathrm{d}\langle \boldsymbol{i}_\mathbf{L}^\mathbf{s} \rangle}{\mathrm{d}t} = \frac{1}{L}\boldsymbol{d}^\mathbf{s}\langle u_\mathrm{dc}\rangle - \left(\frac{R_2}{L} + \mathrm{j}\omega_\mathrm{s}\right)\langle \boldsymbol{i}_\mathbf{L}^\mathbf{s}\rangle - \frac{1}{L}\langle \boldsymbol{u}_\mathbf{g}^\mathbf{s}\rangle \tag{2.35}$$

The average current flowing toward the switches of the inverter $\langle i_\mathrm{P}\rangle$ can be solved as a function of the duty ratios and phase currents yielding (2.36).

$$\langle i_\mathrm{P}\rangle = d_\mathrm{A}\langle i_\mathrm{La}\rangle + d_\mathrm{B}\langle i_\mathrm{Lb}\rangle + d_\mathrm{C}\langle i_\mathrm{Lc}\rangle \tag{2.36}$$

The average current can be given in the stationary reference frame by noting the inverse of the Clarke's transformation (2.23) and is as given in (2.37).

$$\langle i_\mathrm{P}\rangle = \frac{3}{2}\left(d_\alpha\langle i_{\mathrm{L}\alpha}\rangle + d_\beta\langle i_{\mathrm{L}\beta}\rangle\right) \tag{2.37}$$

Moreover, the current can be expressed as the real part of the product of the duty ratio and the complex conjugate of the inductor current and expressed in the synchronous reference frame as in (2.38).

$$\langle i_\mathrm{P}\rangle = \frac{3}{2}\mathrm{Re}\left[\boldsymbol{d}\cdot\boldsymbol{i}_\mathbf{L}^*\right] = \frac{3}{2}\mathrm{Re}\left[\boldsymbol{d}^\mathbf{s}\cdot\boldsymbol{i}_\mathbf{L}^{\mathbf{s}*}\right] = \frac{3}{2}\left(d_\mathrm{d}\langle i_\mathrm{Ld}\rangle + d_\mathrm{q}\langle i_\mathrm{Lq}\rangle\right) \tag{2.38}$$

The average capacitor current can be given in the synchronous reference frame as in (2.39).

$$\langle i_\mathrm{C\text{-}dc}\rangle = -\frac{3}{2}\left(d_\mathrm{d}\langle i_\mathrm{Ld}\rangle + d_\mathrm{q}\langle i_\mathrm{Lq}\rangle\right) + \langle i_\mathrm{dc}\rangle \tag{2.39}$$

The average DC-link voltage $\langle u_\mathrm{dc}\rangle$ can be presented by using the currents and duty

ratios in the synchronous reference frame as in (2.40).

$$\langle u_{\mathrm{dc}} \rangle = -\frac{3}{2} r_{\text{C-dc}} d_{\mathrm{d}} \langle i_{\mathrm{Ld}} \rangle - \frac{3}{2} r_{\text{C-dc}} d_{\mathrm{q}} \langle i_{\mathrm{Lq}} \rangle + r_{\text{C-dc}} \langle i_{\mathrm{dc}} \rangle + \langle u_{\text{C-dc}} \rangle \tag{2.40}$$

The average DC-link voltage has to be substituted back in (2.35) to complete the average model of the inverter because the DC-link voltage is an output variable. The averaged state-space model of the inverter in the synchronous reference frame is as given in (2.41) – (2.46)

$$\begin{aligned} \frac{\mathrm{d}\langle i_{\mathrm{Ld}} \rangle}{\mathrm{d}t} = &-\left(\frac{R_2}{L} + \frac{3 r_{\text{C-dc}}}{2L} d_{\mathrm{d}}^2 \right) \langle i_{\mathrm{Ld}} \rangle + \left(\omega_{\mathrm{s}} - \frac{3 r_{\text{C-dc}}}{2L} d_{\mathrm{d}} d_{\mathrm{q}} \right) \langle i_{\mathrm{Lq}} \rangle \\ &+ \frac{r_{\text{C-dc}}}{L} d_{\mathrm{d}} \langle i_{\mathrm{dc}} \rangle + \frac{1}{L} d_{\mathrm{d}} \langle u_{\text{C-dc}} \rangle - \frac{1}{L} \langle u_{\mathrm{od}} \rangle \end{aligned} \tag{2.41}$$

$$\begin{aligned} \frac{\mathrm{d}\langle i_{\mathrm{Lq}} \rangle}{\mathrm{d}t} = &-\left(\omega_{\mathrm{s}} - \frac{3 r_{\text{C-dc}}}{2L} d_{\mathrm{d}} d_{\mathrm{q}} \right) \langle i_{\mathrm{Ld}} \rangle - \left(\frac{R_2}{L} + \frac{3 r_{\text{C-dc}}}{2L} d_{\mathrm{q}}^2 \right) \langle i_{\mathrm{Lq}} \rangle \\ &+ \frac{r_{\text{C-dc}}}{L} d_{\mathrm{q}} \langle i_{\mathrm{dc}} \rangle + \frac{1}{L} d_{\mathrm{q}} \langle u_{\text{C-dc}} \rangle - \frac{1}{L} \langle u_{\mathrm{oq}} \rangle \end{aligned} \tag{2.42}$$

$$\frac{\mathrm{d}\langle u_{\text{C-dc}} \rangle}{\mathrm{d}t} = -\frac{3}{2 C_{\mathrm{dc}}} d_{\mathrm{d}} \langle i_{\mathrm{Ld}} \rangle - \frac{3}{2 C_{\mathrm{dc}}} d_{\mathrm{q}} \langle i_{\mathrm{Lq}} \rangle + \frac{1}{C_{\mathrm{dc}}} \langle i_{\mathrm{dc}} \rangle \tag{2.43}$$

$$\langle u_{\mathrm{dc}} \rangle = -\frac{3}{2} r_{\text{C-dc}} d_{\mathrm{d}} \langle i_{\mathrm{Ld}} \rangle - \frac{3}{2} r_{\text{C-dc}} d_{\mathrm{q}} \langle i_{\mathrm{Lq}} \rangle + r_{\text{C-dc}} \langle i_{\mathrm{dc}} \rangle + \langle u_{\text{C-dc}} \rangle \tag{2.44}$$

$$\langle i_{\text{o-d}} \rangle = \langle i_{\mathrm{Ld}} \rangle \tag{2.45}$$

$$\langle i_{\text{o-q}} \rangle = \langle i_{\mathrm{Lq}} \rangle \tag{2.46}$$

2.3.2 Linearized model of the PV inverter

The sinusoidal currents and voltages at the fundamental frequency of the grid are DC-valued in the synchronous reference frame which allows solving the steady-state operating point. The steady-state values of q-components of the output current I_{Lq} and the output voltage U_{oq} are assumed to be zero since the inverter is operated with unity power factor and the reference frame of the control system is aligned with the d-component of the grid

voltage by the PLL. The steady-state operating point is as given in (2.47) – (2.51).

$$D_{\mathrm{d}} = \frac{U_{\mathrm{od}} + \sqrt{(-U_{\mathrm{od}})^2 + \frac{8}{3} R_2 U_{\mathrm{dc}} I_{\mathrm{dc}}}}{2U_{\mathrm{dc}}} \tag{2.47}$$

$$D_{\mathrm{q}} = \frac{2\omega_{\mathrm{s}} L I_{\mathrm{dc}}}{3D_{\mathrm{d}} U_{\mathrm{dc}}} \tag{2.48}$$

$$I_{\mathrm{Ld}} = \frac{2I_{\mathrm{dc}}}{3D_{\mathrm{d}}} \tag{2.49}$$

$$I_{\mathrm{Lq}} = 0 \tag{2.50}$$

$$U_{\text{C-dc}} = \frac{U_{\mathrm{od}}}{D_{\mathrm{d}}} + \frac{2R_2 I_{\mathrm{dc}}}{3D_{\mathrm{d}}^2} = U_{\mathrm{dc}} \tag{2.51}$$

The linearized state-space model of the PV inverter in the synchronous reference frame is as given in (2.52) and (2.53).

$$\begin{bmatrix} \frac{\mathrm{d}\hat{i}_{\mathrm{Ld}}}{\mathrm{d}t} \\ \frac{\mathrm{d}\hat{i}_{\mathrm{Lq}}}{\mathrm{d}t} \\ \frac{\mathrm{d}\hat{u}_{\text{C-dc}}}{\mathrm{d}t} \end{bmatrix} = \overbrace{\begin{bmatrix} -\left(\frac{R_2}{L} + \frac{3r_{\text{C-dc}}}{2L} D_{\mathrm{d}}^2\right) & \left(\omega_{\mathrm{s}} - \frac{\omega_{\mathrm{s}} r_{\text{C-dc}} I_{\mathrm{dc}}}{U_{\mathrm{dc}}}\right) & \frac{D_{\mathrm{d}}}{L} \\ -\left(\omega_{\mathrm{s}} + \frac{\omega_{\mathrm{s}} r_{\text{C-dc}} I_{\mathrm{dc}}}{U_{\mathrm{dc}}}\right) & -\left(\frac{R_2}{L} + \frac{3r_{\text{C-dc}}}{2L} D_{\mathrm{q}}^2\right) & \frac{D_{\mathrm{q}}}{L} \\ -\frac{3D_{\mathrm{d}}}{2C_{\mathrm{dc}}} & -\frac{3D_{\mathrm{q}}}{2C_{\mathrm{dc}}} & 0 \end{bmatrix}}^{\mathbf{A}} \begin{bmatrix} \hat{i}_{\mathrm{Ld}} \\ \hat{i}_{\mathrm{Lq}} \\ \hat{u}_{\text{C-dc}} \end{bmatrix}$$

$$+ \overbrace{\begin{bmatrix} \frac{r_{\text{C-dc}} D_{\mathrm{d}}}{L} & -\frac{1}{L} & 0 & \frac{U_{\mathrm{dc}} - r_{\text{C-dc}} I_{\mathrm{dc}}}{L} & 0 \\ \frac{r_{\text{C-dc}} D_{\mathrm{q}}}{L} & 0 & -\frac{1}{L} & -\frac{r_{\text{C-dc}} D_{\mathrm{q}} I_{\mathrm{dc}}}{D_{\mathrm{d}} L} & \frac{U_{\mathrm{dc}}}{L} \\ \frac{1}{C_{\text{C-dc}}} & 0 & 0 & -\frac{I_{\mathrm{dc}}}{D_{\mathrm{d}} C_{\mathrm{dc}}} & 0 \end{bmatrix}}^{\mathbf{B}} \begin{bmatrix} \hat{i}_{\mathrm{dc}} \\ \hat{u}_{\mathrm{od}} \\ \hat{u}_{\mathrm{oq}} \\ \hat{d}_{\mathrm{d}} \\ \hat{d}_{\mathrm{q}} \end{bmatrix} \tag{2.52}$$

$$\begin{bmatrix} \hat{u}_{\mathrm{dc}} \\ \hat{i}_{\mathrm{od}} \\ \hat{i}_{\mathrm{oq}} \end{bmatrix} = \overbrace{\begin{bmatrix} -\frac{3D_{\mathrm{d}}r_{\text{C-dc}}}{2} & -\frac{3D_{\mathrm{q}}r_{\text{C-dc}}}{2} & 1 \\ 1 & 0 & 0 \\ 0 & 1 & 0 \end{bmatrix}}^{\mathbf{C}} \begin{bmatrix} \hat{i}_{\mathrm{Ld}} \\ \hat{i}_{\mathrm{Lq}} \\ \hat{u}_{\text{C-dc}} \end{bmatrix} + \overbrace{\begin{bmatrix} r_{\text{C-dc}} & 0 & 0 & \frac{r_{\text{C-dc}}I_{\mathrm{dc}}}{D_{\mathrm{d}}} & 0 \\ 0 & 0 & 0 & 0 & 0 \\ 0 & 0 & 0 & 0 & 0 \end{bmatrix}}^{\mathbf{D}} \begin{bmatrix} \hat{i}_{\mathrm{dc}} \\ \hat{u}_{\mathrm{od}} \\ \hat{u}_{\mathrm{oq}} \\ \hat{d}_{\mathrm{d}} \\ \hat{d}_{\mathrm{q}} \end{bmatrix} \tag{2.53}$$

Transfer functions can be solved using (2.2) yielding the matrix $\mathbf{G}$ as given in (2.54). The corresponding transfer functions are given in Appendix B without parasitic resistances.

$$\begin{bmatrix} \hat{u}_{\mathrm{dc}} \\ \hat{i}_{\mathrm{od}} \\ \hat{i}_{\mathrm{oq}} \end{bmatrix} = \overbrace{\begin{bmatrix} Z_{\mathrm{in}} & T_{\text{oi-d}} & T_{\text{oi-q}} & G_{\text{ci-d}} & G_{\text{ci-q}} \\ G_{\text{io-d}} & -Y_{\text{o-d}} & -Y_{\text{o-qd}} & G_{\text{co-d}} & G_{\text{co-qd}} \\ G_{\text{io-q}} & -Y_{\text{o-dq}} & -Y_{\text{o-q}} & G_{\text{co-dq}} & G_{\text{co-q}} \end{bmatrix}}^{\mathbf{G}} \begin{bmatrix} \hat{i}_{\mathrm{dc}} \\ \hat{u}_{\mathrm{od}} \\ \hat{u}_{\mathrm{oq}} \\ \hat{d}_{\mathrm{d}} \\ \hat{d}_{\mathrm{q}} \end{bmatrix} \tag{2.54}$$

The input and output dynamics of the inverter can be separated from the transfer function matrix of (2.54) as given in (2.55) and (2.56), respectively.

$$\hat{u}_{\mathrm{dc}} = Z_{\mathrm{in}}\hat{i}_{\mathrm{dc}} + \overbrace{\begin{bmatrix} T_{\text{oi-d}} & T_{\text{oi-q}} \end{bmatrix}}^{\mathbf{T}_{\mathrm{oi}}} \overbrace{\begin{bmatrix} \hat{u}_{\mathrm{od}} \\ \hat{u}_{\mathrm{oq}} \end{bmatrix}}^{\hat{\mathbf{u}}_{\mathrm{o}}} + \overbrace{\begin{bmatrix} G_{\text{ci-d}} & G_{\text{ci-q}} \end{bmatrix}}^{\mathbf{G}_{\mathrm{ci}}} \overbrace{\begin{bmatrix} \hat{d}_{\mathrm{d}} \\ \hat{d}_{\mathrm{q}} \end{bmatrix}}^{\hat{\mathbf{d}}} \tag{2.55}$$

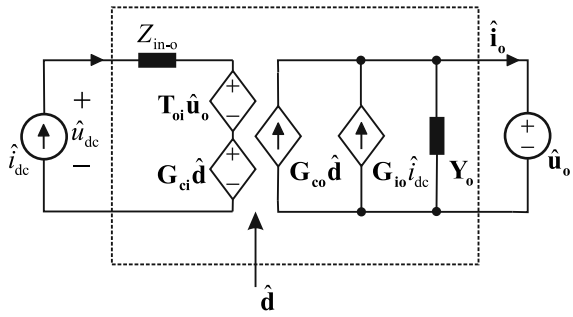

Fig. 2.7: The equivalent small-signal model of a three-phase PV inverter.

$$\overbrace{\begin{bmatrix}\hat{i}_{\text{od}}\\ \hat{i}_{\text{oq}}\end{bmatrix}}^{\hat{\mathbf{i}}_{\text{o}}} = \overbrace{\begin{bmatrix}G_{\text{io-d}}\\ G_{\text{io-q}}\end{bmatrix}}^{\mathbf{G}_{\text{io}}}\hat{i}_{\text{dc}} - \overbrace{\begin{bmatrix}Y_{\text{o-d}} & Y_{\text{o-qd}}\\ Y_{\text{o-dq}} & Y_{\text{o-q}}\end{bmatrix}}^{\mathbf{Y}_{\text{o}}}\overbrace{\begin{bmatrix}\hat{u}_{\text{od}}\\ \hat{u}_{\text{oq}}\end{bmatrix}}^{\hat{\mathbf{u}}_{\text{o}}} + \overbrace{\begin{bmatrix}G_{\text{co-d}} & G_{\text{co-qd}}\\ G_{\text{co-dq}} & G_{\text{co-q}}\end{bmatrix}}^{\mathbf{G}_{\text{co}}}\overbrace{\begin{bmatrix}\hat{d}_{\text{d}}\\ \hat{d}_{\text{q}}\end{bmatrix}}^{\hat{\mathbf{d}}} \tag{2.56}$$

Transfer functions in (2.55) and (2.56) can be used to construct an equivalent small-signal model of the inverter as shown in Fig. 2.7 which resembles the linear model of the DC-DC converter presented in Fig. 2.5. The output currents, voltages, duty ratios and all the transfer functions, excluding input impedance, are matrix valued and are marked using boldface font.

2.3.3 Closed-loop transfer functions of the PV inverter

The inverter is controlled using the cascaded control scheme as shown in Fig. 2.8. The DC-link-voltage controller G_{cv} gives a reference $u_{\text{i-d}}^{\text{ref}}$ for the current controller G_{cd} which regulates d-component of the output current i_{od}^{c}. The q-component of the output current is regulated at zero by the second current controller G_{cq}. The phase angle of the grid θ_{c} is sensed using the phase-locked-loop (PLL).

The closed-loop transfer functions can be solved by first considering only the output-current control. Control block diagrams describing the input dynamics and the output dynamics related to d and q-components are depicted in Figs. 2.9 and 2.10 when the output-current control loops are closed. The control block diagrams can be derived from

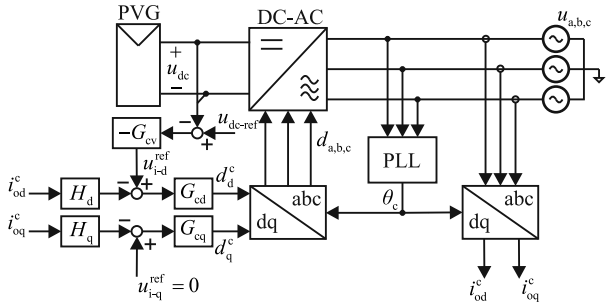

Fig. 2.8: Cascaded control scheme.

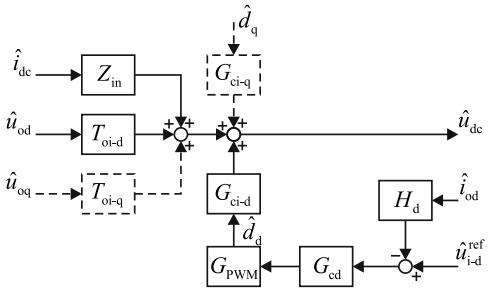

Fig. 2.9: Input dynamics with output current control.

(2.55) and (2.56) by including the transfer functions related to the current control in the diagram. G_{PWM} is the gain originating from the pulse-width modulator (PWM) and H_{d} and H_{q} are the current sensing gains. Input dynamics can be approximated by neglecting the transfer functions originating from the q-components because only real power is transferred (Mao et al., 1998). Moreover, the cross-coupling transfer functions between the d and q-components are assumed to be negligible. Therefore, the signal paths marked with dashed lines are neglected in the analysis.

The closed-loop transfer functions are as given in (2.57) – (2.65) when only the output current control is considered. $L_{\text{out-d}}$ and $L_{\text{out-q}}$ are the loop gains of the current control of the d and q-components which can be solved using (2.66) and (2.67). $Z_{\mathrm{in-d-}\infty}$ and $T_{\mathrm{oi-d-}\infty}$ are special parameters which can be solved from the open-loop transfer functions using (2.68) and (2.69). The superscript 'cc' is used to denote that the output-current control loops are closed.

$$G^{\mathrm{cc}}_{\text{io-d}} = \frac{\hat{i}_{\mathrm{od}}}{\hat{i}_{\mathrm{dc}}} = \frac{G_{\text{io-d}}}{1 + L_{\text{out-d}}} \tag{2.57}$$

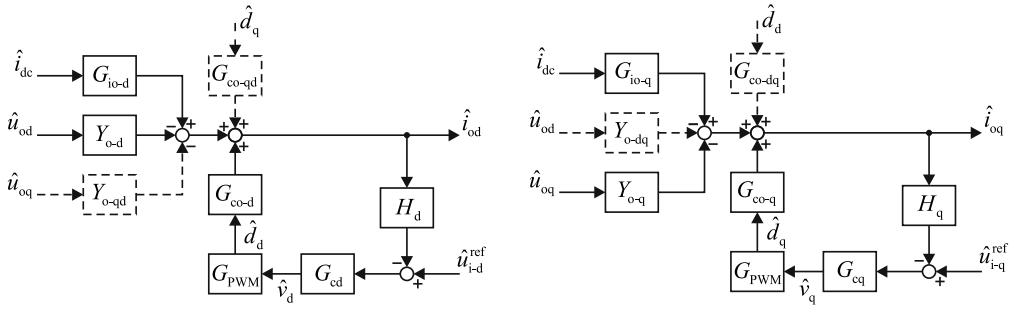

(a) Dynamics of the d-component.

(b) Dynamics of the q-component.

Fig. 2.10: Output dynamics of the inverter when output-current control loops are closed.

$$Y^{cc}_{o\text{-}d} = -\frac{\hat{i}_{od}}{\hat{u}_{od}} = \frac{Y_{o\text{-}d}}{1 + L_{out\text{-}d}} \tag{2.58}$$

$$G^{cc}_{co\text{-}d} = \frac{\hat{i}_{od}}{\hat{u}^{ref}_{i\text{-}d}} = \frac{1}{H_d}\frac{L_{out\text{-}d}}{1 + L_{out\text{-}d}} \tag{2.59}$$

$$G^{cc}_{io\text{-}q} = \frac{\hat{i}_{oq}}{\hat{i}_{dc}} = \frac{G_{io\text{-}q}}{1 + L_{out\text{-}q}} \tag{2.60}$$

$$Y^{cc}_{o\text{-}q} = -\frac{\hat{i}_{oq}}{\hat{u}_{oq}} = \frac{Y_{o\text{-}q}}{1 + L_{out\text{-}q}} \tag{2.61}$$

$$G^{cc}_{co\text{-}q} = \frac{\hat{i}_{oq}}{\hat{u}^{ref}_{i\text{-}q}} = \frac{1}{H_q}\frac{L_{out\text{-}q}}{1 + L_{out\text{-}q}} \tag{2.62}$$

$$Z^{cc}_{in} = \frac{\hat{u}_{dc}}{i_{dc}} = \frac{Z_{in}}{1 + L_{out\text{-}d}} + \frac{L_{out\text{-}d}}{1 + L_{out\text{-}d}} Z_{in-\infty} \tag{2.63}$$

$$T^{cc}_{oi\text{-}d} = \frac{\hat{u}_{dc}}{u_{od}} = \frac{T_{oi\text{-}d}}{1 + L_{out\text{-}d}} + \frac{L_{out\text{-}d}}{1 + L_{out\text{-}d}} T_{oi-d-\infty} \tag{2.64}$$

$$G^{cc}_{ci\text{-}d} = \frac{1}{H_d}\frac{G_{ci\text{-}d}}{G_{co\text{-}d}}\frac{L_{out\text{-}d}}{1 + L_{out\text{-}d}} \tag{2.65}$$

$$L_{out\text{-}d} = G_{co\text{-}d} G_{PWM} G_{cd} H_d \tag{2.66}$$

$$L_{out\text{-}q} = G_{co\text{-}q} G_{PWM} G_{cq} H_q \tag{2.67}$$

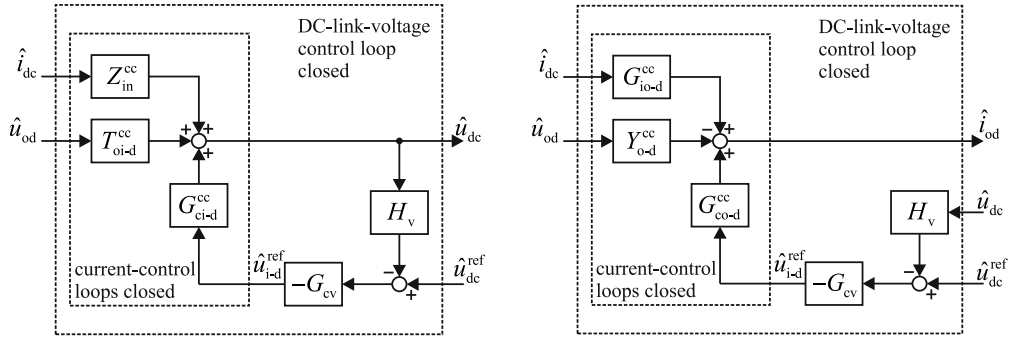

(a) Input dynamics. **(b)** Output dynamics related to the d-components.

Fig. 2.11: Control block diagrams with DC-link voltage control.

$$Z_{\text{in}-\text{d}-\infty} = Z_{\text{in}} - \frac{G_{\text{ci-d}} G_{\text{io-d}}}{G_{\text{co-d}}} \tag{2.68}$$

$$T_{\text{oi}-\text{d}-\infty} = T_{\text{oi-d}} + \frac{G_{\text{ci-d}} Y_{\text{o-d}}}{G_{\text{co-d}}} \tag{2.69}$$

The transfer functions that describe the output dynamics of q-components are not affected by the DC-link voltage control and are as given in (2.60) – (2.62). However, the reference of the d-component of the output current is given by the DC-link voltage controller and, thus, the DC-link voltage control has to be included in the output dynamics related to d-components. Moreover, the input dynamics of the inverter can be approximated by considering only the current control of the d-component (Mao et al., 1998; Puukko, J. et al., 2011). Transfer functions with the DC-link voltage control can be solved by using the previously solved transfer functions in (2.57) – (2.65) and by considering the output-current-controlled inverter as an open-loop system where the new control variable is the reference of the current controller $\hat{u}_{\text{i-d}}^{\text{ref}}$. Control block diagrams that describe the input dynamics and the output dynamics related to the d-component are shown in Fig. 2.11 where the signal paths related to the q-components are neclegted.

The transfer functions with DC-link voltage control can be solved from the block diagrams in Fig. 2.11 yielding (2.70) – (2.75) where L_{dc} is the DC-link-voltage control loop gain as given in (2.76) and $G_{\text{io}-\text{d}-\infty}$ and $Y_{\text{o}-\text{d}-\infty}$ are special parameters as defined in (2.77) and (2.78), respectively.

$$Z_{\text{in-c}} = \frac{\hat{u}_{\text{dc}}}{\hat{i}_{\text{dc}}} = \frac{Z_{\text{in}}}{(1+L_{\text{dc}})(1+L_{\text{out-d}})} + \frac{1}{(1+L_{\text{dc}})} \frac{L_{\text{out-d}}}{(1+L_{\text{out-d}})} Z_{\text{in}-\infty} \tag{2.70}$$

$$T_{\text{oi-d-c}} = \frac{\hat{u}_{\text{dc}}}{\hat{u}_{\text{od}}} = \frac{T_{\text{oi-d}}}{(1+L_{\text{dc}})(1+L_{\text{out-d}})} + \frac{1}{(1+L_{\text{dc}})}\frac{L_{\text{out-d}}}{(1+L_{\text{out-d}})}T_{\text{oi}-\text{d}-\infty} \tag{2.71}$$

$$G_{\text{ri}} = \frac{\hat{u}_{\text{dc}}}{\hat{u}_{\text{dc}}^{\text{ref}}} = \frac{1}{H_{\text{v}}}\frac{L_{\text{dc}}}{1+L_{\text{dc}}} \tag{2.72}$$

$$G_{\text{io-d-c}} = \frac{\hat{i}_{\text{od}}}{\hat{i}_{\text{dc}}} = \frac{G_{\text{io-d}}}{(1+L_{\text{dc}})(1+L_{\text{out-d}})} + \frac{L_{\text{dc}}}{(1+L_{\text{dc}})}G_{\text{io}-\text{d}-\infty} \tag{2.73}$$

$$Y_{\text{o-d-c}} = \frac{\hat{i}_{\text{od}}}{\hat{u}_{\text{od}}} = \frac{Y_{\text{o-d}}}{(1+L_{\text{dc}})(1+L_{\text{out-d}})} + \frac{L_{\text{dc}}}{(1+L_{\text{dc}})}Y_{\text{o}-\text{d}-\infty} \tag{2.74}$$

$$G_{\text{ro}} = \frac{\hat{i}_{\text{od}}}{\hat{u}_{\text{dc}}^{\text{ref}}} = \frac{1}{H_{\text{v}}}\frac{L_{\text{dc}}}{(1+L_{\text{dc}})}\frac{G_{\text{co-d-o}}}{G_{\text{ci-d-o}}} \tag{2.75}$$

$$L_{\text{dc}} = -G_{\text{ci-d}}^{\text{cc}}G_{\text{cv}}H_{\text{v}} = -\frac{H_{\text{v}}}{H_{\text{d}}}\frac{L_{\text{out-d}}}{(1+L_{\text{out-d}})}\frac{G_{\text{ci-d}}}{G_{\text{co-d}}}G_{\text{cv}} \tag{2.76}$$

$$G_{\text{io}-\text{d}-\infty} = G_{\text{io-d}} - \frac{G_{\text{co-d}}Z_{\text{in}}}{G_{\text{ci-d}}} \tag{2.77}$$

$$Y_{\text{o}-\text{d}-\infty} = Y_{\text{o-d}} + \frac{G_{\text{co-d}}T_{\text{oi-d}}}{G_{\text{ci-d}}} \tag{2.78}$$

2.4 Small-signal model of a three-phase CL-filter

A three-phase CL-type filter is usually used to attenuate the frequency components in the output current of a PV inverter which are generated by the high-frequency switching. The circuit diagram of the filter is depicted in Fig. 2.12. The filter is fed from three AC-current sources since the PV inverter operates under output current control and the filter is loaded by the three-phase grid voltages. Therefore, the output variables of the filter are the three-phase voltages $u_{\text{in-f-a}}$,$u_{\text{in-f-b}}$ and $u_{\text{in-f-c}}$ and the three-phase currents $i_{\text{o-f-a}}$, $i_{\text{o-f-b}}$ and $i_{\text{o-f-c}}$, respectively.

The voltages over the filter inductors can be solved using the Kirchoff's voltage law yielding (2.79) when all phases are assumed to be symmetrical.

$$\begin{aligned} u_{\text{Lf}-\text{a}} &= u_{\text{in}-\text{f}-\text{a}} - r_{\text{Lf}}i_{\text{Lf}-\text{a}} - u_{\text{o}-\text{a}} \\ u_{\text{Lf}-\text{b}} &= u_{\text{in}-\text{f}-\text{b}} - r_{\text{Lf}}i_{\text{Lf}-\text{b}} - u_{\text{o}-\text{b}} \\ u_{\text{Lf}-\text{c}} &= u_{\text{in}-\text{f}-\text{c}} - r_{\text{Lf}}i_{\text{Lf}-\text{c}} - u_{\text{o}-\text{c}} \end{aligned} \tag{2.79}$$

The capacitor currents can be solved using Kirchoff's current law yielding (2.80).

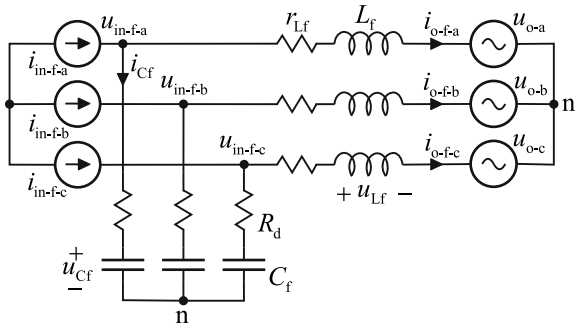

Fig. 2.12: Three-phase CL-filter.

$$\begin{aligned} i_{\text{Cf-a}} &= i_{\text{in-f-a}} - i_{\text{Lf-a}} \\ i_{\text{Cf-b}} &= i_{\text{in-f-b}} - i_{\text{Lf-b}} \\ i_{\text{Cf-c}} &= i_{\text{in-f-c}} - i_{\text{Lf-c}} \end{aligned} \tag{2.80}$$

The input voltages of the filter can be given as a function of the capacitor currents and voltages as shown in (2.81).

$$\begin{aligned} u_{\text{in-f-a}} &= R_{\text{d}} i_{\text{Cf-a}} + u_{\text{Cf-a}} = R_{\text{d}} i_{\text{in-f-a}} - R_{\text{d}} i_{\text{Lf-a}} + u_{\text{Cf-a}} \\ u_{\text{in-f-b}} &= R_{\text{d}} i_{\text{Cf-b}} + u_{\text{Cf-b}} = R_{\text{d}} i_{\text{in-f-b}} - R_{\text{d}} i_{\text{Lf-b}} + u_{\text{Cf-b}} \\ u_{\text{in-f-c}} &= R_{\text{d}} i_{\text{Cf-c}} + u_{\text{Cf-c}} = R_{\text{d}} i_{\text{in-f-c}} - R_{\text{d}} i_{\text{Lf-c}} + u_{\text{Cf-c}} \end{aligned} \tag{2.81}$$

The input voltages can be substituted back in (2.79) allowing the derivatives of the inductor currents to be represented as in (2.82).

$$\begin{aligned} \frac{\mathrm{d}i_{\text{Lf-a}}}{\mathrm{d}t} &= -\frac{R_{\text{d}} + r_{\text{Lf}}}{L_{\text{f}}} i_{\text{Lf-a}} + \frac{u_{\text{Cf-a}}}{L_{\text{f}}} + \frac{R_{\text{d}}}{L_{\text{f}}} i_{\text{in-f-a}} + \frac{u_{\text{o-a}}}{L_{\text{f}}} \\ \frac{\mathrm{d}i_{\text{Lf-b}}}{\mathrm{d}t} &= -\frac{R_{\text{d}} + r_{\text{Lf}}}{L_{\text{f}}} i_{\text{Lf-b}} + \frac{u_{\text{Cf-b}}}{L_{\text{f}}} + \frac{R_{\text{d}}}{L_{\text{f}}} i_{\text{in-f-b}} + \frac{u_{\text{o-b}}}{L_{\text{f}}} \\ \frac{\mathrm{d}i_{\text{Lf-c}}}{\mathrm{d}t} &= -\frac{R_{\text{d}} + r_{\text{Lf}}}{L_{\text{f}}} i_{\text{Lf-c}} + \frac{u_{\text{Cf-c}}}{L_{\text{f}}} + \frac{R_{\text{d}}}{L_{\text{f}}} i_{\text{in-f-c}} + \frac{u_{\text{o-c}}}{L_{\text{f}}} \end{aligned} \tag{2.82}$$

The derivatives of capacitor voltages can be given as in (2.83).

$$\begin{aligned}
\frac{\mathrm{d}i_{\text{Cf-a}}}{\mathrm{d}t} &= \frac{i_{\text{in-a}}}{C_\text{f}} - \frac{i_{\text{L-a}}}{C_\text{f}} \\
\frac{\mathrm{d}i_{\text{Cf-b}}}{\mathrm{d}t} &= \frac{i_{\text{in-b}}}{C_\text{f}} - \frac{i_{\text{L-b}}}{C_\text{f}} \\
\frac{\mathrm{d}i_{\text{Cf-c}}}{\mathrm{d}t} &= \frac{i_{\text{in-c}}}{C_\text{f}} - \frac{i_{\text{L-c}}}{C_\text{f}}
\end{aligned} \tag{2.83}$$

Finally, after transforming the equations into the synchronous reference frame, the linearized state-space of the CL-filter can be given as in (2.84) and in (2.85). All variables can be replaced with the small-signal variables since the circuit is linear. The parasitic resistance of the capacitor is assumed to be a part of the value of the damping resistor R_d.

$$\begin{bmatrix} \frac{\mathrm{d}\hat{i}_{\text{Lf-d}}}{\mathrm{d}t} \\ \frac{\mathrm{d}\hat{i}_{\text{Lf-q}}}{\mathrm{d}t} \\ \frac{\mathrm{d}\hat{u}_{\text{Cf-d}}}{\mathrm{d}t} \\ \frac{\mathrm{d}\hat{u}_{\text{Cf-q}}}{\mathrm{d}t} \end{bmatrix} = \overbrace{\begin{bmatrix} -\frac{(R_\text{d}+r_{\text{Lf}})}{L_\text{f}} & \omega_\text{s} & \frac{1}{L_\text{s}} & 0 \\ -\omega_\text{s} & -\frac{(R_\text{d}+r_{\text{Lf}})}{L_\text{f}} & 0 & \frac{1}{L_\text{s}} \\ -\frac{1}{C_\text{f}} & 0 & 0 & \omega_\text{s} \\ 0 & -\frac{1}{C_\text{f}} & -\omega_\text{s} & 0 \end{bmatrix}}^{\mathbf{A}} \begin{bmatrix} \hat{i}_{\text{L-d}} \\ \hat{i}_{\text{L-q}} \\ \hat{u}_{\text{Cf-d}} \\ \hat{u}_{\text{Cf-q}} \end{bmatrix} \tag{2.84}$$

$$+ \overbrace{\begin{bmatrix} \frac{R_\text{d}}{L_\text{f}} & 0 & -\frac{1}{L_\text{f}} & 0 \\ 0 & \frac{R_\text{d}}{L_\text{f}} & 0 & -\frac{1}{L_\text{f}} \\ \frac{1}{C_\text{f}} & 0 & 0 & 0 \\ 0 & \frac{1}{C_\text{f}} & 0 & 0 \end{bmatrix}}^{\mathbf{B}} \begin{bmatrix} \hat{i}_{\text{in-f-d}} \\ \hat{i}_{\text{in-f-q}} \\ \hat{u}_{\text{o-d}} \\ \hat{u}_{\text{o-q}} \end{bmatrix}$$

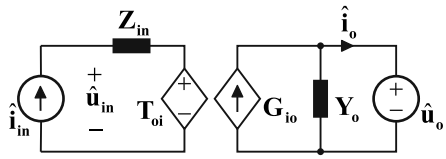

Fig. 2.13: The equivalent small-signal model of a three-phase CL-filter.

$$\begin{bmatrix} \hat{u}_{\text{in-f-d}} \\ \hat{u}_{\text{in-f-q}} \\ \hat{i}_{\text{o-f-d}} \\ \hat{i}_{\text{o-f-q}} \end{bmatrix} = \overbrace{\begin{bmatrix} -R_{\text{d}} & 0 & 1 & 0 \\ 0 & -R_{\text{d}} & 0 & 1 \\ 1 & 0 & 0 & 0 \\ 0 & 1 & 0 & 0 \end{bmatrix}}^{\mathbf{C}} \begin{bmatrix} \hat{i}_{\text{Lf-d}} \\ \hat{i}_{\text{Lf-q}} \\ \hat{u}_{\text{Cf-d}} \\ \hat{u}_{\text{Cf-q}} \end{bmatrix} + \overbrace{\begin{bmatrix} R_{\text{d}} & 0 & 0 & 0 \\ 0 & R_{\text{d}} & 0 & 0 \\ 0 & 0 & 0 & 0 \\ 0 & 0 & 0 & 0 \end{bmatrix}}^{\mathbf{D}} \begin{bmatrix} \hat{i}_{\text{in-f-d}} \\ \hat{i}_{\text{in-f-q}} \\ \hat{u}_{\text{o-d}} \\ \hat{u}_{\text{o-q}} \end{bmatrix} \tag{2.85}$$

The transfer functions between the input and output variables can be solved by using (2.2) and can be collected from the matrix **G**. The corresponding transfer functions are given in Appendix C without parasitic resistances. The input and output dynamics of the CL-filter can be given in a matrix form according to (2.86) and (2.87).

$$\overbrace{\begin{bmatrix} \hat{u}_{\text{in-d}} \\ \hat{u}_{\text{in-q}} \end{bmatrix}}^{\hat{\mathbf{u}}_{\text{in}}} = \overbrace{\begin{bmatrix} Z_{\text{in-d}} & Z_{\text{in-qd}} \\ Z_{\text{in-dq}} & Z_{\text{in-q}} \end{bmatrix}}^{\mathbf{Z}_{\text{in}}} \overbrace{\begin{bmatrix} \hat{i}_{\text{in-d}} \\ \hat{i}_{\text{in-q}} \end{bmatrix}}^{\hat{\mathbf{i}}_{\text{in}}} + \overbrace{\begin{bmatrix} T_{\text{oi-d}} & T_{\text{oi-qd}} \\ T_{\text{oi-dq}} & T_{\text{oi-q}} \end{bmatrix}}^{\mathbf{T}_{\text{oi}}} \overbrace{\begin{bmatrix} \hat{u}_{\text{o-d}} \\ \hat{u}_{\text{o-q}} \end{bmatrix}}^{\hat{\mathbf{u}}_{\text{o}}} \tag{2.86}$$

$$\overbrace{\begin{bmatrix} \hat{i}_{\text{o-d}} \\ \hat{i}_{\text{o-q}} \end{bmatrix}}^{\hat{\mathbf{i}}_{\text{o}}} = \overbrace{\begin{bmatrix} G_{\text{io-d}} & G_{\text{io-qd}} \\ G_{\text{io-dq}} & G_{\text{io-q}} \end{bmatrix}}^{\mathbf{G}_{\text{io}}} \overbrace{\begin{bmatrix} \hat{i}_{\text{in-d}} \\ \hat{i}_{\text{in-q}} \end{bmatrix}}^{\hat{\mathbf{i}}_{\text{in}}} - \overbrace{\begin{bmatrix} Y_{\text{o-d}} & Y_{\text{o-qd}} \\ Y_{\text{o-dq}} & Y_{\text{o-q}} \end{bmatrix}}^{\mathbf{Y}_{\text{o}}} \overbrace{\begin{bmatrix} \hat{u}_{\text{o-d}} \\ \hat{u}_{\text{o-q}} \end{bmatrix}}^{\hat{\mathbf{u}}_{\text{o}}} \tag{2.87}$$

The equivalent small-signal model of the filter can be constructed based on (2.86) and (2.87) and is as shown in Fig. 2.13.

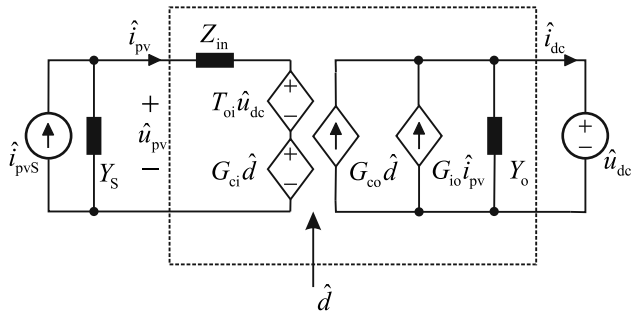

Fig. 2.14: Linear model of the DC-DC converter with non-ideal source.

2.5 Source affected transfer functions

Real sources have a finite output impedance which affects the dynamics of the converter connected to it. This section shortly reviews the method to include the effect of a nonideal source into the dynamics of DC-DC converters and three-phase inverters. The effect of a PV generator on a three-phase inverter has been previously reported in (Puukko, Messo and Suntio, 2011).

2.5.1 Transfer functions of the DC-DC converter

The linear model of the DC-DC converter with a non-ideal source is shown in Fig. 2.14. The impedance of the source is given as an admittance $Y_S = 1/Z_S$ to simplify the notation. Source-affected transfer functions can be obtained by solving the small-signal input current of the power stage $\hat{i}_{pv}$ as in (2.88) and by substituting it back in the dynamics given in (2.19).

$$\hat{i}_{pv} = \hat{i}_{pvS} - Y_S \hat{u}_{pv} \tag{2.88}$$

Source-affected transfer functions of the DC-DC converter can be solved using the open-loop transfer functions in (2.19) and the source admittance Y_S as shown in (2.89) – (2.94). $Z^S_{in\text{-}o}$ is the source-affected input impedance, $T^S_{oi\text{-}o}$ is the transfer function from the output voltage to input voltage, $G^S_{io\text{-}o}$ is the transfer function from input current to output current, $Y^S_{o\text{-}o}$ is output admittance and $G^S_{ci\text{-}o}$ and $G^S_{co\text{-}o}$ are control-related transfer functions. The special parameters are defined as in (2.95) and (2.96).

$$Z^S_{in\text{-}o} = \frac{\hat{u}_{pv}}{\hat{i}_{pvS}} = \frac{Z_{in\text{-}o}}{1 + Y_S Z_{in\text{-}o}} \tag{2.89}$$

$$T_{\text{oi-o}}^{\text{S}} = \frac{\hat{u}_{\text{pv}}}{\hat{u}_{\text{dc}}} = \frac{T_{\text{oi-o}}}{1 + Y_{\text{S}} Z_{\text{in-o}}} \tag{2.90}$$

$$G_{\text{ci-o}}^{\text{S}} = \frac{\hat{u}_{\text{pv}}}{\hat{d}} = \frac{G_{\text{ci-o}}}{1 + Y_{\text{S}} Z_{\text{in-o}}} \tag{2.91}$$

$$G_{\text{io-o}}^{\text{S}} = \frac{\hat{i}_{\text{dc}}}{\hat{i}_{\text{pvS}}} = \frac{G_{\text{io-o}}}{1 + Y_{\text{S}} Z_{\text{in-o}}} \tag{2.92}$$

$$Y_{\text{o-o}}^{\text{S}} = -\frac{\hat{i}_{\text{dc}}}{\hat{u}_{\text{dc}}} = -\frac{1 + Y_{\text{S}} Z_{\text{in-oco}}}{1 + Y_{\text{S}} Z_{\text{in-o}}} Y_{\text{o-o}} \tag{2.93}$$

$$G_{\text{co-o}}^{\text{S}} = \frac{\hat{i}_{\text{dc}}}{\hat{d}} = \frac{1 + Y_{\text{S}} Z_{\text{in}-\infty}}{1 + Y_{\text{S}} Z_{\text{in-o}}} G_{\text{co-o}} \tag{2.94}$$

$$Z_{\text{in-oco}} = Z_{\text{in-o}} + \frac{G_{\text{io-o}} T_{\text{oi-o}}}{Y_{\text{o-o}}} \tag{2.95}$$

$$Z_{\text{in}-\infty} = Z_{\text{in-o}} - \frac{G_{\text{io-o}} G_{\text{ci-o}}}{G_{\text{co-o}}} \tag{2.96}$$

2.5.2 Transfer functions of the PV inverter

The equivalent small-signal model of a three-phase inverter with a non-ideal source is shown in Fig. 2.15. The model resembles the linear model of the DC-DC converter, although some of the transfer functions and variables are matrix-valued. The input current of the power stage $\hat{i}_{\text{pv}}$ is as given in (2.97). The input current can be substituted in the open-loop dynamics given by (2.55) and (2.56) to obtain the source-affected input and output dynamics as given in (2.98) and (2.99).

$$\hat{i}_{\text{dc}} = \hat{i}_{\text{dcS}} - Y_{\text{S}} \hat{u}_{\text{dc}} \tag{2.97}$$

$$\hat{u}_{\text{dc}} = \frac{Z_{\text{in}}}{1 + Z_{\text{in}} Y_{\text{S}}} \hat{i}_{\text{inS}} + \frac{\mathbf{T}_{\text{oi}}}{1 + Z_{\text{in}} Y_{\text{S}}} \hat{\mathbf{u}}_{\text{o}} + \frac{\mathbf{G}_{\text{ci}}}{1 + Z_{\text{in}} Y_{\text{S}}} \hat{\mathbf{d}} \tag{2.98}$$

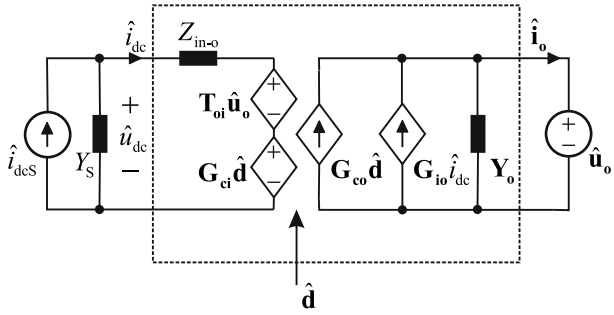

Fig. 2.15: The equivalent small-signal model of the inverter with a nonideal source.

$$\hat{\mathbf{i}}_{\mathrm{o}} = \left[\mathbf{G}_{\mathrm{io}} - \frac{Y_{\mathrm{S}}}{1 + Z_{\mathrm{in}} Y_{\mathrm{S}}}\mathbf{G}_{\mathrm{io}}\right] \hat{i}_{\mathrm{dcS}} - \left[\frac{Y_{\mathrm{S}}}{1 + Z_{\mathrm{in}} Y_{\mathrm{S}}}\mathbf{G}_{\mathrm{io}}\mathbf{T}_{\mathrm{oi}} + \mathbf{Y}_{\mathrm{o}}\right] \hat{\mathbf{u}}_{\mathrm{o}} + \left[\mathbf{G}_{\mathrm{co}} - \frac{Y_{\mathrm{S}}}{1 + Z_{\mathrm{in}} Y_{\mathrm{S}}}\mathbf{G}_{\mathrm{io}}\mathbf{G}_{\mathrm{ci}}\right] \hat{\mathbf{d}} \tag{2.99}$$

Each of the source-affected transfer function can be solved from (2.98) and (2.99) by utilizing basic matrix algebra. Transfer functions related to the inverter input dynamics are given in (2.100) – (2.104) where the superscript 'S' denotes that the transfer function is affected by the output admittance of the source.

$$Z_{\mathrm{in}}^{\mathrm{S}} = \frac{\hat{u}_{\mathrm{dc}}}{\hat{i}_{\mathrm{dc}}} = \frac{Z_{\mathrm{in}}}{1 + Y_{\mathrm{S}} Z_{\mathrm{in}}} \tag{2.100}$$

$$T_{\mathrm{oi\text{-}d}}^{\mathrm{S}} = \frac{\hat{u}_{\mathrm{dc}}}{\hat{u}_{\mathrm{od}}} = \frac{T_{\mathrm{oi\text{-}d}}}{1 + Y_{\mathrm{S}} Z_{\mathrm{in}}} \tag{2.101}$$

$$T_{\mathrm{oi\text{-}q}}^{\mathrm{S}} = \frac{\hat{u}_{\mathrm{dc}}}{\hat{u}_{\mathrm{oq}}} = \frac{T_{\mathrm{oi\text{-}q}}}{1 + Y_{\mathrm{S}} Z_{\mathrm{in}}} \tag{2.102}$$

$$G_{\mathrm{ci\text{-}d}}^{\mathrm{S}} = \frac{\hat{u}_{\mathrm{dc}}}{\hat{d}_{\mathrm{d}}} = \frac{G_{\mathrm{ci\text{-}d}}}{1 + Y_{\mathrm{S}} Z_{\mathrm{in}}} \tag{2.103}$$

$$G_{\mathrm{ci\text{-}q}}^{\mathrm{S}} = \frac{\hat{u}_{\mathrm{dc}}}{\hat{d}_{\mathrm{q}}} = \frac{G_{\mathrm{ci\text{-}q}}}{1 + Y_{\mathrm{S}} Z_{\mathrm{in}}} \tag{2.104}$$

The source-affected transfer functions of the inverter related to the output dynamics

of the d-component are as given in (2.105) – (2.113).

$$G^{\mathrm{S}}_{\text{io-d}} = \frac{\hat{i}_{\mathrm{od}}}{\hat{i}_{\mathrm{dcS}}} = \frac{G_{\text{io-d}}}{1 + Y_{\mathrm{S}} Z_{\mathrm{in}}} \tag{2.105}$$

$$Y^{\mathrm{S}}_{\text{o-d}} = -\frac{\hat{i}_{\mathrm{od}}}{\hat{u}_{\mathrm{od}}} = \frac{1 + Y_{\mathrm{S}} Z_{\text{in-d-oc}}}{1 + Y_{\mathrm{S}} Z_{\mathrm{in}}} Y_{\text{o-d}} \tag{2.106}$$

$$Y^{\mathrm{S}}_{\text{o-qd}} = -\frac{\hat{i}_{\mathrm{od}}}{\hat{u}_{\mathrm{oq}}} = \frac{1 + Y_{\mathrm{S}} Z_{\text{in-qd-oc}}}{1 + Y_{\mathrm{S}} Z_{\mathrm{in}}} Y_{\text{o-qd}} \tag{2.107}$$

$$G^{\mathrm{S}}_{\text{co-d}} = \frac{\hat{i}_{\mathrm{od}}}{\hat{d}_{\mathrm{d}}} = \frac{1 + Y_{\mathrm{S}} Z_{\text{in-d-}\infty}}{1 + Y_{\mathrm{S}} Z_{\mathrm{in}}} G_{\text{co-d}} \tag{2.108}$$

$$G^{\mathrm{S}}_{\text{co-qd}} = \frac{\hat{i}_{\mathrm{od}}}{\hat{d}_{\mathrm{q}}} = \frac{1 + Y_{\mathrm{S}} Z_{\text{in-qd-}\infty}}{1 + Y_{\mathrm{S}} Z_{\mathrm{in}}} G_{\text{co-qd}} \tag{2.109}$$

$$Z_{\text{in-d-oco}} = Z_{\mathrm{in}} + \frac{T_{\text{oi-d}} G_{\text{io-d}}}{Y_{\text{o-d}}} \tag{2.110}$$

$$Z_{\text{in-qd-oco}} = Z_{\mathrm{in}} + \frac{T_{\text{oi-q}} G_{\text{io-d}}}{Y_{\text{o-qd}}} \tag{2.111}$$

$$Z^{\mathrm{d}}_{\text{in-}\infty} = Z_{\mathrm{in}} - \frac{G_{\text{ci-d}} G_{\text{io-d}}}{G_{\text{co-d}}} \tag{2.112}$$

$$Z^{\mathrm{qd}}_{\text{in-}\infty} = Z_{\mathrm{in}} - \frac{G_{\text{ci-q}} G_{\text{io-d}}}{G_{\text{co-qd}}} \tag{2.113}$$

The source-affected transfer functions of the inverter related to the output dynamics of the q-component are given in (2.114) – (2.122).

$$G^{\mathrm{S}}_{\text{io-q}} = \frac{\hat{i}_{\mathrm{oq}}}{\hat{i}_{\mathrm{dcS}}} = \frac{G_{\text{io-q}}}{1 + Y_{\mathrm{S}} Z_{\mathrm{in}}} \tag{2.114}$$

$$Y^{\mathrm{S}}_{\text{o-dq}} = -\frac{\hat{i}_{\mathrm{oq}}}{\hat{u}_{\mathrm{od}}} = \frac{1 + Y_{\mathrm{S}} Z_{\text{in-dq-oc}}}{1 + Y_{\mathrm{S}} Z_{\mathrm{in}}} Y_{\text{o-dq}} \tag{2.115}$$

$$Y^{\mathrm{S}}_{\mathrm{oq}} = -\frac{\hat{i}_{\mathrm{oq}}}{\hat{u}_{\mathrm{oq}}} = \frac{1 + Y_{\mathrm{S}} Z_{\text{in-q-oc}}}{1 + Y_{\mathrm{S}} Z_{\mathrm{in}}} Y_{\text{o-q}} \tag{2.116}$$

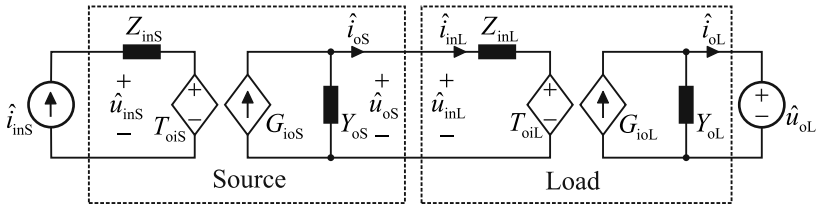

Fig. 2.16: Interconnected DC-DC system.

$$G^{\text{S}}_{\text{co-dq}} = \frac{\hat{i}_{\text{oq}}}{\hat{d}_{\text{d}}} = \frac{1 + Y_{\text{S}} Z_{\text{in-dq-}\infty}}{1 + Y_{\text{S}} Z_{\text{in}}} G_{\text{co-dq}} \tag{2.117}$$

$$G^{\text{S}}_{\text{co-q}} = \frac{\hat{i}_{\text{oq}}}{\hat{d}_{\text{q}}} = \frac{1 + Y_{\text{S}} Z_{\text{in-q-}\infty}}{1 + Y_{\text{S}} Z_{\text{in}}} G_{\text{co-q}} \tag{2.118}$$

$$Z_{\text{in-dq-oco}} = Z_{\text{in}} + \frac{T_{\text{oi-d}} G_{\text{io-q}}}{Y_{\text{o-dq}}} \tag{2.119}$$

$$Z_{\text{in-q-oco}} = Z_{\text{in}} + \frac{T_{\text{oi-q}} G_{\text{io-q}}}{Y_{\text{o-q}}} \tag{2.120}$$

$$Z_{\text{in-dq-}\infty} = Z_{\text{in}} - \frac{G_{\text{ci-d}} G_{\text{io-q}}}{G_{\text{co-dq}}} \tag{2.121}$$

$$Z_{\text{in-q-}\infty} = Z_{\text{in}} - \frac{G_{\text{ci-q}} G_{\text{io-q}}}{G_{\text{co-q}}} \tag{2.122}$$

2.6 Stability analysis of interconnected power electronic systems

The stability of interconnected power electronic systems has been an important research topic from the mid 70's until to date. The stability analysis of a DC-DC converter was first reported in (Middlebrook, 1978).

Fig. 2.16 shows an interconnected system made up of two separate power electronic subsystems denoted as the 'Source' and the 'Load'. The source system could be, e.g., a DC-DC converter and the load system could be its output filter. Any DC-DC converter or filter can be described using four transfer functions between the currents and voltages of the input and output terminals, assuming that all the control loops are closed, i.e., there are no control inputs. The analysis is done assuming the H-parameter model due to the nature of photovoltaic power systems. However, the same principles are valid when G, Y or Z-parameters are used. The transfer functions of the source and load systems are as given in (2.123) and (2.124).

$$\begin{bmatrix} \hat{u}_{\text{inS}} \\ \hat{i}_{\text{oS}} \end{bmatrix} = \begin{bmatrix} Z_{\text{inS}} & T_{\text{oiS}} \\ G_{\text{ioS}} & -Y_{\text{oS}} \end{bmatrix} \begin{bmatrix} \hat{i}_{\text{inS}} \\ \hat{u}_{\text{oS}} \end{bmatrix} \tag{2.123}$$

$$\begin{bmatrix} \hat{u}_{\text{inL}} \\ \hat{i}_{\text{oL}} \end{bmatrix} = \begin{bmatrix} Z_{\text{inL}} & T_{\text{oiL}} \\ G_{\text{ioL}} & -Y_{\text{oL}} \end{bmatrix} \begin{bmatrix} \hat{i}_{\text{inL}} \\ \hat{u}_{\text{oL}} \end{bmatrix} \tag{2.124}$$

The currents and voltages at the interface between the source and the load are the same as defined in (2.125). The two systems can be merged together by solving the mapping between the input variables $\hat{i}_{\text{inS}}$, $\hat{u}_{\text{oL}}$ and the output variables $\hat{u}_{\text{inS}}$, $\hat{i}_{\text{oL}}$ of the interconnected system. The transfer functions that describe the small-signal behavior of the interconnected system are as given in (2.126) where $Y_{\text{oS-sci}}$ and $Z_{\text{inL-oco}}$ are special parameters defined in (2.127) and (2.128).

$$\begin{bmatrix} \hat{u}_{\text{inL}} \\ \hat{i}_{\text{inL}} \end{bmatrix} = \begin{bmatrix} \hat{u}_{\text{oS}} \\ \hat{i}_{\text{oS}} \end{bmatrix} \tag{2.125}$$

$$\begin{bmatrix} \hat{u}_{\text{inS}} \\ \\ \hat{i}_{\text{oL}} \end{bmatrix} = \begin{bmatrix} \dfrac{(1 + Z_{\text{inL}} Y_{\text{oS-sci}})}{1 + Y_{\text{oS}} Z_{\text{inL}}} Z_{\text{inS}} & \dfrac{T_{\text{oiS}} T_{\text{oiL}}}{1 + Y_{\text{oS}} Z_{\text{inL}}} \\ \dfrac{G_{\text{ioS}} G_{\text{ioL}}}{1 + Y_{\text{oS}} Z_{\text{inL}}} & \dfrac{(1 + Y_{\text{oS}} Z_{\text{inL-oco}})}{1 + Y_{\text{oS}} Z_{\text{inL}}} Y_{\text{oL}} \end{bmatrix} \begin{bmatrix} \hat{i}_{\text{inS}} \\ \\ \hat{u}_{\text{oL}} \end{bmatrix} \tag{2.126}$$

$$Y_{\text{oS-sci}} = Y_{\text{oS}} + \frac{T_{\text{oiS}} G_{\text{ioS}}}{Z_{\text{inS}}} \tag{2.127}$$

$$Z_{\text{inL-oco}} = Z_{\text{inL}} + \frac{G_{\text{ioL}} T_{\text{oiL}}}{Y_{\text{oL}}} \tag{2.128}$$

The denominator of all transfer functions in (2.126) include the same term $Y_{\text{oS}} Z_{\text{inL}}$ which is commonly known as the minor loop gain (Leppäaho and Suntio, 2011). The stability of the interconnected system can be evaluated by plotting the minor-loop gain in the complex plane. The number of right-half-plane (RHP) zeros and poles found in the minor loop gain can be evaluated by inspecting the encirclements of the contour around the critical point (-1,0) in the complex plane as defined in (2.129). N is the number of encirclements in clockwise direction, N_{zeros} is the number of RHP-zeros and N_{poles} is the

number of RHP-poles. The system has an unstable pole if the contour encircles the point (-1,0) in clockwise direction, assuming there are no RHP-poles in the minor loop gain.

$$N = N_{\text{zeros}} - N_{\text{poles}} \tag{2.129}$$

The Nyquist stability criterion has been applied successfully for three-phase systems (Wen et al., 2012) and single-phase systems (Sun, 2011). The impedances of single-phase systems can be defined in phase-domain and used directly in the stability analysis. However, a three-phase system which is analysed in the synchronous reference frame has multiple inputs and outputs and requires special consideration.

The transfer functions that describe the input and output dynamics of a three-phase inverter are shown in (2.130) and (2.131) when all the control loops are closed.

$$\hat{u}_{\text{inS}} = Z_{\text{inS}}\hat{i}_{\text{inS}} + \overbrace{\begin{bmatrix} T_{\text{oiS-d}} & T_{\text{oiS-q}} \end{bmatrix}}^{\mathbf{T}_{\text{oiS}}} \overbrace{\begin{bmatrix} \hat{u}_{\text{oS-d}} \\ \hat{u}_{\text{oS-q}} \end{bmatrix}}^{\hat{\mathbf{u}}_{\text{oS}}} \tag{2.130}$$

$$\overbrace{\begin{bmatrix} \hat{i}_{\text{o-d}} \\ \hat{i}_{\text{o-q}} \end{bmatrix}}^{\hat{\mathbf{i}}_{\text{oS}}} = \overbrace{\begin{bmatrix} G_{\text{ioS-d}} \\ G_{\text{ioS-q}} \end{bmatrix}}^{\mathbf{G}_{\text{ioS}}} \hat{i}_{\text{inS}} - \overbrace{\begin{bmatrix} Y_{\text{oS-d}} & Y_{\text{oS-qd}} \\ Y_{\text{oS-dq}} & Y_{\text{oS-q}} \end{bmatrix}}^{\mathbf{Y}_{\text{oS}}} \overbrace{\begin{bmatrix} \hat{u}_{\text{oS-d}} \\ \hat{u}_{\text{oS-q}} \end{bmatrix}}^{\hat{\mathbf{u}}_{\text{oS}}} \tag{2.131}$$

Transfer function matrix of a three-phase load, such as a three-phase filter was given solved using (2.2). The matrix can be divided into submatrices which describe the input and output dynamics of the filter as in (2.132) and (2.133), respectively.

$$\begin{aligned} \overbrace{\begin{bmatrix} \hat{u}_{\text{inL-d}} \\ \hat{u}_{\text{inL-q}} \end{bmatrix}}^{\hat{\mathbf{u}}_{\text{inL}}} = & \overbrace{\begin{bmatrix} Z_{\text{inL-d}} & Z_{\text{inL-qd}} \\ Z_{\text{inL-dq}} & Z_{\text{inL-q}} \end{bmatrix}}^{\mathbf{Z}_{\text{inL}}} \overbrace{\begin{bmatrix} \hat{i}_{\text{inL-d}} \\ \hat{i}_{\text{inL-q}} \end{bmatrix}}^{\hat{\mathbf{i}}_{\text{inL}}} \\ & + \overbrace{\begin{bmatrix} T_{\text{oiL-d}} & T_{\text{oiL-qd}} \\ T_{\text{oiL-dq}} & T_{\text{oiL-q}} \end{bmatrix}}^{\mathbf{T}_{\text{oiL}}} \overbrace{\begin{bmatrix} \hat{u}_{\text{oL-d}} \\ \hat{u}_{\text{oL-q}} \end{bmatrix}}^{\hat{\mathbf{u}}_{\text{oL}}} \end{aligned} \tag{2.132}$$

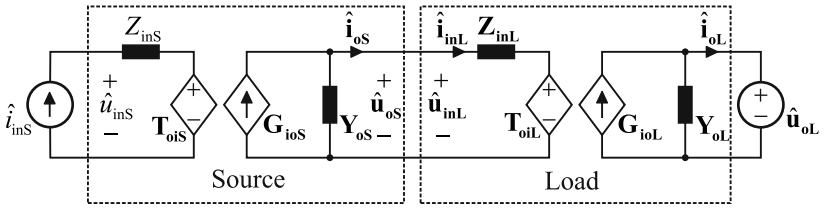

Fig. 2.17: Interconnected three-phase system.

$$\overbrace{\begin{bmatrix} \hat{i}_{\text{oL-d}} \\ \hat{i}_{\text{oL-q}} \end{bmatrix}}^{\hat{\mathbf{i}}_{\text{oL}}} = \overbrace{\begin{bmatrix} G_{\text{ioL-d}} & G_{\text{ioL-qd}} \\ G_{\text{ioL-dq}} & G_{\text{ioL-q}} \end{bmatrix}}^{\mathbf{G}_{\text{ioL}}} \overbrace{\begin{bmatrix} \hat{i}_{\text{inL-d}} \\ \hat{i}_{\text{inL-q}} \end{bmatrix}}^{\hat{\mathbf{i}}_{\text{inL}}} - \overbrace{\begin{bmatrix} Y_{\text{oL-d}} & Y_{\text{oL-qd}} \\ Y_{\text{oL-dq}} & Y_{\text{oL-q}} \end{bmatrix}}^{\mathbf{Y}_{\text{oL}}} \overbrace{\begin{bmatrix} \hat{u}_{\text{oL-d}} \\ \hat{u}_{\text{oL-q}} \end{bmatrix}}^{\hat{\mathbf{u}}_{\text{oL}}} \tag{2.133}$$

The interconnected three-phase system comprising of a three-phase inverter and an output filter can be constructed based on (2.132) and (2.133) and is depicted in Fig. 2.17. The matrix-valued components and variables are denoted using boldface font.

The input and output dynamics of the interconnected system can be solved from Fig. 2.17 by utilizing basic matrix algebra and by noting that the currents and voltages at the interface between the systems are the same. The input and output dynamics of the system are as given in (2.134) and (2.135).

$$\begin{aligned} \hat{u}_{\text{inS}} = &\left(Z_{\text{inS}} + \mathbf{T}_{\text{oiS}} \left[\mathbf{I} + \mathbf{Z}_{\text{inL}} \mathbf{Y}_{\text{oS}} \right]^{-1} \mathbf{Z}_{\text{inL}} \mathbf{G}_{\text{ioS}} \right) \hat{i}_{\text{inS}} \\ &+ \left(\mathbf{T}_{\text{oiS}} \left[\mathbf{I} + \mathbf{Z}_{\text{inL}} \mathbf{Y}_{\text{oS}} \right]^{-1} \mathbf{T}_{\text{oiL}} \right) \hat{\mathbf{u}}_{\text{oL}} \end{aligned} \tag{2.134}$$

$$\begin{aligned} \hat{\mathbf{i}}_{\text{oL}} = &\mathbf{G}_{\text{ioL}} \left[\mathbf{I} + \mathbf{Y}_{\text{oS}} \mathbf{Z}_{\text{inL}} \right]^{-1} \mathbf{G}_{\text{ioS}} \hat{i}_{\text{inS}} \\ &- \left(\mathbf{Y}_{\text{oL}} + \mathbf{G}_{\text{ioL}} \left[\mathbf{I} + \mathbf{Y}_{\text{oS}} \mathbf{Z}_{\text{inL}} \right]^{-1} \mathbf{Y}_{\text{oS}} \mathbf{T}_{\text{oiL}} \right) \mathbf{u}_{\text{oL}} \end{aligned} \tag{2.135}$$

The input and output dynamics of the interconnected system can be divided into four matrix-valued transfer functions as given in (2.136) – (2.139).

$$\mathbf{Z}_{\text{inSL}} = Z_{\text{inS}} + \mathbf{T}_{\text{oiS}} \left[\mathbf{I} + \mathbf{Z}_{\text{inL}} \mathbf{Y}_{\text{oS}} \right]^{-1} \mathbf{Z}_{\text{inL}} \mathbf{G}_{\text{ioS}} \tag{2.136}$$

$$\mathbf{T}_{\mathrm{oiSL}} = \mathbf{T}_{\mathrm{oiS}} \left[\mathbf{I} + \mathbf{Z}_{\mathrm{inL}} \mathbf{Y}_{\mathrm{oS}}\right]^{-1} \mathbf{T}_{\mathrm{oiL}} \tag{2.137}$$

$$\mathbf{G}_{\mathrm{ioSL}} = \mathbf{G}_{\mathrm{ioL}} \left[\mathbf{I} + \mathbf{Y}_{\mathrm{oS}} \mathbf{Z}_{\mathrm{inL}}\right]^{-1} \mathbf{G}_{\mathrm{ioS}} \tag{2.138}$$

$$\mathbf{Y}_{\mathrm{oSL}} = \mathbf{Y}_{\mathrm{oL}} + \mathbf{G}_{\mathrm{ioL}} \left[\mathbf{I} + \mathbf{Y}_{\mathrm{oS}} \mathbf{Z}_{\mathrm{inL}}\right]^{-1} \mathbf{Y}_{\mathrm{oS}} \mathbf{T}_{\mathrm{oiL}} \tag{2.139}$$

All the transfer functions include an inverse matrix which contains the product of the output admittance matrix of the source $\mathbf{Y}_{\mathrm{oS}}$ and the input impedance matrix of the load $\mathbf{Z}_{\mathrm{inL}}$ as shown in (2.140) and (2.141). The matrices look very similar to the minor loop gain in (2.126). However, analysing the stability of a multivariable system is not as straightforward as for the DC-DC converters. The stability can be evaluated by plotting the eigenvalues of the matrices (2.140) and (2.141) in the complex plane as a function of frequency. This is, however, time consuming and requires iterative algorithms as discussed in (MacFarlane and Postlethwaite, 1977) and (Belkhayat, 1997).

$$\left[\mathbf{I} + \mathbf{Z}_{\mathrm{inL}} \mathbf{Y}_{\mathrm{oS}}\right]^{-1} = \left(\begin{bmatrix} 1 & 0 \\ 0 & 1 \end{bmatrix} + \begin{bmatrix} Z_{\mathrm{inL\text{-}d}} & Z_{\mathrm{inL\text{-}qd}} \\ Z_{\mathrm{inL\text{-}dq}} & Z_{\mathrm{inL\text{-}q}} \end{bmatrix} \begin{bmatrix} Y_{\mathrm{oS\text{-}d}} & Y_{\mathrm{oS\text{-}qd}} \\ Y_{\mathrm{oS\text{-}dq}} & Y_{\mathrm{oS\text{-}q}} \end{bmatrix} \right)^{-1} \tag{2.140}$$

$$\left[\mathbf{I} + \mathbf{Y}_{\mathrm{oS}} \mathbf{Z}_{\mathrm{inL}}\right]^{-1} = \left(\begin{bmatrix} 1 & 0 \\ 0 & 1 \end{bmatrix} + \begin{bmatrix} Y_{\mathrm{oS\text{-}d}} & Y_{\mathrm{oS\text{-}qd}} \\ Y_{\mathrm{oS\text{-}dq}} & Y_{\mathrm{oS\text{-}q}} \end{bmatrix} \begin{bmatrix} Z_{\mathrm{inL\text{-}d}} & Z_{\mathrm{inL\text{-}qd}} \\ Z_{\mathrm{inL\text{-}dq}} & Z_{\mathrm{inL\text{-}q}} \end{bmatrix} \right)^{-1} \tag{2.141}$$

Fortunately, the analysis can be simplified if the cross-coupling terms between the d and q-components can be neglected, as discussed e.g., in Burgos et al. (2010). Neglecting the cross-coupling impedances and admittances yields the same result for both inverse matrices as shown in (2.142).

$$\left[\mathbf{I} + \mathbf{Z}_{\mathrm{inL}} \mathbf{Y}_{\mathrm{oS}}\right]^{-1} = \left[\mathbf{I} + \mathbf{Y}_{\mathrm{oS}} \mathbf{Z}_{\mathrm{inL}}\right]^{-1} = \begin{bmatrix} \dfrac{1}{1 + Y_{\mathrm{oS\text{-}d}} \cdot Z_{\mathrm{inL\text{-}d}}} & 0 \\ 0 & \dfrac{1}{1 + Y_{\mathrm{oS\text{-}q}} \cdot Z_{\mathrm{inL\text{-}q}}} \end{bmatrix} \tag{2.142}$$

As can be seen in (2.142) the problem reduces to analysing the stability of two inde-

pendent minor loop gains which can be done using the Nyquist stability criterion. The stability of both of the minor loop gains (2.143) and (2.144) shall be verified.

$$L_{\mathrm{d}} = Y_{\mathrm{oS\text{-}d}} Z_{\mathrm{inL\text{-}d}} = Z_{\mathrm{inL\text{-}d}} / Z_{\mathrm{oS\text{-}d}} \tag{2.143}$$

$$L_{\mathrm{q}} = Y_{\mathrm{oS\text{-}q}} Z_{\mathrm{inL\text{-}q}} = Z_{\mathrm{inL\text{-}q}} / Z_{\mathrm{oS\text{-}q}} \tag{2.144}$$

3 EFFECT OF THE VOLTAGE-BOOSTING DC-DC CONVERTER ON THE DC-LINK CONTROL

This chapter discusses the effect of an upstream voltage-boosting DC-DC converter on dynamics of the PV inverter. A short literature review specific to the topic is performed in the beginning. The modeling methods introduced in Chapter 2 are utilized to capture the dynamics of the DC-DC converter and the inverter in order to include the effect of the nonideal source (DC-DC converter) on the dynamics of the inverter. The minimum DC-link capacitance value, which is required for stable operation is discussed and the stabilizing effect of the input-voltage control of the DC-DC converter is shown.

3.1 Introduction

The PV generator is often interfaced to the utility grid using a two-stage inverter (Ho et al., 2013; Ji et al., 2011; Vighetti et al., 2012). The inverter comprises of a voltage-boosting DC-DC converter followed by a three-phase inverter as shown in Fig. 3.1. The DC-DC stage allows the PV generator to be operated at lower voltages than in case of single-stage inverter because the PV voltage is not anymore constrained by the peak of the grid voltage. Operating the PV generator in a wider voltage range allows global maximum power point to be tracked in partial shading conditions and gives the designer more freedom in selecting the PV module configuration.

The DC-DC converter is most often based on the conventional voltage-fed boost converter due to the fact that its input current is continuous (Xiao et al., 2007). The DC-DC converter is derived from the conventional voltage-fed boost converter by adding an input capacitor for correct interfacing with the PV generator (Leppäaho et al., 2010). A single boost converter can be used (Urtasun et al., 2013) or, alternatively, several boost converters can be connected in parallel and operated in an interleaved mode (Ho et al., 2013; Jung et al., 2011) which reduces the current ripple in the inductors and, therefore, improves the efficiency. However, the interleaved boost converter is out of the scope of this thesis but would be an interesting topic to look into in the future.

The PV generator is a nonideal source with a finite output impedance as discussed in Chapter 1. The dynamics of the DC-DC converter are affected by the dynamic resistance of the PV generator r_{pv} and by the operating point. The effect of the PV generator in the

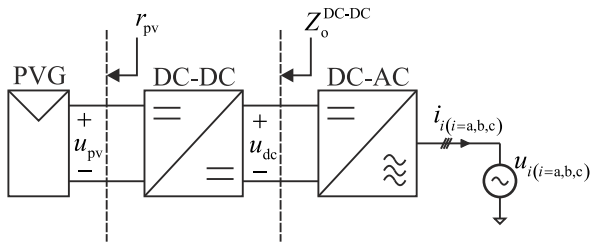

Fig. 3.1: Two-stage photovoltaic inverter.

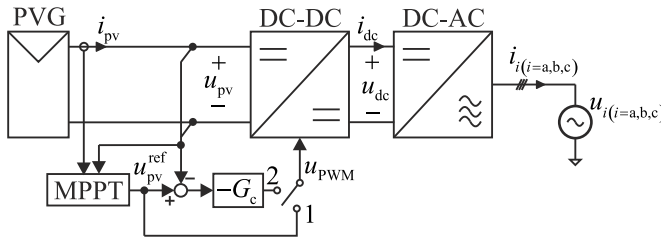

Fig. 3.2: Control modes of the DC-DC stage.

control performance of the boost converter was studied in (Urtasun et al., 2013) where an adaptive controller was proposed to maintain the control performance at all operating points along the IU-curve. However, the effect of the boost converter on the dynamics of a three-phase inverter has not yet been extensively studied in the literature. The dynamics of the inverter are affected by the output impedance of the DC-DC converter $Z_{\mathrm{o}}^{\mathrm{DC\text{-}DC}}$ which depends on the output impedance of the PV generator r_{pv} and on the control mode of the DC-DC converter.

The boost converter is usually operated at open loop (Chen and Lin, 2014; Jung et al., 2011; Yang et al., 2010) or under input-voltage control as, e.g, in (Femia et al., 2009). Alternatively, the inductor current control and input-voltage control can be cascaded together as done, e.g., in (Jung et al., 2011) but this is out of the scope of this thesis. The two control schemes of the DC-DC stage studied in this thesis are illustrated in Fig. 3.2. The duty ratio of the DC-DC converter can be defined directly by the MPPT-algorithm (switch in position 1) which is referred as the open-loop control mode or, alternatively, the MPPT-algorithm can define a reference value for the input-voltage controller G_{c} (switch in position 2) which regulates the voltage of the PV generator u_{pv} through a feedback loop.

3.2 DC-DC converter in the open-loop control mode

3.2.1 Output impedance of the DC-DC converter at open loop

The output admittance of the DC-DC converter can be solved using the methods presented in Chapter 2 when the converter operates in open-loop control mode. The detailed derivation can be found in (Messo, Jokipii and Suntio, 2012). The source-affected output admittance can be solved by using (3.1) where the output impedance of the PV generator is approximated by its low-frequency value, i.e., by the dynamic resistance r_{pv}.

$$Y_{\mathrm{o}}^{\mathrm{DC\text{-}DC}} = \frac{1}{Z_{\mathrm{o}}^{\mathrm{DC\text{-}DC}}} = \frac{1 + \frac{1}{r_{\mathrm{pv}}}\left(Z_{\mathrm{in\text{-}o}} + \frac{G_{\mathrm{io\text{-}o}}T_{\mathrm{oi\text{-}o}}}{Y_{\mathrm{o\text{-}o}}}\right)}{1 + \frac{1}{r_{\mathrm{pv}}}Z_{\mathrm{in\text{-}o}}} \tag{3.1}$$

The low-frequency value of the output admittance can be solved symbolically and is given in (3.2) as an impedance. The dynamic resistance clearly affects the shape of the output impedance of the DC-DC converter.

$$Z_{\mathrm{o}}^{\mathrm{DC\text{-}DC}}(\mathrm{j}\omega = 0) = \frac{r_{\mathrm{pv}} + r_{\mathrm{L1}} + D'r_{\mathrm{D}} + Dr_{\mathrm{sw}}}{D'^2} \approx \frac{r_{\mathrm{pv}}}{D'^2} \tag{3.2}$$

An experimental prototype operating at reduced voltages was used to verify the shape of the output impedance. The power stage of the converter is depicted in Fig. 3.3. An additional output capacitor C_2 was added to protect the diode from the current spikes originating from the parasitic inductance of the output connections. The parameters of the experimental DC-DC converter and the PV generator are shown in Table 3.1. The converter was fed from a solar array simulator (SAS) model E4360 manufactured by Agilent which is known to replicate the dynamics of a real PV generator accurately (Nousiainen et al., 2013). An electronic voltage-type load manufactured by Chroma was connected at the output terminals. Pulse signal for the switch was generated using a digital signal processor (DSP) model TMSF28335 manufactured by Texas Instruments. Frequency response analyzer with an impedance measurement kit manufactured by Venable Instruments Inc. Model 3120 was used to measure the output impedance of the DC-DC converter.

The additional output capacitor can be included in the output admittance of the DC-DC converter by using basic circuit theory as in (3.3) since the capacitor is connected in parallel with the output terminals. The admittance of the capacitor can be given as shown in (3.4).

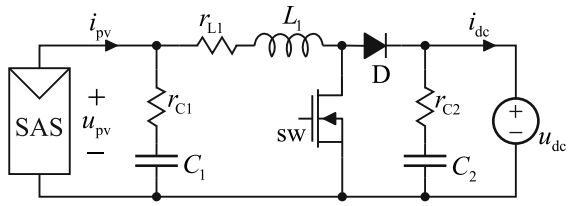

Fig. 3.3: Power stage of the voltage-boosting DC-DC converter.

Table 3.1: Parameters of the experimental converter and the PV generator

U_{MPP}	20 V	U_{dc}	30 V	r_{C2}	30 mΩ
U_{oc}	25 V	C_1	100 μF	L_1	320 mH
I_{MPP}	1.5 A	C_2	100 μF	r_{L1}	250 mΩ
I_{sc}	1.65 A	r_{C1}	50 mΩ	f_{s}	75 kHz

$$Y_{\text{o-C2}}^{\text{DC-DC}} = Y_{\text{o}}^{\text{DC-DC}} + Y_{\text{C2}}, \tag{3.3}$$

$$Y_{\text{C2}} = \frac{sC_2}{1 + sr_{\text{C2}}C_2}. \tag{3.4}$$

The source-affected output impedance of the DC-DC converter was measured at three operating points along the IU-curve of the PV generator; in CC and CV regions and at the MPP. The measured and predicted output impedances are as shown in Fig. 3.4. The low-frequency gain of the output impedance equals the dynamic resistance scaled by the inverse of the complementary duty ratio as given in (3.2). The magnitude of the output impedance is the largest in the CC region and the smallest in the CV region. At the MPP the low-frequency gain is approximately the ratio of the output voltage and current of the DC-DC converter $U_{\mathrm{dc}}/I_{\mathrm{dc}}$. In other words, the DC-DC converter operating in open-loop control mode reflects the dynamic resistance of the PV generator to its output terminals.

3.2.2 Effect of open-loop-controlled DC-DC converter on DC-link control dynamics

The effect of the DC-DC stage on the control dynamics of the inverter can be solved using the methods derived in Chapter 2 and presented in (Messo, Puukko and Suntio, 2012). The source-affected transfer function from the d-component of the duty ratio $\hat{d}_{\mathrm{d}}$ to

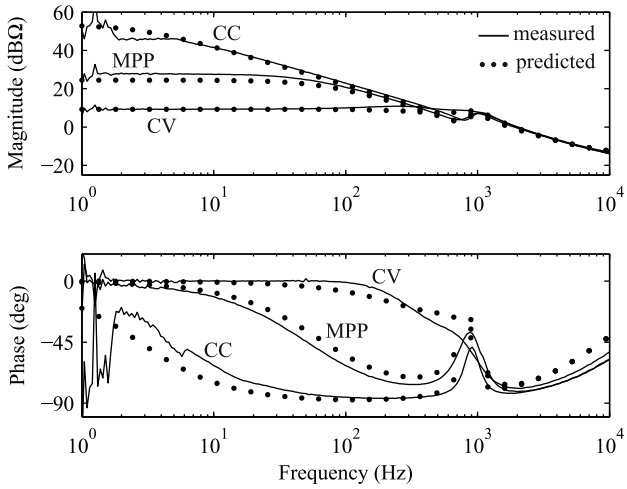

Fig. 3.4: Measured and predicted output impedances of the DC-DC converter at open loop.

the d-component of the output current $\hat{i}_{\mathrm{od}}$ can be solved using (2.108). In the following symbolic analysis, the source impedance affecting the transfer function is approximated by the low-frequency output impedance of the DC-DC converter (3.2). However, in the predicted frequency responses the complete output impedance with all the parasitics is used. The source-affected control-to-output-current transfer function $G_{\mathrm{co\text{-}d}}^{\mathrm{S\text{-}OL}}$ is as given in (3.5) without parasitics where the superscript 'OL' refers to the open-loop control mode of the DC-DC converter. The denominator of the transfer function is as given in (3.6).

$$G_{\mathrm{co\text{-}d}}^{\mathrm{S\text{-}OL}} = \frac{\hat{i}_{\mathrm{od}}}{\hat{d}_{\mathrm{d}}} = \frac{U_{\mathrm{dc}}}{L} s \left[s + \frac{D'^2}{C_{\mathrm{dc}}} \left(\frac{1}{r_{\mathrm{pv}}} - \frac{I_{\mathrm{pv}}}{U_{\mathrm{pv}}} \right) \right] \frac{1}{\Delta^{\mathrm{S\text{-}OL}}}, \tag{3.5}$$

$$\Delta^{\mathrm{S\text{-}OL}} = s^3 + \frac{D'^2}{C_{\mathrm{dc}} r_{\mathrm{pv}}} s^2 + \left[\frac{3\left(D_{\mathrm{d}}^2 + D_{\mathrm{q}}^2\right)}{2 C_{\mathrm{dc}} L} + \omega_{\mathrm{s}}^2 \right] s + \frac{D'^2 \omega_{\mathrm{s}}^2}{r_{\mathrm{pv}} C_{\mathrm{dc}}}. \tag{3.6}$$

The control-to-output-current transfer function (3.5) contains a low-frequency zero which is given by (3.7). The zero is located on the right-half of the complex-plane when the PV generator operates in the CC region, i.e., when the dynamic resistance is larger than the static resistance ($r_{\mathrm{pv}} > U_{\mathrm{pv}}/I_{\mathrm{pv}}$). On the other hand, the zero is shifted to the left-half of the complex-plane when the PV generator operates in the CV region, i.e., when the dynamic resistance is smaller than the static resistance ($r_{\mathrm{pv}} < U_{\mathrm{pv}}/I_{\mathrm{pv}}$). At the MPP, the value of dynamic resistance equals the static resistance $U_{\mathrm{pv}}/I_{\mathrm{pv}}$ and the

zero is located at the origin.

$$\omega_{\text{z-OL}} = \frac{D'^2}{C_{\text{dc}}} \left(\frac{I_{\text{pv}}}{U_{\text{pv}}} - \frac{1}{r_{\text{pv}}} \right) \tag{3.7}$$

The source-affected DC-link voltage control loop gain $L_{\text{dc}}^{\text{S-OL}}$ is as given in (3.8). The source-affected control-to-input-voltage transfer function $G_{\text{ci-d}}^{\text{S-OL}}$ can be solved using (2.103) and the source-affected current control loop $L_{\text{out-d}}^{\text{S-OL}}$ can be solved according to (3.9).

$$L_{\text{dc}}^{\text{S-OL}} = -\frac{H_{\text{v}}}{H_{\text{d}}} \cdot \frac{L_{\text{out-d}}^{\text{S-OL}}}{1 + L_{\text{out-d}}^{\text{S-OL}}} \cdot \frac{G_{\text{ci-d}}^{\text{S-OL}}}{G_{\text{co-d}}^{\text{S-OL}}} \cdot G_{\text{cv}} \tag{3.8}$$

$$L_{\text{out-d}}^{\text{S-OL}} = G_{\text{co-d}}^{\text{S-OL}} \cdot G_{\text{PWM}} \cdot G_{\text{cd}} \cdot H_{\text{d}}. \tag{3.9}$$

The DC-link voltage control loop gain can be approximated as in (3.10) at the frequencies lower than the crossover frequency of the current control loop $L_{\text{out-d}}^{\text{S-OL}}$ because the second term in (3.8) is close to unity. Therefore, the DC-link voltage control loop gain has a pole approximately at the frequency given by (3.7). Thus, the DC-link voltage control loop gain has a RHP-pole when the PV generator operates in the CC region. Therefore, the DC-link voltage control can become unstable when the operating point of the PV generator shifts to lower voltages, e.g., as a results of operating point perturbation made by the MPPT algorithm.

$$L_{\text{dc}}^{\text{S-OL}} \approx -\frac{H_{\text{v}}}{H_{\text{d}}} \cdot \frac{G_{\text{ci-d}}^{\text{S-OL}}}{G_{\text{co-d}}^{\text{S-OL}}} \cdot G_{\text{cv}} \tag{3.10}$$

3.3 DC-link capacitance design rule

The minimization of the DC-link capacitance has been widely studied in the literature, especially, related to motor drive systems and wind turbine applications (Espí and Castelló, 2013; Gu and Nam, 2006, 2005). Some research has been done in order to minimize the DC-link capacitance in a PV inverter (Kotsopoulus et al., 2001) but the results are not directly applicable when the cascaded control scheme is used since the authors used a predictive controller. Moreover, large DC-link capacitance has been reported to make the control system of a PV inverter more robust when the DC-DC converter operates at open loop (Bratcu et al., 2011) which suggests that there is a minimum value for the DC-link capacitance which is required for stable operation. A design rule for a single-stage PV inverter was proposed in (Puukko, Nousiainen and Suntio, 2011) which has

been extended for a two-stage PV inverter in (Messo, Jokipii, Puukko and Suntio, 2014) and (Messo, Jokipii and Suntio, 2013).

The low-frequency pole in of the DC-link-voltage control loop can be approximated as given in (3.11) by neglecting the conversion losses of the DC-DC converter and by substituting $D' = U_{\mathrm{pv}}/U_{\mathrm{dc}}$ in (3.7). The DC-link voltage U_{dc} is considered as a constant.

$$\omega_{\text{p-OL}} = \frac{1}{U_{\mathrm{dc}}^2 C_{\mathrm{dc}}} \left(P_{\mathrm{pv}} - \frac{U_{\mathrm{pv}}^2}{r_{\mathrm{pv}}} \right) \tag{3.11}$$

The highest frequency of the pole can be approximated by considering the dynamic resistance to be large which makes the second term inside the parenthesis to disappear and yields (3.12).

$$\omega_{\text{p-OL}} = \frac{P_{\mathrm{pv}}}{U_{\mathrm{dc}}^2 C_{\mathrm{dc}}} \tag{3.12}$$

The crossover frequency of the DC-link voltage control loop is recommended to be chosen at least twice the frequency of the RHP-pole which is considered to provide sufficient robustness of the DC-link voltage control (Kolar et al., 2013).

The RHP-pole reaches its highest frequency when the output power of the PV generator equals the maximum power P_{MPP}. Moreover, the maximum irradiance received by the PV generator can be as large as 1.5 times the standard irradiance level, e.g., due to cloud enhancement which affects directly to the maximum power as discussed in (Luoma et al., 2011). The cloud enhancement can be taken into account by using a scaling factor since the output power of the generator with a fixed voltage is directly proportional to the irradiance. The minimum DC-link-capacitance of a two-stage inverter which is required for ensuring the stability is as given in (3.13) where ω_{c} is the crossover frequency of the DC-link voltage control loop and k_{i} is the scaling factor. The minimum required capacitance is directly proportional to the maximum power of the PV generator and inversely proportional to the crossover frequency of the DC-link-voltage control loop gain and the square of the DC-link voltage.

$$C_{\text{dc-min}} = 2 \cdot k_{\mathrm{i}} \cdot \frac{P_{\mathrm{MPP}}}{U_{\mathrm{dc}}^2 \omega_{\mathrm{c}}} \tag{3.13}$$

The minimum value of the required DC-link capacitance of a two-stage grid-connected PV inverter is depicted in Fig. 3.5 as a function of the crossover frequency of the DC-link-voltage control. The minimum capacitance is shown for two different DC-link voltages and the cloud enhancement is neglected ($k_{\mathrm{i}} = 1$). The crossover frequency of the DC-link voltage control has to be limited below 100 Hz since the grid voltages can be unbalanced.

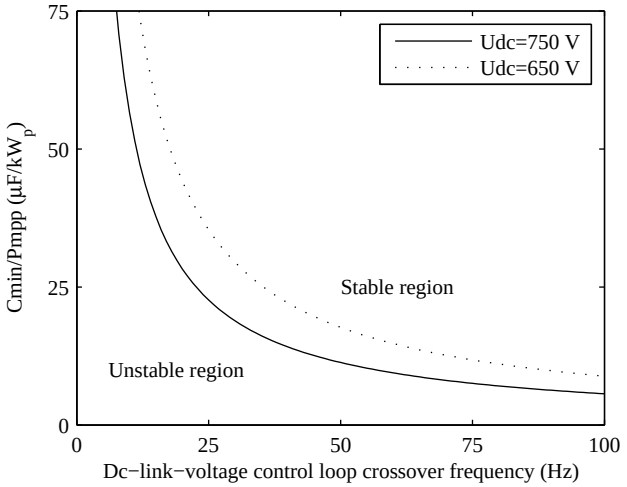

Fig. 3.5: Required DC-link capacitance of a two-stage PV inverter as a function of the crossover frequency of the DC-link-voltage control.

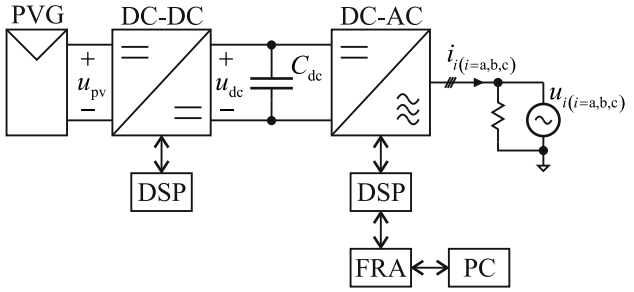

Fig. 3.6: Measurement setup of the two-stage prototype converter.

The unbalanced grid voltages generate ripple at 100 Hz in the DC-link voltage which affects the output current references of the inverter. Thus, the harmonics in the grid current would increase. Setting the crossover frequency at 10 Hz would attenuate the ripple currents by approximately 20 dB which is considered as a sufficient attenuation. The minimum DC-link capacitance, according to Fig. 3.5, is around 90 μF/kW when a DC-link voltage of 650 V is used. Higher DC-link voltage allows using less capacitance in the DC-link. Increasing the DC-link voltage up to 750 V would decrease the minimum capacitance requirement from 90 to 60 μF/kW.

An experimental two-level three-phase inverter operating at reduced voltages was connected at the output of the DC-DC converter to verify the DC-link capacitance design rule. Laboratory equipment and the prototypes used in the thesis are illustrated in

Table 3.2: Parameters of the experimental three-phase inverter.

U_{dc}	30 V	C_{dc}	300 μF	$L_{\mathrm{a,b,c}}$	73 μH
$U_{\mathrm{a,b,c}}$	7.07 $\mathrm{V_{rms}}$	$r_{\mathrm{C\text{-}dc}}$	85 mΩ	$r_{\mathrm{L(a,b,c)}}$	15 mΩ
I_{dc}	1 A	ω_{s}	2·π·50 Hz	f_{s}	75 kHz

Appendix D. Parameters and component values are presented in Table 3.2 where U_{dc} and I_{dc} are the steady-state values of the DC-link voltage and current, $U_{\mathrm{a,b,c}}$ is the RMS-value of the three-phase AC voltage, C_{dc} and $r_{\mathrm{C\text{-}dc}}$ are the capacitance and parasitic resistance of the DC-link capacitor, $L_{\mathrm{a,b,c}}$ and $r_{\mathrm{L(a,b,c)}}$ are the inductance and parasitic resistance of the AC-side inductors, ω_{s} is the angular frequency of the grid and f_{s} is the switching frequency. The measurement setup is depicted in Fig. 3.6. The DC-DC converter was operated with a constant duty ratio at open loop. The inverter was controlled in the synchronous reference frame using the cascaded control scheme. The output currents and voltages were measured once every switching cycle and the measurement circuits include low-pass filters with cut-off frequency at approximately 50 kHz. The DC-DC converter was fed from the same solar array simulator as before and the inverter was loaded by a three-phase voltage source manufactured by Elgar. A three-phase resistive load of 1.2 ohms was connected in parallel with the inverter and the voltage source to dissipate the generated power since the three-phase voltage source could not absorb power. The load resistors were sufficiently large compared with the output impedance of the voltage source and, thus, the effect of the load resistors on the measurements can be neglected. For comparison, the phase impedance of the three-phase voltage source can be approximated as a series connection of a 100 mΩ resistor and a 100 μH inductor.

Transfer function from the DC-link reference voltage $\hat{u}_{\mathrm{dc}}^{\mathrm{ref}}$ to the actual DC-link voltage $\hat{u}_{\mathrm{dc}}$ was measured using the frequency response analyzer (FRA) with the measurement setup depicted in Fig. 3.7 where VC is the DC-link voltage controller and CC the current controller of the d-component. Current control of the q-component and the PLL are not shown in the figure. A small-signal perturbation $\hat{u}_{\mathrm{inj}}$ was added in the reference value of the DC-link voltage $U_{\mathrm{dc}}^{\mathrm{ref}}$ which was then fed to the FRA together with the measured DC-link voltage. The closed-loop transfer function from the reference voltage to the DC-link voltage G_{ref} is as given in (3.14) where $H_{\mathrm{v\text{-}dc}}$ is the DC-link voltage measurement gain and G_{inv} is the frequency response from the error signal of the voltage controller to the actual DC-link voltage.

$$G_{\mathrm{ref}} = \frac{\hat{u}_{\mathrm{dc}}}{\hat{u}_{\mathrm{dc}}^{\mathrm{ref}}} = \frac{G_{\mathrm{inv}}}{1 + H_{\mathrm{v\text{-}dc}} G_{\mathrm{inv}}} \tag{3.14}$$

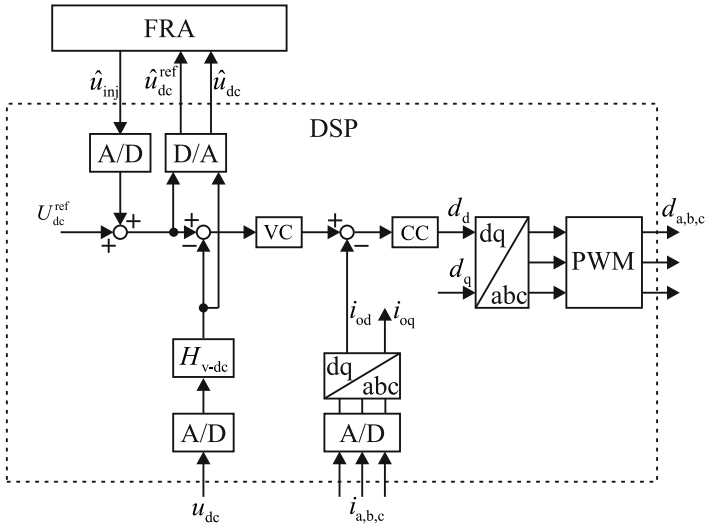

Fig. 3.7: Setup for measuring the DC-link voltage control loop gain.

The sensing gain $H_{\text{v-dc}}$ includes a low-pass filter with a cut-off frequency at half the switching frequency which can be neclegted since the interesting frequency range is well below the switching frequency. The switch signals were generated using the conventional sinusoidal pulse-width modulation (SPWM). The measurement gain and the gains originating from analog-to-digital conversions and pulse-width modulation were manipulated in the code and can be considered to be unity. The transfer function G_{ref} can be approximated as given in (3.15).

$$G_{\text{ref}} = \frac{\hat{u}_{\text{dc}}}{\hat{u}_{\text{dc}}^{\text{ref}}} \approx \frac{G_{\text{inv}}}{1 + G_{\text{inv}}} = \frac{L_{\text{dc}}}{1 + L_{\text{dc}}} \tag{3.15}$$

The DC-link-voltage control loop gain can be solved from (3.15) and is as given in (3.16) where G_{ref} is the measured frequency response. Similar method to extract the loop gain has been previously used in (Figueres et al., 2009).

$$L_{\text{dc}} = \frac{G_{\text{ref}}}{1 - G_{\text{ref}}} \tag{3.16}$$

The DC-link voltage control loop gain was measured in CV and CC regions when the DC-link capacitance was selected equal to 300 μF based on (3.13) and by neglecting the cloud enhancement. The measured and predicted DC-link voltage control loop gains are as shown in Fig. 3.8. The low-frequency phase of the loop gain flips 180 degrees between

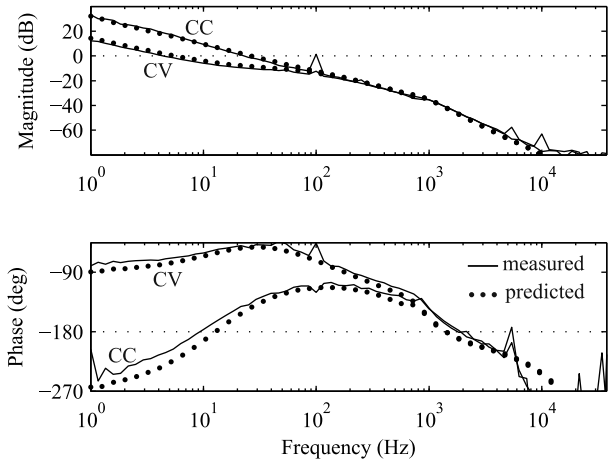

Fig. 3.8: Measured and predicted DC-link voltage control loop gains when the DC-link capacitance is selected based on the proposed design rule.

the two operating regions which indicates that the low-frequency pole of the loop gain shifts between left and right-halves of the complex-plane. The crossover frequency of the loop gain in the CC region is 34 Hz which is approximately twice the frequency of the RHP-pole. The frequency of the RHP-pole was calculated to be 18 Hz. The control system is stable at both operating points since it has always a positive phase margin.

The crossover frequency of the loop gain was intentionally lowered using the same DC-link capacitance value. The crossover frequency was set to 8 Hz in the CC region which is lower than the frequency of the RHP-pole (18 Hz). The measured and predicted loop gains are as shown in Fig. 3.9. The phase margin is negative in the CC region and the DC-link voltage control becomes unstable which is also the reason why the frequency response could not be measured in the CC region. However, the instability is correctly predicted by the small-signal model.

The operating point of the PV generator was slowly moved from the stable CV region toward the unstable CC region by steadily decreasing the duty ratio of the DC-DC converter. The voltage of the solar array simulator, DC-link voltage and the current of phase A (i_{La}) are shown in Fig. 3.10. The DC-link voltage control becomes unstable when the operating point is shifted below the MPP voltage at 20 volts, i.e., in the CC region. The DC-link voltage experiences large oscillation which is reflected in the amplitude of the phase currents due to the use of cascaded control scheme. The DC-link voltage and the amplitude of the phase currents oscillate at 8 Hz which equals the predicted crossover frequency of the unstable DC-link voltage control loop in Fig. 3.9.

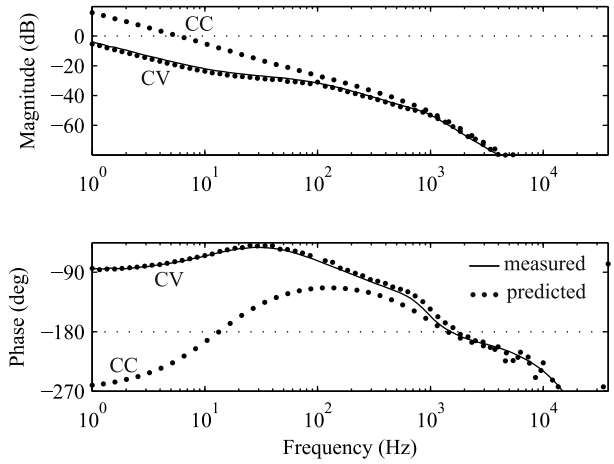

Fig. 3.9: Measured and predicted DC-link voltage control loop gains when the crossover frequency of the voltage control is lowered.

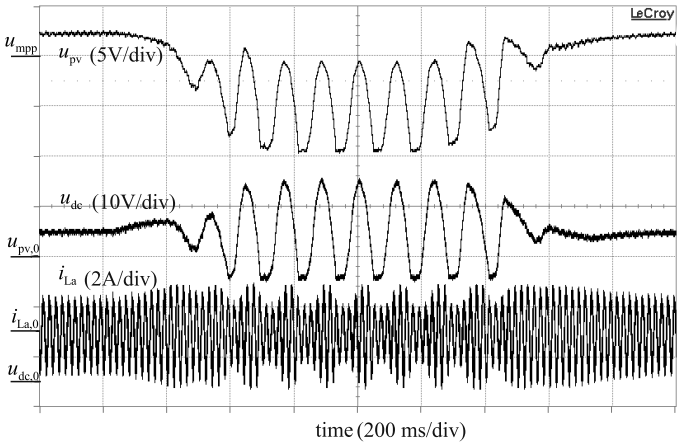

Fig. 3.10: DC-link voltage control becomes unstable in the CC region due to insufficient DC-link capacitance.

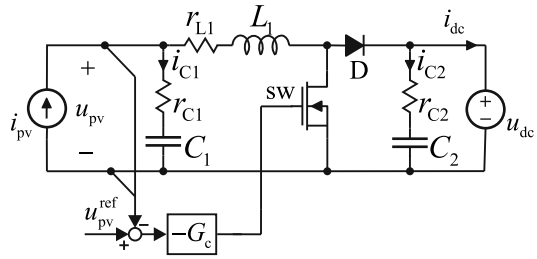

Fig. 3.11: Input-voltage controlled DC-DC converter.

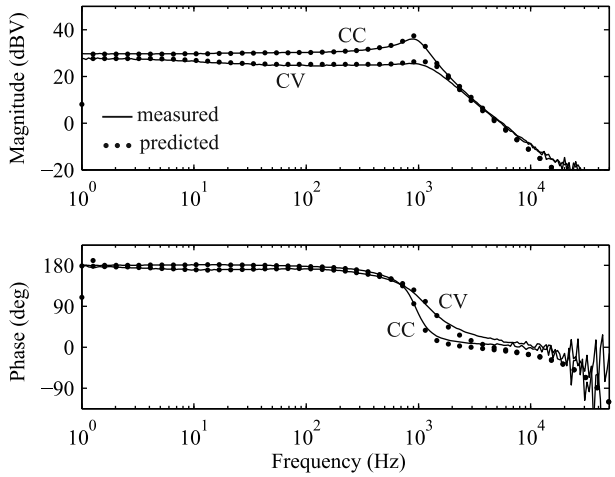

Fig. 3.12: Transfer function from the control variable to PV generator voltage.

3.4 Stabilizing effect of an input-voltage-controlled DC-DC converter

The power stage of the voltage-boosting DC-DC converter is shown in Fig. 3.11. The voltage of the PV generator is controlled using a conventional feedback control employing an integral controller. The reference of the PV voltage $u_{\mathrm{pv}}^{\mathrm{ref}}$ is given by the MPPT-algorithm.

The measured and predicted transfer function from the duty ratio $\hat{d}$ to the input voltage of the DC-DC converter $\hat{u}_{\mathrm{pv}}$ are shown in Fig. 3.12 in CC and CV regions. The phase curve starts from 180 degrees in both regions which means that the control signal has to be inverted by multiplying the output of the controller by -1. The control-to-input-voltage transfer function contains no RHP-zeros or poles which makes the control design of the converter a trivial task.

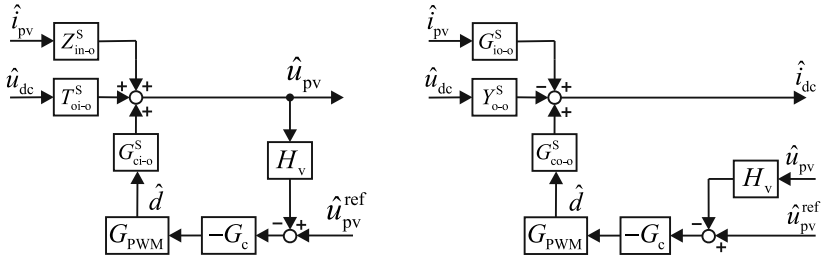

(a) Input dynamics. **(b)** Output dynamics.

Fig. 3.13: Control block diagrams of the DC-DC converter under input-voltage control.

3.4.1 Output impedance of the DC-DC converter under input-voltage control

Control block diagrams which describe the input and output dynamics of the converter can be constructed by using (2.19) and by including the controller G_c and the voltage sensing gain H_v in the control block diagram. The control block diagrams are shown in Fig. 3.13 when the input-voltage control loop is closed. The voltage sensing gain and the modulator gain G_{PWM} are manipulated in the final DSP implementation in such a way that they can be considered to be unity. The superscript 'S' denotes that the transfer functions are affected by the dynamic resistance of the PV generator.

The transfer functions under input-voltage control can be solved from the control block diagrams yielding (3.17) – (3.20). The source-affected input-voltage control loop gain L^S_{in} can be solved using (3.21). The special parameters $G_{io-\infty}$ and $Y_{o-\infty}$ are as defined in (3.22) and (3.23), respectively.

$$Z^S_{in\text{-}c} = \frac{\hat{u}_{pv}}{\hat{i}_{pv}} = \frac{Z^S_{in\text{-}o}}{1 + L^S_{in}} \tag{3.17}$$

$$T^S_{oi\text{-}c} = \frac{\hat{u}_{pv}}{\hat{u}_{dc}} = \frac{T^S_{oi\text{-}o}}{1 + L^S_{in}} \tag{3.18}$$

$$G^S_{io\text{-}c} = \frac{\hat{i}_{dc}}{\hat{i}_{pv}} = \frac{G^S_{io\text{-}o}}{1 + L^S_{in}} + \frac{L^S_{in}}{1 + L^S_{in}} G_{io-\infty} \tag{3.19}$$

$$Y^S_{o\text{-}c} = \frac{\hat{i}_{dc}}{\hat{u}_{dc}} = \frac{Y^S_{o\text{-}o}}{1 + L^S_{in}} + \frac{L^S_{in}}{1 + L^S_{in}} Y_{o-\infty} \tag{3.20}$$

$$L^S_{in} = G^S_{ci\text{-}o} G_{PWM} G_c H_v \tag{3.21}$$

$$G_{\mathrm{io}-\infty} = G_{\mathrm{io\text{-}o}} - \frac{Z_{\mathrm{in\text{-}o}} G_{\mathrm{co\text{-}o}}}{G_{\mathrm{ci\text{-}o}}} \tag{3.22}$$

$$Y_{\mathrm{o}-\infty} = Y_{\mathrm{o\text{-}o}} + \frac{T_{\mathrm{oi\text{-}o}} G_{\mathrm{co\text{-}o}}}{G_{\mathrm{ci\text{-}o}}} \tag{3.23}$$

The first term of the closed-loop output admittance (3.20) originates from the open-loop output admittance $Y^{\mathrm{S}}_{\mathrm{o\text{-}o}}$ and is divided by the input-voltage control loop gain. Thus, the first term of the output admittance can be considered negligible at low frequencies where the control loop gain has a large magnitude. Moreover, the first part of the second term $L^{\mathrm{S}}_{\mathrm{in}} / \left(1 + L^{\mathrm{S}}_{\mathrm{in}}\right)$ is unity below the crossover frequency of the input-voltage control. Therefore, the closed-loop output admittance is dominated by the ideal output admittance $Y_{\mathrm{o}-\infty}$ below the crossover frequency of the input-voltage control loop. The DC-admittance of the DC-DC converter can be solved symbolically by setting the Laplace-variable s in $Y_{\mathrm{o}-\infty}$ equal to zero yielding (3.24). The output impedance is approximately the ratio of the converter's output voltage and current which is actually the typical property of a constant-power-output converter.

$$Z^{\mathrm{S}}_{\mathrm{o\text{-}c}}\left(s=0\right) = \frac{1}{Y^{\mathrm{S}}_{\mathrm{o\text{-}c}}\left(s=0\right)} = \frac{U_{\mathrm{dc}} + U_{\mathrm{D}} + \left(r_{\mathrm{D}} - r_{\mathrm{sw}}\right) I_{\mathrm{pv}}}{D' I_{\mathrm{pv}}} \approx \frac{U_{\mathrm{dc}}}{D' I_{\mathrm{pv}}} = \frac{U_{\mathrm{dc}}}{I_{\mathrm{dc}}} \tag{3.24}$$

The measured and predicted output impedances of the DC-DC converter at different operating points are shown in Fig. 3.14. The low-frequency magnitude of the impedance is not affected by the dynamic resistance of the PV generator. Therefore, the use of input-voltage control effectively prevents the dynamics of the PV generator from affecting the low-frequency output impedance of the DC-DC converter. The DC-link voltage U_{dc} is regulated at a constant value by the DC-link voltage controller of the inverter. Therefore, the value of the low-frequency output impedance depends mainly on the output current of the DC-DC converter, i.e., the output power of the PV generator.

3.4.2 Effect of the input-voltage-controlled DC-DC converter on DC-link control dynamics

The effect of the input-voltage controlled DC-DC converter on the DC-link control dynamics of the inverter can be analyzed symbolically by using the inverse of the low-frequency output impedance of the DC-DC converter (3.24) as the source admittance Y_{S} in (2.100) – (2.109). The source-affected control-to-output-current transfer function $G^{\mathrm{S\text{-}OL}}_{\mathrm{co\text{-}d}}$ is as given in (3.25) without the parasitic elements, where the superscript ´S-CL' is used to denote that the transfer function is affected by the output impedance of the input-voltage-controlled DC-DC converter. The low-frequency zero of the transfer function is located at the origin. The design constraint related to the RHP-pole has

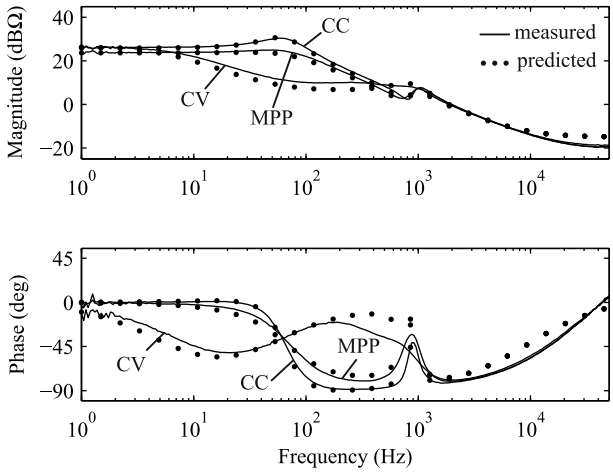

Fig. 3.14: Measured and predicted output impedances of the DC-DC converter under input-voltage control.

disappeared. From the dynamical point-of-view, there is no minimum requirement for the DC-link capacitance when the DC-DC converter operates under input-voltage control. However, the DC-link capacitance should be designed large enough to mitigate the voltage ripple which appears when the grid voltages are unbalanced as discussed, e.g., in (Karanayil et al., 2013) but this is out of the scope of this thesis.

$$G_{\text{co-d}}^{\text{S-CL}} = \frac{\hat{i}_{\text{od}}}{\hat{d}_{\text{d}}} = \frac{U_{\text{dc}}}{L} s^2 \frac{1}{\Delta^{\text{S-CL}}} \tag{3.25}$$

where

$$\Delta^{\text{S-CL}} = s^3 + \frac{D'^2 I_{\text{pv}}}{C_{\text{dc}} U_{\text{pv}}} s^2 + \left[\frac{3\left(D_{\text{d}}^2 + D_{\text{q}}^2\right)}{2 C_{\text{dc}} L} + \omega_{\text{s}}^2 \right] s + \frac{D'^2 I_{\text{pv}}}{C_{\text{dc}} U_{\text{pv}}} \omega_{\text{s}}^2. \tag{3.26}$$

Fig. 3.15 shows the measured and predicted DC-link voltage control loop gains when the DC-DC converter operates under input-voltage control. The shape of the loop gain was essentially the same in all operating points and, therefore, only the measurement in the CC region is shown. The phase margin of the loop gain is positive and the control system is stable.

The stability of the two-stage inverter was verified by changing the reference voltage of the DC-DC converter $u_{\text{pv}}^{\text{ref}}$ from CV region to CC region and back. Time-domain responses of the voltage of the solar array simulator, DC-link voltage and current of

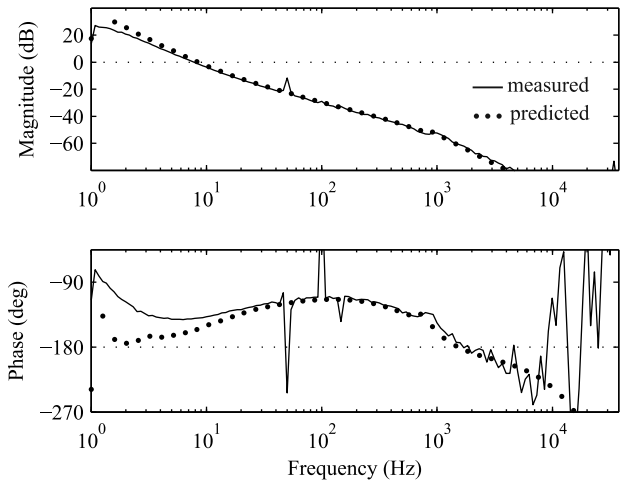

Fig. 3.15: Measured and predicted DC-link voltage control loop gains in the CC region when the DC-DC converter operates under input-voltage control.

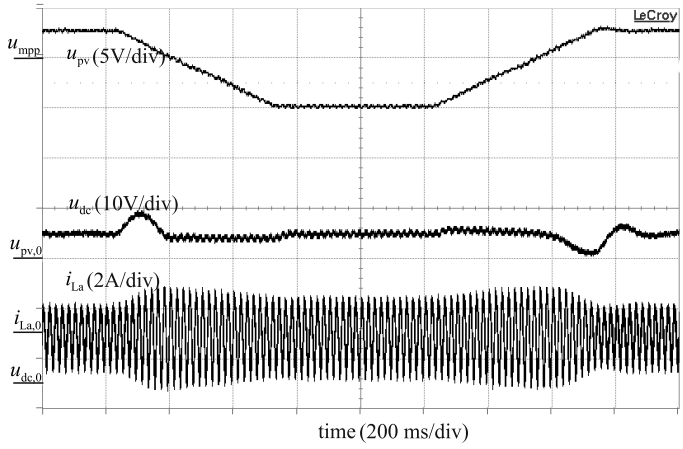

Fig. 3.16: DC-link voltage control remains stable when the input voltage of the DC-DC converter is controlled.

phase A are shown in Fig. 3.16. The component sizing was exactly the same as in the previous case when the DC-DC converter was operated in open-loop control mode. The DC-link voltage remains stable at all operating points. The slight variations in the DC-link voltage originate from the fact that the DC-link voltage control was tuned to be very slow ($\omega_c = 2\pi \cdot 8$ rad/s). Thus, it takes some time for the DC-link voltage controller to reach steady-state when the output power of the solar array simulator changes. However, the grid current does not contain any such low-frequency harmonics as in the previous case when the DC-DC converter was operated in the open-loop control mode. The amplitude of the phase currents changes according to the generated power as expected.

3.5 Conclusions

Two-stage inverters are widely utilized in PV applications due to the benefits that the voltage-boosting characteristics provide. The DC-DC converter is usually operated at open loop or under input-voltage control where the voltage of the PV generator is regulated using a feedback loop. The dynamic resistance of the PV generator together with the control mode of the DC-DC converter determine the shape of the converter's output impedance. The control dynamics of the inverter are affected by the output impedance of the DC-DC converter.

The DC-link control dynamics include a RHP-pole when the DC-DC converter operates at open loop and the PV generator operates in the CC region. Therefore, the DC-link voltage control can become unstable at voltages below the MPP when insufficient DC-link capacitance is used. A design rule is proposed which guarantees the stability of the DC-link voltage control. In addition, it is shown that the RHP-pole is effectively removed when the DC-DC converter is operated under input-voltage control. The input-voltage control prevents the low-frequency dynamics of the PV generator from affecting the output impedance of the DC-DC converter and the control dynamics of the inverter. Thus, using the DC-DC converter under input-voltage control instead of open-loop control improves the robustness of stability of the two-stage inverter.

4 EFFECT OF A PHASE-LOCKED-LOOP ON THE INVERTER DYNAMICS

The effect of a commonly used grid synchronization method, i.e., the phase-locked-loop (PLL), on the dynamics of the PV inverter is studied in this chapter as discussed in (Messo, Jokipii, Mäkinen and Suntio, 2013). A short literature review is presented in the beginning to familiarize the reader to prior research and the problematics related to the topic. The PLL is included in the small-signal model by linearizing the average model of the PLL. The effect of the PLL on the output impedance of the inverter is discussed and verified by simulations and experimental measurements.

4.1 Introduction

The output currents of a three-phase inverter have to be synchronized with the output voltages to inject current into the utility grid. This is achieved commonly by using the PLL (Chung, 2000). The PLL has been claimed to affect the shape of the inverter's output impedance in a way that can cause stability problems. Some researchers have reported the PLL to cause a negative real part in the output impedance of a three-phase inverter (Alawasa et al., 2014; Céspedes and Sun, 2011) and in the impedance of a three-phase active rectifier (Harnefors et al., 2007; Wen et al., 2012).

A negative real part of the impedance is often associated with stability problems. Three-phase PV inverters have been reported to become unstable when the utility grid has large inductance (Liserre et al., 2006) or, at least, to increase harmonic currents (Céspedes and Sun, 2011; Enslin and Heskes, 2004). The reported issues with harmonic instabilities are most likely caused by the interactions between the output impedance of the inverter and the input impedance of the grid (Chen and Sun, 2011; Liserre et al., 2006; Wang et al., 2011).

The impedances of the inverter and the grid have to be measured or predicted using an accurate small-signal model to analyse the possibility for instability. There exists several methods to measure three-phase impedances. In any case, a small-signal excitation in the voltages or currents is required to measure the impedance. The exication signal can be in the form of a wide-bandwidth binary signal (Martin et al., 2013) or the frequency components can be identified one frequency at a time. A separate VSI can be used to

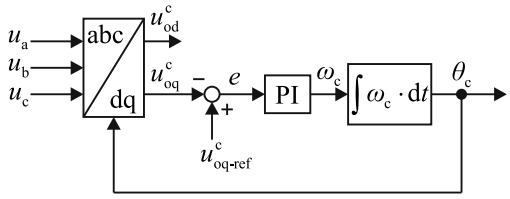

Fig. 4.1: Control diagram of a conventional phase-locked-loop.

generate a small-signal injection in a shunt or series configuration (Shen et al., 2013). Alternatively, a line-current injection can be done using an injection circuit (Huang et al., 2009). The impedances can be measured in the synchronous reference frame as their positive and negative-sequence components (Céspedes and Sun, 2011). Due to the nature of the small-signal model used in this thesis, it is convenient to measure the impedances in the synchronous reference frame.

4.2 Small-signal model of the PV inverter with phase-locked-loop

The control diagram of a conventional PLL is depicted in Fig. 4.1. The PI-type controller acts on the error signal e which is calculated from the sensed q-component of the grid voltage u^c_{oq} and the reference voltage $u^c_{oq\text{-}ref}$. The reference voltage is set equal to zero and is, therefore, usually not shown in the control diagram. The output of the controller is the estimated frequency of the grid ω_c which is converted into the estimated phase angle θ_c using an integrator. The sensed phase angle is fed back to the dq-transformation block which is part of the PLL. The error signal is zero at steady state, i.e., the estimated q-component of the grid voltage is zero. Therefore, the estimated phase angle is the same as the phase angle of the grid voltages and the control system reference frame is aligned with the grid reference frame.

Fig. 4.2 shows two phase-shifted coordinate systems in the synchronous reference frame. The one denoted with superscript 'g' is tied to the space-vector of the grid and the one denoted with superscript 'c' is tied to the space-vector inside the control system which is estimated using the PLL. In Fig. 4.2, θ_c is the angle of the control system reference frame, θ_g is the angle of the grid reference frame and θ_Δ is the angle difference between the systems. The grid voltages are usually selected as the reference and, therefore, the angle θ_g is zero. A linear mapping between the two reference frames is needed in order to include the PLL in the small-signal model of the inverter.

A space-vector $\boldsymbol{x}$ can be presented in any of the reference frames using the d and q components because all the frames rotate at the same angular frequency at steady-state. Moreover, the space-vector can be given in the control system reference frame as in (4.1)

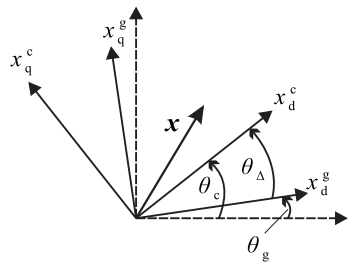

Fig. 4.2: Synchronous reference frames tied to the control system of the inverter 'c' and to the ideal grid voltages 'g'.

by noting that the angle of the grid reference frame θ_g is zero.

$$\boldsymbol{x}^c = x_d^c + jx_q^c = \boldsymbol{x}^g \, e^{-j\theta_\Delta} = \left(x_d^g + jx_q^g\right) \, e^{-j\theta_\Delta} \tag{4.1}$$

The exponential term can be given as a sum of cosine and sinus of the angle difference by using Euler's formula. Therefore, the d and q-components in the control system reference frame can be given as a function of the d and q-components in the grid reference frame according to (4.2) and (4.3), respectively.

$$x_d^c = x_d^g \cos\theta_\Delta + x_q^g \sin\theta_\Delta \tag{4.2}$$

$$x_q^c = x_q^g \cos\theta_\Delta - x_d^g \sin\theta_\Delta \tag{4.3}$$

The angle difference θ_Δ between the two coordinate systems is zero at steady-state. Therefore, the cosine of the angle is approximately unity and the sinus equals the value of the angle difference in radians. The angle of the control system reference frame θ_c is the same as the angle difference between the coordinate systems θ_Δ which yields (4.4) and (4.5).

$$x_d^c \approx x_d^g + x_q^g \theta_c \tag{4.4}$$

$$x_q^c \approx x_q^g - x_d^g \theta_c \tag{4.5}$$

The relation in (4.4) and (4.5) can be linearized by developing the first-order partial derivatives in respect to each variable and can be written as in (4.6) and (4.7) where Θ_c

is the angle difference at steady-state and X_d and X_q are the steady-state values of the d and q-components.

$$\hat{x}_\mathrm{d}^\mathrm{c} = \hat{x}_\mathrm{d}^\mathrm{g} + \Theta_\mathrm{c}\hat{x}_\mathrm{q}^\mathrm{g} + X_\mathrm{q}\hat{\theta}_\mathrm{c} \tag{4.6}$$

$$\hat{x}_\mathrm{q}^\mathrm{c} = \hat{x}_\mathrm{q}^\mathrm{g} - \Theta_\mathrm{c}\hat{x}_\mathrm{d}^\mathrm{g} - X_\mathrm{d}\hat{\theta}_\mathrm{c} \tag{4.7}$$

Output currents, voltages and duty ratios in the control system reference frame can be given as a function of the variables in the grid reference frame as in (4.8)–(4.13).

$$\hat{u}_\mathrm{od}^\mathrm{c} = \hat{u}_\mathrm{od}^\mathrm{g} + \Theta_\mathrm{c}\hat{u}_\mathrm{oq}^\mathrm{g} + U_\mathrm{oq}\hat{\theta_\mathrm{c}} \tag{4.8}$$

$$\hat{i}_\mathrm{od}^\mathrm{c} = \hat{i}_\mathrm{od}^\mathrm{g} + \Theta_\mathrm{c}\hat{i}_\mathrm{oq}^\mathrm{g} + I_\mathrm{oq}\hat{\theta_\mathrm{c}} \tag{4.9}$$

$$\hat{d}_\mathrm{d}^\mathrm{c} = \hat{d}_\mathrm{d}^\mathrm{g} + \Theta_\mathrm{c}\hat{d}_\mathrm{q}^\mathrm{g} + D_\mathrm{q}\hat{\theta_\mathrm{c}} \tag{4.10}$$

$$\hat{u}_\mathrm{oq}^\mathrm{c} = \hat{u}_\mathrm{oq}^\mathrm{g} - \Theta_\mathrm{c}\hat{u}_\mathrm{od}^\mathrm{g} - U_\mathrm{od}\hat{\theta_\mathrm{c}} \tag{4.11}$$

$$\hat{i}_\mathrm{oq}^\mathrm{c} = \hat{i}_\mathrm{oq}^\mathrm{g} - \Theta_\mathrm{c}\hat{i}_\mathrm{od}^\mathrm{g} - I_\mathrm{od}\hat{\theta_\mathrm{c}} \tag{4.12}$$

$$\hat{d}_\mathrm{q}^\mathrm{c} = \hat{d}_\mathrm{q}^\mathrm{g} - \Theta_\mathrm{c}\hat{d}_\mathrm{d}^\mathrm{g} - D_\mathrm{d}\hat{\theta_\mathrm{c}} \tag{4.13}$$

The relation can be written as in (4.14)–(4.19) since the steady-state angle between the coordinate systems Θ_c, q-component of the grid voltage U_oq and the q-component of the output current I_oq are equal to zero. In addition, the q-component of the duty ratio D_q is usually very small and is neglected in the analysis. The steady-state values of U_od, I_od and D_d can be solved by using (2.47) – (2.51). The small-signal angle $\hat{\theta}_\mathrm{c}$ remains as the only unknown variable.

$$\hat{u}_\mathrm{d}^\mathrm{c} = \hat{u}_\mathrm{d}^\mathrm{g} \tag{4.14}$$

$$\hat{i}_\mathrm{od}^\mathrm{c} = \hat{i}_\mathrm{od}^\mathrm{g} \tag{4.15}$$

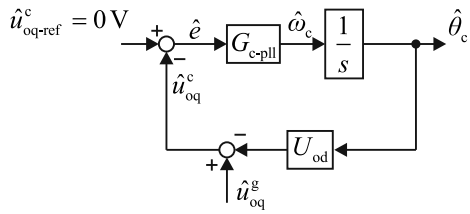

Fig. 4.3: Linearized control block diagram of the PLL.

$$\hat{d}^{c}_{d} = \hat{d}^{g}_{d} \tag{4.16}$$

$$\hat{u}^{c}_{oq} = \hat{u}^{g}_{oq} - U_{od}\hat{\theta}_c \tag{4.17}$$

$$\hat{i}^{c}_{oq} = \hat{i}^{g}_{oq} - I_{od}\hat{\theta}_c \tag{4.18}$$

$$\hat{d}^{c}_{q} = \hat{d}^{g}_{q} - D_{d}\hat{\theta}_c \tag{4.19}$$

The linearized control block diagram of the PLL is depicted in Fig. 4.3 which is derived by utilizing (4.14)–(4.19) and by transforming the controller and the integrator of Fig. 4.1 into the frequency-domain. The small-signal angle $\hat{\theta}_c$ can be solved from the control block diagram by taking into account that the reference is zero and is as given in (4.20). The control loop gain of the PLL L_{PLL} is as given in (4.21).

$$\hat{\theta}_c = \frac{1}{U_{od}} \frac{L_{PLL}}{1 + L_{PLL}} \hat{u}^{g}_{oq} \tag{4.20}$$

$$L_{PLL} = -\frac{G_{c\text{-}pll} U_{od}}{s} \tag{4.21}$$

Finally, the relation between the small-signal variables in the two coordinate systems can be presented as given in (4.22)–(4.27). The relations are required to finalize the linearized small-signal model.

$$\hat{u}^{c}_{d} = \hat{u}^{g}_{d} \tag{4.22}$$

$$\hat{i}_{\mathrm{od}}^{\mathrm{c}} = \hat{i}_{\mathrm{od}}^{\mathrm{g}} \tag{4.23}$$

$$\hat{d}_{\mathrm{d}}^{\mathrm{c}} = \hat{d}_{\mathrm{d}}^{\mathrm{g}} \tag{4.24}$$

$$\hat{u}_{\mathrm{oq}}^{\mathrm{c}} = \left(1 - \frac{L_{\mathrm{PLL}}}{1 + L_{\mathrm{PLL}}}\right) \hat{u}_{\mathrm{oq}}^{\mathrm{g}} \tag{4.25}$$

$$\hat{i}_{\mathrm{oq}}^{\mathrm{c}} = \hat{i}_{\mathrm{oq}}^{\mathrm{g}} - \frac{I_{\mathrm{od}}}{U_{\mathrm{od}}} \frac{L_{\mathrm{PLL}}}{1 + L_{\mathrm{PLL}}} \hat{u}_{\mathrm{oq}}^{\mathrm{g}} \tag{4.26}$$

$$\hat{d}_{\mathrm{q}}^{\mathrm{c}} = \hat{d}_{\mathrm{q}}^{\mathrm{g}} - \frac{D_{\mathrm{d}}}{U_{\mathrm{od}}} \frac{L_{\mathrm{PLL}}}{1 + L_{\mathrm{PLL}}} \hat{u}_{\mathrm{oq}}^{\mathrm{g}} \tag{4.27}$$

4.3 Output impedance of the PV inverter with phase-locked-loop

The PLL does not affect the dynamics related to the d-components as long as the steady-state value of D_{q} remains small and, thus, the d-component of the output impedance can be given as in (4.28) and as derived in Section 2.3.3.

$$Z_{\text{o-d-c}} = \frac{1}{Y_{\text{o-d-c}}} = \frac{\hat{u}_{\mathrm{od}}}{\hat{i}_{\mathrm{od}}} = \left(\frac{Y_{\text{o-d}}}{(1 + L_{\mathrm{dc}})\,(1 + L_{\text{out-d}})} + \frac{L_{\mathrm{dc}}}{(1 + L_{\mathrm{dc}})} Y_{\mathrm{o-d-}\infty} \right)^{-1} \tag{4.28}$$

The q-components in (4.24)–(4.27) are affected by the PLL. The PLL can be included in the control block diagram which describes the output dynamics of q-components (Fig. 2.10b) by taking into account the relation given by (4.24)–(4.27). The control block diagram which includes the PLL is shown in Fig. 4.4. The sensing gain H_{q} and the modulator gain G_{PWM} are assumed to be unity because they can be manipulated inside the DSP. The q-component of the output admittance can be solved by setting the small-signal input current $\hat{i}_{\mathrm{pv}}$ equal to zero and solving the transfer function from the q-component of the output voltage $\hat{u}_{\mathrm{oq}}^{\mathrm{g}}$ to the q-component of the output current $\hat{i}_{\mathrm{oq}}^{\mathrm{g}}$ in the grid reference frame. The q-component of the output impedance is as given in (4.29) where the current control loop gain $L_{\text{out-q}}$ is as defined in (4.30).

$$\begin{aligned} Z_{\text{o-q-c}} = \frac{1}{Y_{\text{o-q-c}}} = \Bigg(& \frac{Y_{\text{o-q}}}{1 + L_{\text{out-q}}} - \frac{L_{\mathrm{PLL}}}{(1 + L_{\mathrm{PLL}})} \frac{L_{\text{out-q}}}{(1 + L_{\text{out-q}})} \frac{I_{\mathrm{od}}}{U_{\mathrm{od}}} \\ & - \frac{L_{\mathrm{PLL}}}{(1 + L_{\mathrm{PLL}})} \frac{G_{\text{co-q}}}{(1 + L_{\text{out-q}})} \frac{D_{\mathrm{d}}}{U_{\mathrm{od}}} \Bigg)^{-1} \end{aligned} \tag{4.29}$$

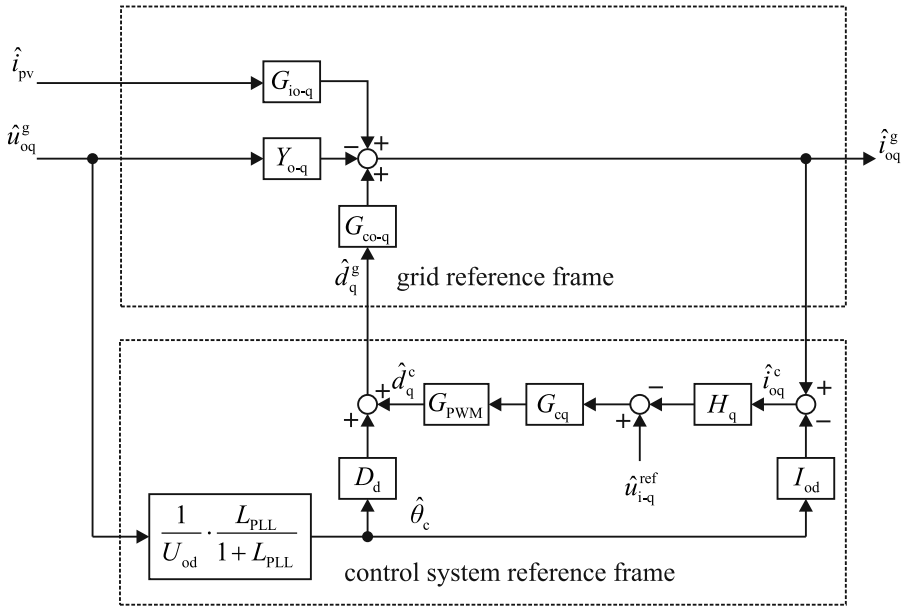

Fig. 4.4: Q-channel control block diagram with the phase-locked-loop.

$$L_{\text{out-q}} = G_{\text{co-q}} G_{\text{PWM}} G_{\text{cq}} H_{\text{q}} \tag{4.30}$$

The q-component of the output admittance has two terms that have a negative sign which are affected by the loop gain of the phase-locked-loop L_{PLL} and the loop gain of the output current control $L_{\text{out-q}}$. After careful analysis, it can be deduced that the low-frequency value of the output impedance is approximately the ratio $-U_{\text{od}}/I_{\text{od}}$ because both control loops have high gain and, therefore, the terms $L_{\text{PLL}}/(1+L_{\text{PLL}})$ and $L_{\text{out-q}}/(1+L_{\text{out-q}})$ are close to unity. The third term in (4.29) is considerably smaller than the second term since the d-component of the duty ratio is small compared to the output current. Moreover, the third term is divided with the current control loop gain which is designed to have high gain at low frequencies. Thus, the q-component of the output impedance resembles a negative resistor at frequencies below the crossover frequency of the PLL as given in (4.31).

$$Z^{\text{low-freq}}_{\text{o-q-c}} = -\frac{U_{\text{od}}}{I_{\text{od}}} \tag{4.31}$$

A switching model of a single-stage three-phase PV inverter was simulated in MATLAB Simulink using the SimPowerSystems Toolbox. The simulation model was used as

Table 4.1: Parameters of the simulation model.

U_{MPP}	699.3 V	$U_{\mathrm{grid\text{-}rms}}$	230 V	$L_{(\mathrm{a,b,c})}$	2.46 mH
I_{MPP}	14.66 A	ω_{grid}	$2\pi{\cdot}50$ Hz	$r_{\mathrm{L(a,b,c)}}$	25.8 mΩ
r_{pv}	$U_{\mathrm{MPP}}/I_{\mathrm{MPP}}$	C_{dc}	2.6 mF	r_{sw}	20 mΩ
P_{MPP}	10.25 kW	$r_{\mathrm{C\text{-}dc}}$	10 mΩ	f_{s}	10 kHz

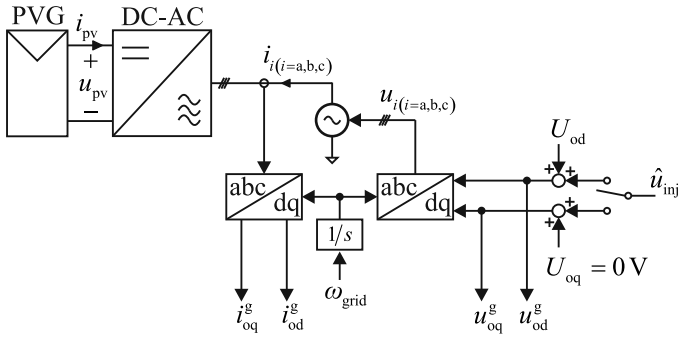

Fig. 4.5: Principle of extracting the d and q-components of the output impedance from the switching model.

the first step in verification of the model. The source was modeled by a voltage-controlled current source which was tuned to replicate the IU-curve and the dynamic resistance of a real PV generator. The parameters of the switching model are summarized in Table 4.1. The inverter was operated at the MPP by setting the reference of the DC-link voltage control $u_{\mathrm{dc\text{-}ref}}$ in Fig. 2.8 equal to the MPP voltage U_{MPP}.

The d and q-components of the output impedance were extracted from the switching model by using frequency response analysis. The principle of extracting the frequency responses is illustrated in Fig. 4.5. A wide-bandwidth excitation signal $\hat{u}_{\mathrm{inj}}$ was added in the d or q-component of the grid voltage and the output voltages and output currents of the inverter were measured in the grid reference frame. The d and q-components of the output impedance can be extracted from the ratios $u^{\mathrm{g}}_{\mathrm{od}}/i^{\mathrm{g}}_{\mathrm{od}}$ and $u^{\mathrm{g}}_{\mathrm{oq}}/i^{\mathrm{g}}_{\mathrm{oq}}$ by using the methods presented, e.g., in (Roinila et al., 2010).

The predicted and simulated d-components of the output impedance are shown in Fig. 4.6. The phase of the impedance stays between -90 and 90 degrees meaning that the output impedance resembles a passive circuit and, therefore, is unlikely to cause instability.

Fig. 4.7 shows the predicted and simulated q-components of the output impedance.

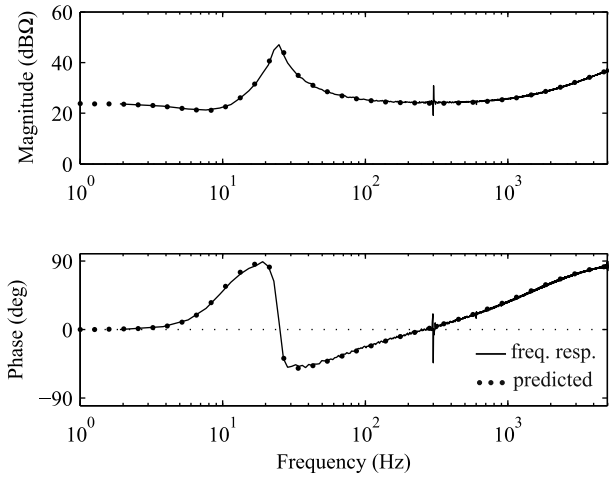

Fig. 4.6: Simulated and predicted d-component of the output impedance with PLL.

Table 4.2: Parameters of the SAS

U_{MPP}	30 V	U_{OC}	38.3 V
I_{MPP}	1 A	I_{SC}	1.1 A

The phase of the impedance is less than -90 degrees below the crossover frequency of the PLL which was set to 100 Hz. The magnitude of impedance is the ratio of the output current and output voltage d-components $U_{\mathrm{od}}/I_{\mathrm{od}}$ at low frequencies and the phase curve starts from -180 degrees. Therefore, it is evident that the q-component of the output impedance behaves as a negative resistor at low frequencies.

Output impedances were extracted from the experimental three-phase inverter to further validate the small-signal model. The inverter was fed from the SAS and the three-phase voltage source with parallel-connected load resistors were used as a load. The parameters of the SAS are summarized in Table 4.2. The inverter was set to operate at the MPP.

The principle of the impedance measurement setup is illustrated in Fig. 4.8. A DSP was used to generate the phase angle and the three-phase grid voltage references which were fed to the voltage source using three PWM outputs. The small-signal perturbation $\hat{u}_{\mathrm{inj}}$ was done either in the d or q-component of the grid voltage by feeding it through an analog-to-digital converter and by adding it to the reference voltages of the voltage source. The output currents and voltages of the inverter were measured using a separate measurement circuit and transformed into the synchronous reference frame using the

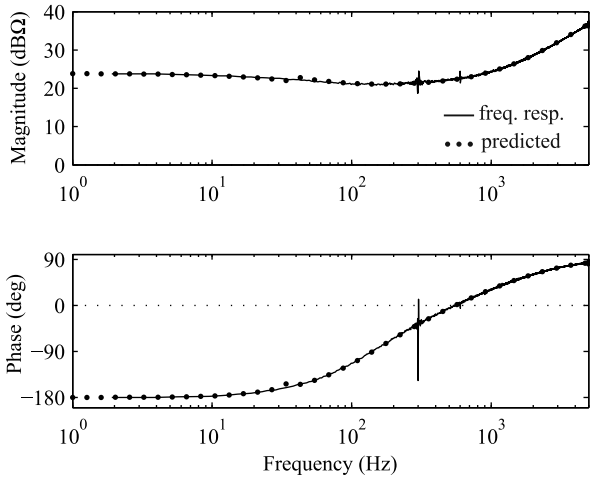

Fig. 4.7: Simulated and predicted q-component of the output impedance with PLL.

same phase angle θ_g which was used to generate the phase voltages. Therefore, there are no accuracy errors in the measurement caused by an additional PLL as reported in (Shen, Z. et al., 2013). The measured d or q-components of output voltages and currents of the inverter were fed to the frequency response analyzer using two PWM outputs of the DSP.

The d-component of the output impedance was measured by feeding the d-component of the output current i^g_{od} and voltage u^g_{od} to the FRA. Fig. 4.9 shows the measured and predicted impedances at the MPP. The shape of the impedance resembles the impedance extracted from the switching model in Fig. 4.6. The phase curve stays between -90 and 90 degrees and the impedance behaves as a passive circuit.

The q-component of the output impedance of the prototype inverter is shown in Fig. 4.10 which was obtained by feeding the q-components of the output current i^g_{oq} and voltage u^g_{oq} to the FRA. The crossover frequency of the PLL was set to 100 Hz. The phase of the impedance is less than -90 degrees below the crossover frequency of the PLL starting from -180 degrees and, thus, the real part of the impedance q-component is negative at low frequencies.

4.4 Impedance-based interactions

A three-phase PV inverter which is connected to the utility grid using a three-phase CL-filter is depicted in Fig. 4.11. The parameters of the inverter were the same as given in Table 4.1 except for the CL-filter (Table 4.3). The CL-filter is added to suppress the

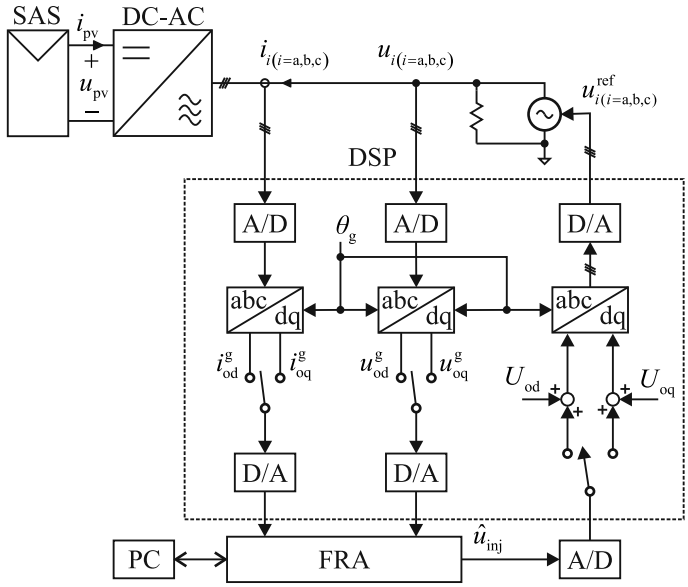

Fig. 4.8: Principle of the output impedance measurement setup.

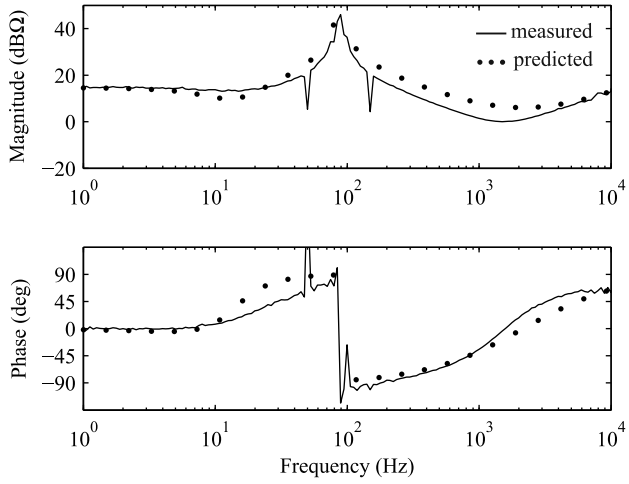

Fig. 4.9: D-component of the output impedance measured from the experimental prototype.

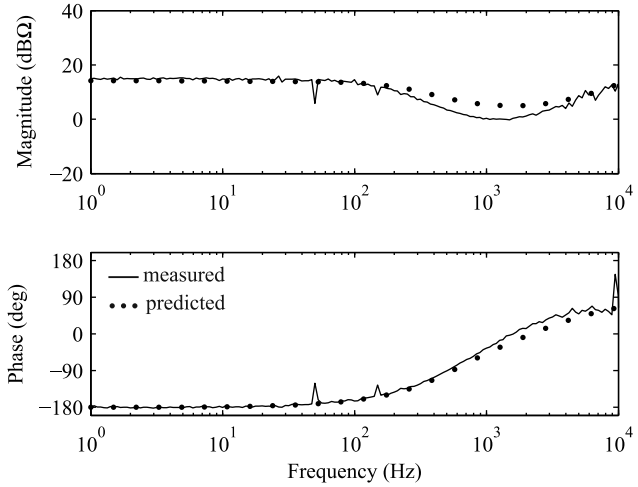

Fig. 4.10: Q-component of the output impedance measured from the experimental prototype.

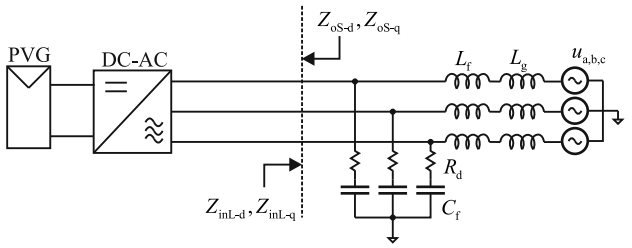

Fig. 4.11: Three-phase PV inverter connected to the grid using CL-type output filter.

switching ripple in the output currents of the inverter to a suitable level. The grid is assumed to be mainly inductive with an inductance L_g. The capacitance of the filter C_f was selected equal to 0.04 p.u. of the capacitance base value. The capacitance value is generally chosen below 0.05 p.u. because the power factor of the converter decreases with increasing capacitance. This is due to the fact that the converter synchronizes its phase currents with the capacitor voltages and, thus, there is a phase difference between the currents and grid voltages. The resonant frequency of the filter was set at 1470 Hz. Passive damping was used to avoid resonant-peaking of the CL-filter. The value of the damping resistance was selected as one third of the capacitor impedance at the resonant frequency as discussed in (Liserre et al., 2005).

The stability at the interface between the PV inverter and the output filter was evaluated in two cases. The interface is illustrated in Fig. 4.11 with a dashed line. In the first case, the grid was assumed ideal with no inductance, i.e., $L_g = 0$. In the

Table 4.3: Parameters of the CL-filter

C_f	25 μF	r_Lf	26 mΩ
L_f	475 μH	R_d	1.46 Ω

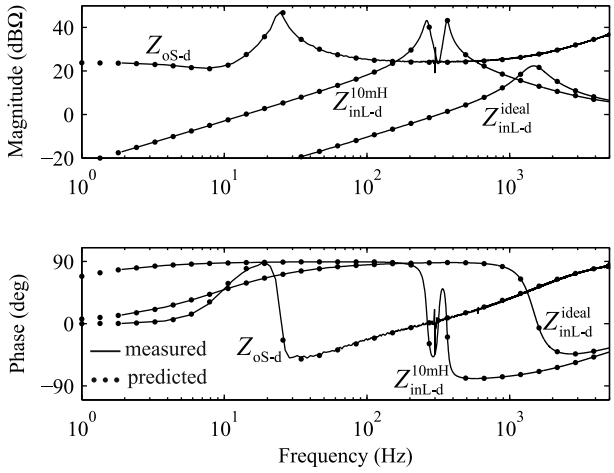

Fig. 4.12: D-components of the impedances extracted from the switching model.

second case, the grid impedance was assumed to be an inductance of 10 mH. The d and q-components of the filter input impedance were extracted from the switching model by feeding the filter from a balanced three-phase current source and making a small-signal excitation to the d or q-component of the input current.

The extracted and predicted d-components of the output impedance $Z_{\mathrm{oS\text{-}d}}$ of the inverter and the input impedance $Z_{\mathrm{inL\text{-}d}}$ of the filter are shown in Fig. 4.12. The superscript 'ideal' denotes that the grid inductance is zero and '10 mH' denotes that the grid inductance is increased to 10 mH. The grid inductance was included in the small-signal model by increasing the inductance value of the filter L_f. The grid inductance shifts the resonant frequency of the CL-filter to a lower frequency causing the impedances to overlap as can be seen in Fig. 4.12.

The overlapping of the impedance d-components suggests that the system might be unstable. However, the stability should be validated by applying the Nyquist stability criterion to the ratios of the impedance d and q-components separately as explained in Chapter 2. The ratio of the impedance d-components on the complex plane $Z_{\mathrm{inL\text{-}d}}/Z_{\mathrm{oS\text{-}d}}$ is shown in Fig. 4.13 in both cases. The large-grid-inductance case is presented by a dotted line and the ideal case by a solid line. The contour never encircles the critical point

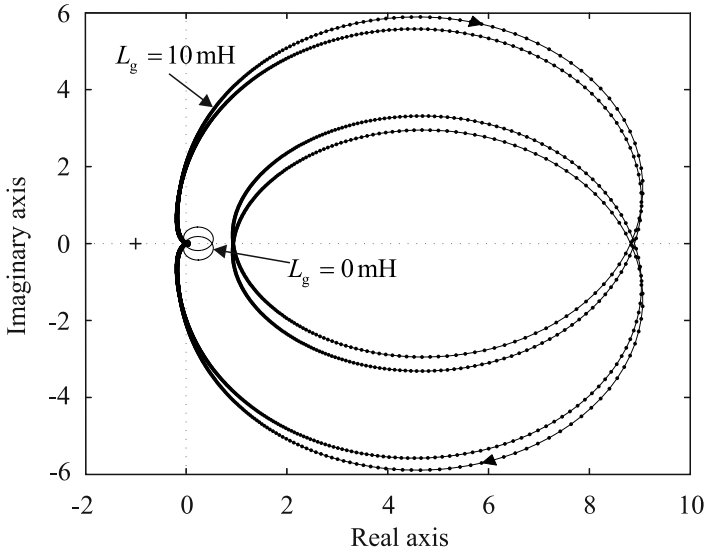

Fig. 4.13: Ratio of the impedance d-components in the complex plane.

(-1,0) and, thus, the system is stable in terms of the d-components of the impedances.

The extracted and predicted q-components of the output impedance of the inverter $Z_{\text{oS-q}}$ and the input impedance of the filter $Z_{\text{inL-q}}$ are shown in Fig. 4.14. Similarly as before, the resonance of the filter shifts to a lower frequency due to large grid inductance which causes the impedances to overlap. The difference in the phase of the impedances $Z_{\text{oS-q}}$ and $Z_{\text{inL-q}}^{10\text{mH}}$ at 130 Hz is more than 180 degrees which implies that the system is unstable in terms of the impedance q-components. However, the stability should be verified by plotting the ratio of the impedance q-components $Z_{\text{inL-q}}/Z_{\text{oS-q}}$ on the complex plane and by applying the Nyquist stability criterion.

The ratio of the impedance q-components is depicted on the complex plane in Fig. 4.15. According to the Nyquist stability criterion, the system remains stable in terms of the impedance q-components when the grid is ideal. However, the contour encircles the critical point (-1,0) in clockwise direction in the large-inductance case indicating that the system has a pole on the right-half of the complex plane and is unstable.

Instability caused by interaction between the impedance q-components was verified by using the switching model implemented with SimPowerSystems. The PV inverter was connected to a three-phase grid using the CL-filter as depicted in Fig. 4.11. The inductance of the grid was zero at first but was increased to 10 mH at 0.1 s causing the interface between the filter and the inverter to become unstable due to interaction between the impedance q-components. Simulated phase voltage and phase current are shown in Fig. 4.16 where the instability of the grid current is clearly visible after 0.1 s.

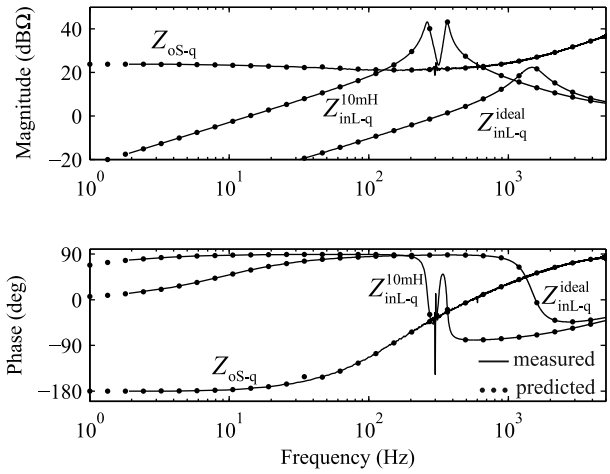

Fig. 4.14: Q-components of the impedances extracted from the switching model.

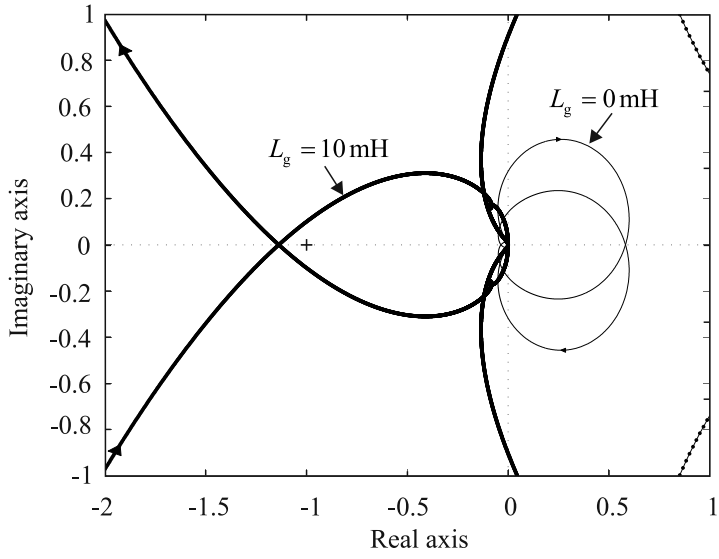

Fig. 4.15: Ratio of the impedance q-components in the complex plane.

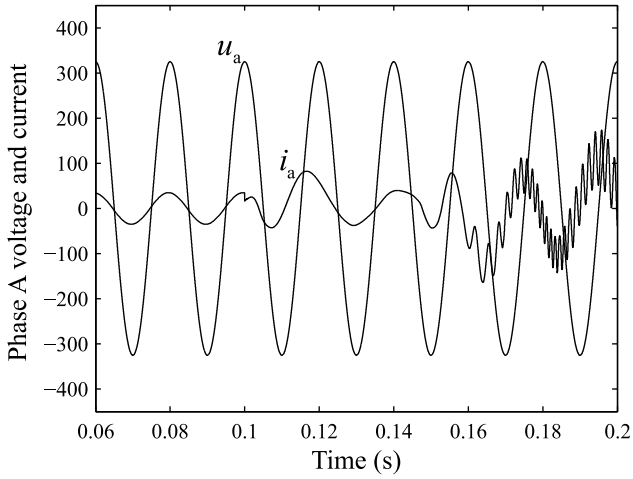

Fig. 4.16: Interface between the inverter and the output filter becomes unstable when the grid inductance is increased.

Table 4.4: Parameters of the experimental CL-filter

C_f	160 μF	r_Lf	110 mΩ
L_f	552 μH	R_d	210 mΩ

The experimental prototype converter operating at reduced voltages was used to further validate the results. A three-phase CL-filter with the parameters given in Table 4.4 was connected between the prototype and the parallel connection of the load resistors and three-phase voltage source. The parameters of the filter were selected in such a manner that the inverter would become unstable when the crossover frequency of the PLL is increased to 300 Hz. The d and q-components of the filter input impedance were measured by using the measurement setup depicted in Fig. 4.17. The small-signal perturbation was made by the FRA in the duty ratios D_d or D_q of the inverter which was operating at open loop. The input voltages and currents of the CL-filter were measured using a separate measurement card to extract the impedances.

The output impedance of the inverter was measured in two cases. At first, the crossover frequency of the PLL was set to 100 Hz, and in the second case, the crossover frequency was increased to approximately 300 Hz. The d-component of the inverter output impedance was essentially the same in both cases since the PLL does not affect the d-components. Therefore, only the measurement with the PLL crossover frequency of 300 Hz is shown. The measured d-components of the inverter output impedance and the

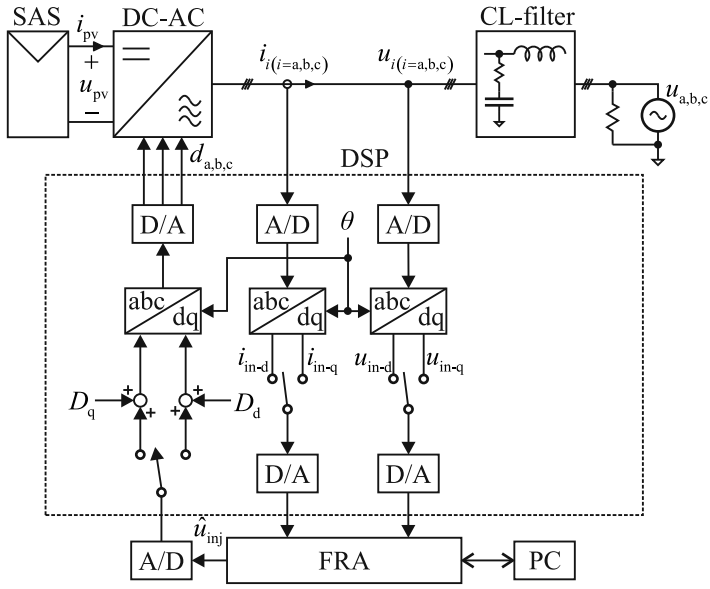

Fig. 4.17: Setup for measuring the input impedance of the three-phase CL-filter.

filter input impedance are shown in Fig. 4.18. The filter is a passive circuit, i.e., its phase curve lies between -90 and 90 degrees. Moreover, the phase curve of the inverter output impedance exceeds -90 degrees only slightly due to noise in the measurements. Therefore, the d-component of the inverter output impedance resembles a passive component.

The measured ratio of the impedance d-components $Z_{\text{inL-d}}/Z_{\text{oS-d}}$ is shown in the complex plane in Fig. 4.19. The contour does not encircle the critical point (-1,0) which means that the system is stable in terms of the d-components. However, the q-components should also be examined to complete the stability analysis. The measured and predicted q-components of the impedances are shown in Fig. 4.20. The superscripts in the lower part of the figure are used to denote the crossover frequency of the PLL, whether 100 or 300 Hz. The magnitudes of the inverter output impedances stay approximately the same in both cases. However, the phase of the impedance in the second case ($Z_{\text{oS-q}}^{300\text{Hz}}$) is closer to 180 degrees at higher frequencies due to the increased crossover frequency of the PLL. Moreover, in the second case the impedances overlap at 342 Hz with a phase difference more than 180 degrees which indicates a potential instability.

The ratio $Z_{\text{inL-q}}/Z_{\text{oS-q}}$ of the measured impedance q-components in the complex plane is depicted in Fig. 4.21 when the PLL crossover frequency is set to 300 Hz. The contour encircles the critical point (-1,0) in clockwise direction indicating that the interface is unstable.

The instability caused by the impedance-based interaction of the impedance q-components

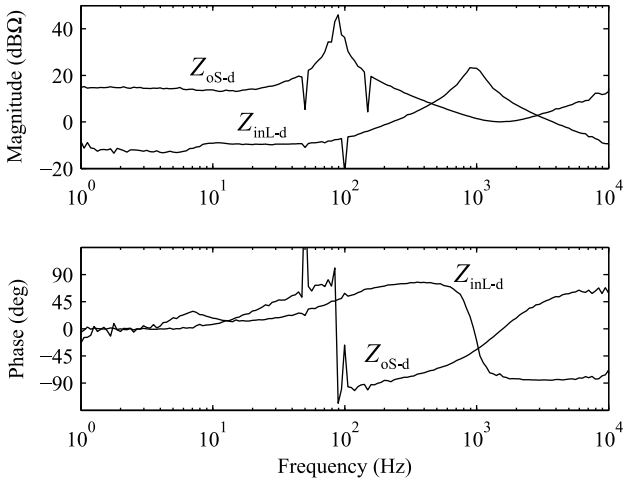

Fig. 4.18: Measured d-components of the output impedance of the inverter and the input impedance of the filter.

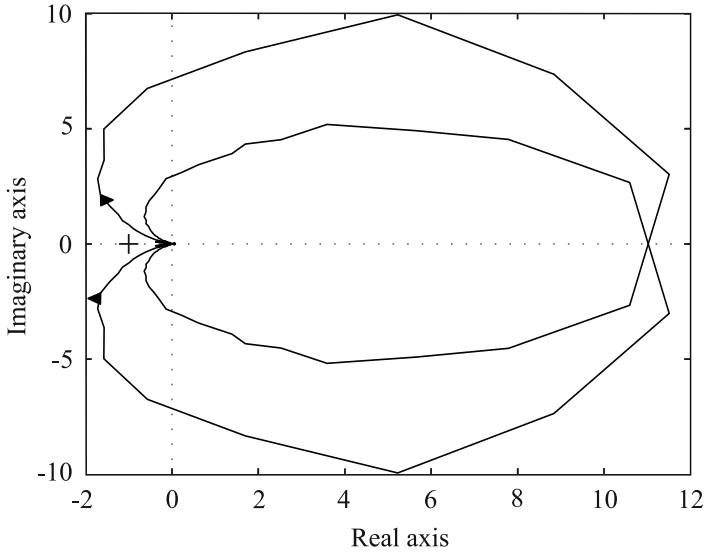

Fig. 4.19: Ratio of the impedance d-components in the complex plane.

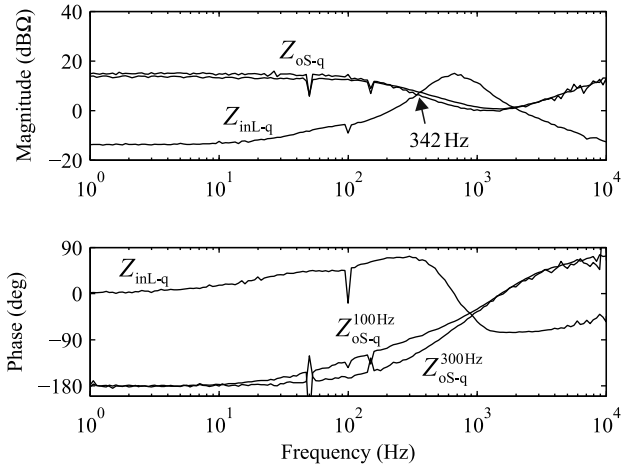

Fig. 4.20: Measured and predicted impedance q-components.

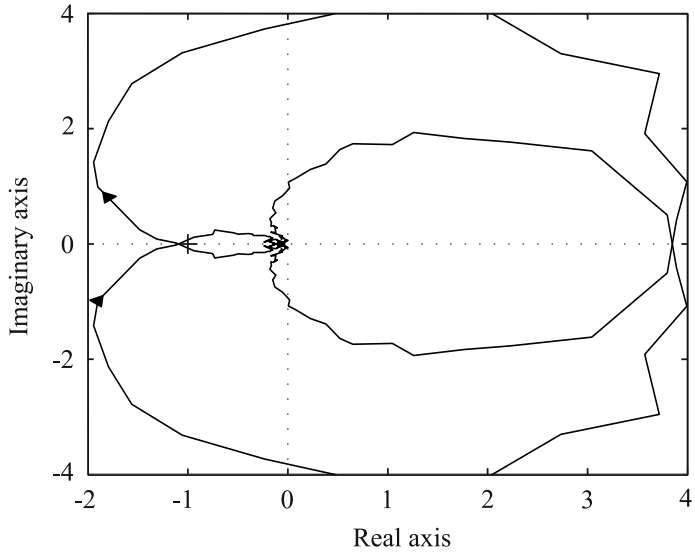

Fig. 4.21: Ratio of the impedance q-components in the complex plane.

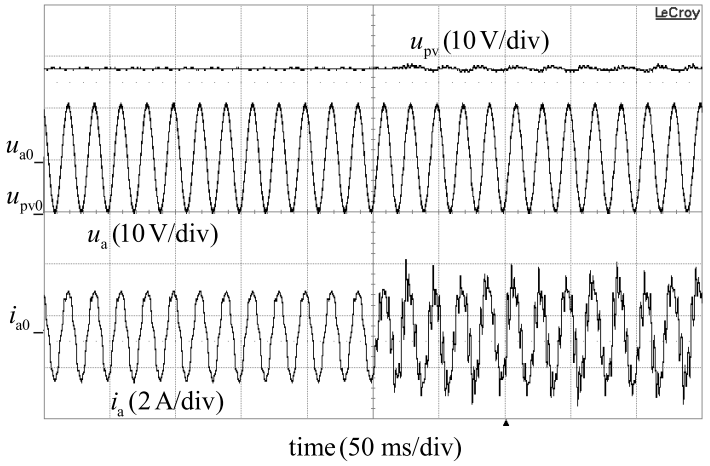

Fig. 4.22: Inverter output current becomes unstable due to impedance-based interaction.

was verified by using the prototype converter. The crossover frequency of the PLL was increased from 100 Hz to 300 Hz which, according to the previous analysis, would cause the interface between the inverter and the CL-filter to become unstable.

Fig. 4.22 shows the time-domain response of the DC-link voltage, phase voltage and output current of one phase of the inverter when the PLL crossover frequency is increased to 300 Hz. The instability caused by the impedance-based interactions of the q-components does not make the DC-link voltage unstable and the fundamental current component stays the same. However, the quality of the output current is decreased significantly since the output current contains large harmonic components.

The spectrum of the output current was recorded using a Waverunner 104MXi oscilloscope manufactured by LeCroy and is as shown in Fig. 4.23 for the unstable case. In addition to the small ripple components caused by measurement circuits, the spectrum has two large spikes at 288 and 388 Hz. The magnitudes of these components are approximately 16 and 26 percent of the fundamental component. The spikes are separated exactly by 100 Hz and their center frequency is at 338 Hz which is approximately the same as the frequency at which the impedance q-components overlap in Fig. 4.20 (342 Hz) when the PLL crossover frequency was set to 300 Hz.

4.5 Conclusions

Three-phase PV inverters have been reported to suffer from instability when connected to a polluted or weak grid which has high inductance. The cause of the instability has been traced back to interactions between the output impedance of the inverter and the grid impedance. The bandwidth of the PLL's control loop gain has been identified as

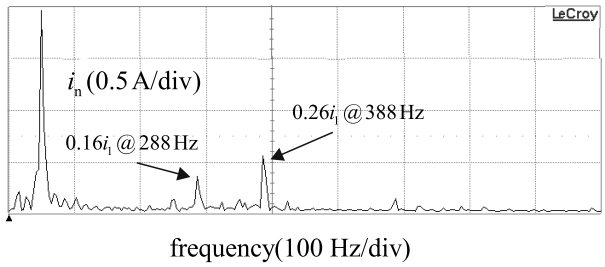

Fig. 4.23: Spectrum of the output current in the unstable case.

one of the most prominent factors related to the stability issues.

This chapter presented a consistent method to include the PLL in the small-signal model of a three-phase VSI-based PV inverter. The investigations show that the d-component of the inverter's output impedance is not affected by the PLL. However, the q-component of the impedance resembles a negative resistor at frequencies below the crossover frequency of the PLL's control loop gain. The model is verified by measuring the d and q-components of the output impedance from a switching model and from a prototype inverter operating at reduced voltages.

The inverter is vulnerable to impedance-based interactions and instability due to the negative-resistance nature of the q-component of the output impedance. The situation is most severe when a wide-bandwidth PLL is used in a grid that has large inductance. The instability can be avoided by, e.g., limiting the bandwidth of the PLL. However, the output impedance of the inverter and the input impedance of the grid has to be known in order to make trustworthy stability analysis. The small-signal model developed in this thesis can be used to study the effect of the PLL on the shape of the output impedance of the inverter and to make reliable stability analysis.

5 EFFECT OF GRID-VOLTAGE FEEDFORWARD ON INVERTER DYNAMICS

The control system of a three-phase PV inverter often includes a feedforward measurement from the grid voltages. An inverter employing a feedforward has been shown to exhibit better transient performance and to inject less harmonic currents in the grid. In this chapter, the feedforward is included in the small-signal model of a three-phase inverter and its effect on the shape of the output impedance is examined. The feedforward is shown to increase the magnitude of the output impedance if the gain in the feedforward path is chosen correctly which explains the decreased harmonic currents. The small-signal model is verified by extracting the output impedance of the PV inverter from a switching model. The simulation results have been previously reported in (Messo, Jokipii and Suntio, 2014).

5.1 Introduction

Grid-voltage feedforward is often utilized in grid-connected three and single-phase inverters (Timbus et al., 2009; Xue et al., 2012). The feedforward can be implemented in the stationary reference frame (Li et al., 2011) or in the synchronous reference frame (Park et al., 2008). The purpose of the feedforward is to mitigate the harmonic currents generated by nonideal grid voltages and to improve the performance of the inverter during transients as discussed in (Huang et al., 2008). In addition, the grid-voltage feedforward has been shown to mitigate the effect of unbalanced grid voltages (Li et al., 2011). The feedforward was successfully implemented to a single-phase fuel-cell inverter in (Park et al., 2008) where it allowed the inverter to be started with zero power command without reverse power flow phenomenon which could lead to failure of the fuel-cell. The aim of the feedforward was to increase the output impedance of the inverter to make it insensitive to variations in grid voltage. Park et al. (2008) reported lower harmonic currents of a VSI with an LCL-filter when the feedforward in the synchronous reference frame was used. The improved transient performance and lower harmonic currents suggest that the grid-voltage feedforward increases the magnitude of the inverter's output impedance at the harmonic frequencies.

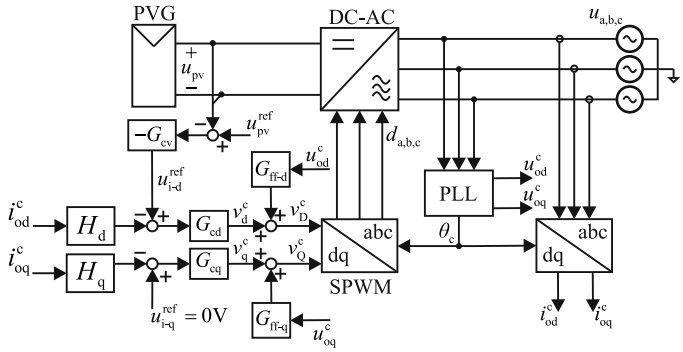

Fig. 5.1: Cascaded control scheme with grid-voltage feedforward.

5.2 Small-signal model of the PV inverter with grid-voltage feedforward

The control system of the PV inverter with the grid-voltage feedforward implemented in the synchronous reference frame is depicted in Fig. 5.1. The d and q-components of the grid voltages $u_{\mathrm{od}}^{\mathrm{c}}$ and $u_{\mathrm{oq}}^{\mathrm{c}}$ are sensed and added to the outputs of the current controllers, i.e., to the control voltages $v_{\mathrm{d}}^{\mathrm{c}}$ and $v_{\mathrm{q}}^{\mathrm{c}}$ in the control system reference frame. The d and q-components of the output voltages are multiplied by the feedforward gains $G_{\text{ff-d}}$ and $G_{\text{ff-q}}$, respectively. The feedforward gains usually include a sensing gain and a low-pass filter.

The small-signal voltages which are fed to the SPWM can be given as in (5.1) and in (5.2) where the feedforward gains $G_{\text{ff-d}}$ and $G_{\text{ff-q}}$ are assumed to be linear.

$$\hat{v}_{\mathrm{D}}^{\mathrm{c}} = \hat{v}_{\mathrm{d}}^{\mathrm{c}} + G_{\text{ff-d}}\hat{u}_{\mathrm{od}}^{\mathrm{c}} \tag{5.1}$$

$$\hat{v}_{\mathrm{Q}}^{\mathrm{c}} = \hat{v}_{\mathrm{q}}^{\mathrm{c}} + G_{\text{ff-q}}\hat{u}_{\mathrm{oq}}^{\mathrm{c}} \tag{5.2}$$

The effect of the grid-voltage feedforward on the dynamics of the inverter can be solved by utilizing the same methods as in Chapter 2. The control block diagrams which describe the inverter's input dynamics and the output dynamics related to the d-component are depicted in Fig. 5.2 when the output current control and the feedforward loops are closed. The input dynamics are assumed to be dominated by the dynamics related of the d-components. Therefore, the crosscoupling transfer functions between the d and q-components can be neglected, i.e., the transfer functions $G_{\text{ci-q}}$, $T_{\text{oi-q}}$, $Y_{\text{o-qd}}$ and

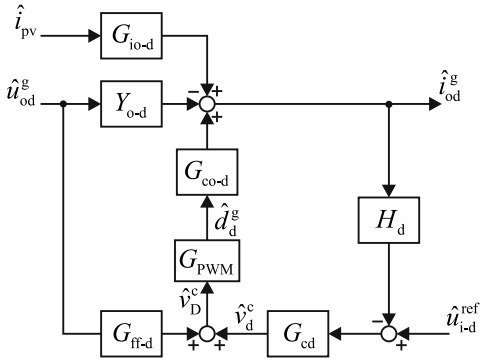

(a) Output dynamics related to d-components.

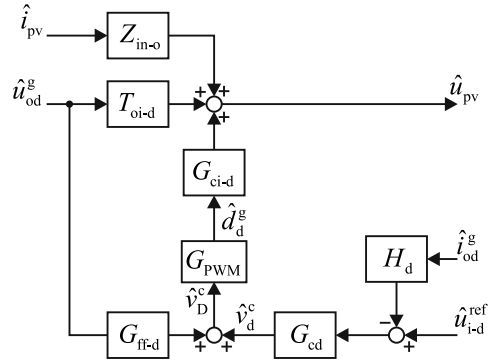

(b) Input dynamics.

Fig. 5.2: Control block diagrams of the inverter with grid-voltage feedforward and output current control.

$G_{\text{co-qd}}$ can be neglected. Moreover, it is assumed that the PLL does not affect the sensed d-components of the output currents and voltages and that the q-component of the duty ratio D_{q} is small, i.e., $\hat{d}^{\text{g}}_{\text{d}} = \hat{d}^{\text{c}}_{\text{d}}$.

The transfer functions of the inverter can be solved from the control block diagrams in Fig. 5.2 and are as given in (5.3) – (5.8). The superscript 'cc-ff' is used to denote that the transfer functions include the effect of the output current control and the grid-voltage feedforward. The current control loop gain $L_{\text{out-d}}$ and the special parameters $Z_{\text{in}-\text{d}-\infty}$ and $T_{\text{oi}-\text{d}-\infty}$ are as defined in (5.9) – (5.11). The special parameters and the current control loop gain are not affected by the feedforward.

$$G^{\text{cc-ff}}_{\text{io-d}} = \frac{\hat{i}^{\text{g}}_{\text{od}}}{\hat{i}_{\text{dc}}} = \frac{G_{\text{io-d}}}{1 + L_{\text{out-d}}} \tag{5.3}$$

$$Y^{\text{cc-ff}}_{\text{o-d}} = -\frac{\hat{i}^{\text{g}}_{\text{od}}}{\hat{u}^{\text{g}}_{\text{od}}} = \frac{Y_{\text{o-d}} - G_{\text{co-d}} G_{\text{PWM}} G_{\text{ff-d}}}{1 + L_{\text{out-d}}} \tag{5.4}$$

$$G^{\text{cc-ff}}_{\text{co-d}} = \frac{\hat{i}^{\text{g}}_{\text{od}}}{\hat{u}^{\text{ref}}_{\text{i-d}}} = \frac{1}{H_{\text{d}}} \frac{L_{\text{out-d}}}{(1 + L_{\text{out-d}})} \tag{5.5}$$

$$Z^{\text{cc-ff}}_{\text{in}} = \frac{\hat{u}_{\text{dc}}}{i_{\text{dc}}} = \frac{Z_{\text{in}}}{1 + L_{\text{out-d}}} + \frac{L_{\text{out-d}}}{1 + L_{\text{out-d}}} Z_{\text{in}-\text{d}-\infty} \tag{5.6}$$

$$T^{\text{cc-ff}}_{\text{oi-d}} = \frac{\hat{u}_{\text{dc}}}{u^{\text{g}}_{\text{od}}} = \frac{T_{\text{oi-d}} + G_{\text{ci-d}} G_{\text{PWM}} G_{\text{ff-d}}}{1 + L_{\text{out-d}}} + \frac{L_{\text{out-d}}}{1 + L_{\text{out-d}}} T_{\text{oi}-\text{d}-\infty} \tag{5.7}$$

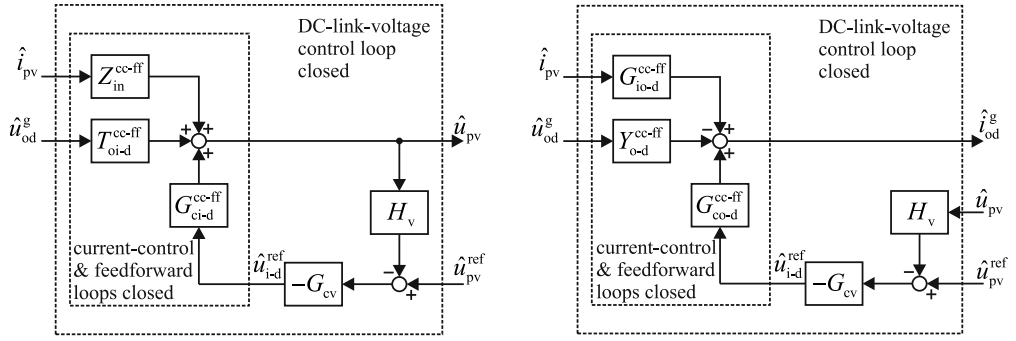

(a) Input dynamics. **(b)** Output dynamics related to d-components.

Fig. 5.3: Control block diagrams when the DC-link voltage control loop is closed.

$$G_{\text{ci-d}}^{\text{cc-ff}} = \frac{\hat{u}_{\text{dc}}}{u_{\text{i-d}}^{\text{ref}}} = \frac{1}{H_{\text{d}}} \frac{G_{\text{ci-d}}}{G_{\text{co-d}}} \frac{L_{\text{out-d}}}{(1 + L_{\text{out-d}})} \tag{5.8}$$

$$L_{\text{out-d}} = G_{\text{co-d}} G_{\text{PWM}} G_{\text{cd}} H_{\text{d}} \tag{5.9}$$

$$Z_{\text{in}-\text{d}-\infty} = Z_{\text{in}} - \frac{G_{\text{ci-d}} G_{\text{io-d}}}{G_{\text{co-d}}} \tag{5.10}$$

$$T_{\text{oi}-\text{d}-\infty} = T_{\text{oi-d}} + \frac{G_{\text{ci-d}} Y_{\text{o-d}}}{G_{\text{co-d}}} \tag{5.11}$$

The DC-link voltage control can be included in the transfer functions, as in Chapter 2, by considering the output-current-controlled inverter as an open-loop system with $\hat{u}_{\text{i-d}}^{\text{ref}}$ as the control input. The control block diagrams describing inverter's input dynamics and the output dynamics related to the d-component are depicted in Fig. 5.3. The transfer functions of the inverter with DC-link voltage control and the grid-voltage feedforward are as given in (5.12) – (5.17) where the superscript 'ff' is used to denote that the effect of the feedforward is included in the dynamics. The feedforward affects the output-to-input transfer function $T_{\text{oi-d-c}}^{\text{ff}}$ and the d-component of the output admittance $Y_{\text{o-d-c}}^{\text{ff}}$.

$$Z_{\text{in-c}}^{\text{ff}} = \frac{\hat{u}_{\text{pv}}}{\hat{i}_{\text{pv}}} = \frac{Z_{\text{in}}}{(1 + L_{\text{dc}})(1 + L_{\text{out-d}})} + \frac{1}{(1 + L_{\text{dc}})} \frac{L_{\text{out-d}}}{(1 + L_{\text{out-d}})} Z_{\text{in}-\infty} \tag{5.12}$$

$$T_{\text{oi-d-c}}^{\text{ff}} = \frac{\hat{u}_{\text{pv}}}{\hat{u}_{\text{od}}^{\text{g}}} = \frac{T_{\text{oi-d}} + G_{\text{ci-d}} G_{\text{PWM}} G_{\text{ff-d}}}{(1 + L_{\text{dc}})(1 + L_{\text{out-d}})} + \frac{1}{(1 + L_{\text{dc}})} \frac{L_{\text{out-d}}}{(1 + L_{\text{out-d}})} T_{\text{oi}-\text{d}-\infty} \tag{5.13}$$

$$G_{\mathrm{ri}}^{\mathrm{ff}} = \frac{\hat{u}_{\mathrm{pv}}}{\hat{u}_{\mathrm{pv}}^{\mathrm{ref}}} = \frac{1}{H_{\mathrm{v}}} \frac{L_{\mathrm{dc}}}{(1 + L_{\mathrm{dc}})} \tag{5.14}$$

$$G_{\mathrm{io\text{-}d\text{-}c}}^{\mathrm{ff}} = \frac{\hat{i}_{\mathrm{od}}^{\mathrm{g}}}{\hat{i}_{\mathrm{pv}}} = \frac{G_{\mathrm{io\text{-}d}}}{(1 + L_{\mathrm{dc}})(1 + L_{\mathrm{out\text{-}d}})} + \frac{L_{\mathrm{dc}}}{(1 + L_{\mathrm{dc}})} G_{\mathrm{io-d-}\infty} \tag{5.15}$$

$$Y_{\mathrm{o\text{-}d\text{-}c}}^{\mathrm{ff}} = -\frac{\hat{i}_{\mathrm{od}}^{\mathrm{g}}}{\hat{o}_{\mathrm{od}}^{\mathrm{g}}} = \frac{Y_{\mathrm{o\text{-}d}} - G_{\mathrm{co\text{-}d}} G_{\mathrm{PWM}} G_{\mathrm{ff\text{-}d}}}{(1 + L_{\mathrm{dc}})(1 + L_{\mathrm{out\text{-}d}})} + \frac{L_{\mathrm{dc}}}{(1 + L_{\mathrm{dc}})} Y_{\mathrm{o-d-}\infty} \tag{5.16}$$

$$G_{\mathrm{ro\text{-}d}}^{\mathrm{ff}} = \frac{\hat{i}_{\mathrm{od}}^{\mathrm{g}}}{\hat{u}_{\mathrm{pv}}^{\mathrm{ref}}} = \frac{1}{H_{\mathrm{v}}} \frac{G_{\mathrm{co\text{-}d}}}{G_{\mathrm{ci\text{-}d}}} \frac{L_{\mathrm{dc}}}{(1 + L_{\mathrm{dc}})} \tag{5.17}$$

The DC-link voltage control loop gain L_{dc} and the special parameters $G_{\mathrm{io-d-}\infty}$ and $Y_{\mathrm{o-d-}\infty}$ are not affected by the feedforward and can be given as in (5.18) – (5.20).

$$L_{\mathrm{dc}} = -G_{\mathrm{ci\text{-}d}}^{\mathrm{cc\text{-}ff}} G_{\mathrm{cv}} H_{\mathrm{v}} = -\frac{H_{\mathrm{v}}}{H_{\mathrm{d}}} \frac{G_{\mathrm{ci\text{-}d}}}{G_{\mathrm{co\text{-}d}}} \frac{L_{\mathrm{out\text{-}d}}}{(1 + L_{\mathrm{out\text{-}d}})} G_{\mathrm{cv}} \tag{5.18}$$

$$G_{\mathrm{io-d-}\infty} = G_{\mathrm{io\text{-}d}} - \frac{G_{\mathrm{co\text{-}d}}}{G_{\mathrm{ci\text{-}d}}} Z_{\mathrm{in}} \tag{5.19}$$

$$Y_{\mathrm{o-d-}\infty} = Y_{\mathrm{o\text{-}d}} + \frac{G_{\mathrm{co\text{-}d}}}{G_{\mathrm{ci\text{-}d}}} T_{\mathrm{oi\text{-}d}} \tag{5.20}$$

The effect of the feedforward on the output dynamics related to the q-component can be solved from the control block diagram depicted in Fig. 5.4 where the crosscoupling transfer functions between the d and q-components $G_{\mathrm{co\text{-}dq}}$ and $Y_{\mathrm{o\text{-}dq}}$ are neglected. The control block diagram can be constructed by modifying the one presented earlier in Fig. 4.4 where the output current control of the q-component and the PLL were considered. The small-signal voltages that are fed to the pulse-width modulator (5.2) are added in the control block diagram to take the grid-voltage feedforward into account. The control voltage $\hat{v}_{\mathrm{Q}}^{\mathrm{c}}$ can be given as a function of the q-component of the output voltage in the grid reference frame by using the relation derived in (4.24)–(4.27) and is as given in (5.21).

$$\hat{v}_{\mathrm{Q}}^{\mathrm{c}} = \hat{v}_{\mathrm{q}}^{\mathrm{c}} + G_{\mathrm{ff\text{-}q}} \left(1 - \frac{L_{\mathrm{PLL}}}{1 + L_{\mathrm{PLL}}}\right) \hat{u}_{\mathrm{oq}}^{\mathrm{g}} \tag{5.21}$$

The output admittance of the inverter can be solved from the control block diagram of Fig. 5.4 by the setting the small-signal input current $\hat{i}_{\mathrm{pv}}$ and the reference $\hat{u}_{\mathrm{i\text{-}q}}^{\mathrm{ref}}$ equal to zero and by solving the transfer function between the q-components of the output voltage $\hat{u}_{\mathrm{oq}}^{\mathrm{g}}$ and the output current $\hat{i}_{\mathrm{oq}}^{\mathrm{g}}$. The closed-loop output admittance of the PV inverter with PLL and grid-voltage feedforward is as given in (5.22). The current control

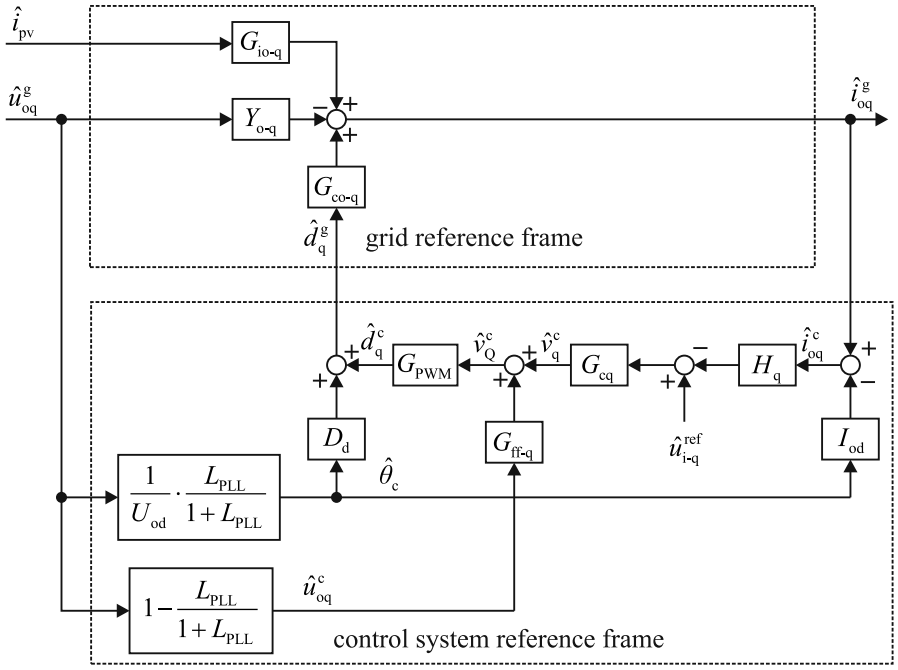

Fig. 5.4: Output dynamics related to q-components with the grid-voltage feedforward and PLL.

loop gain of the q-component $L_{\text{out-q}}$ and and the PLL loop gain are not affected by the feedforward and can be given as in (5.23) and in (5.24).

$$Y_{\text{o-q-c}}^{\text{ff}} = -\frac{\hat{i}_{\text{oq}}^{\text{g}}}{\hat{u}_{\text{oq}}^{\text{g}}} = \frac{1}{1+L_{\text{out-q}}}\left[Y_{\text{o-q}} - G_{\text{co-q}}G_{\text{PWM}}G_{\text{ff-q}}\left(1-\frac{L_{\text{PLL}}}{1+L_{\text{PLL}}}\right)\right] - \frac{L_{\text{out-q}}}{1+L_{\text{out-q}}}\frac{L_{\text{PLL}}}{1+L_{\text{PLL}}}\frac{I_{\text{od}}}{U_{\text{od}}} - \frac{G_{\text{co-q}}}{1+L_{\text{out-q}}}\frac{L_{\text{PLL}}}{1+L_{\text{PLL}}}\frac{D_{\text{d}}}{U_{\text{od}}} \tag{5.22}$$

$$L_{\text{out-q}} = G_{\text{co-q}}G_{\text{PWM}}G_{\text{cq}}H_{\text{q}} \tag{5.23}$$

$$L_{\text{PLL}} = -\frac{G_{\text{c-pll}}U_{\text{od}}}{s} \tag{5.24}$$

The transfer function from the input current to the q-component of the output current can be solved by setting the small-signal terms $\hat{u}_{\text{oq}}^{\text{g}}$ and $\hat{u}_{\text{i-q}}^{\text{ref}}$ equal to zero and by solving the transfer function from $\hat{i}_{\text{pv}}$ to $\hat{i}_{\text{oq}}^{\text{g}}$. The input-to-output-current transfer function of the inverter with grid-voltage feedforward is as given in (5.25). Moreover, the transfer function from the reference of the q-component $\hat{u}_{\text{i-q}}^{\text{ref}}$ to the output current $\hat{i}_{\text{oq}}^{\text{g}}$ can be solved in a similar manner yielding (5.26).

$$G_{\text{io-q-c}}^{\text{ff}} = \frac{\hat{i}_{\text{oq}}^{\text{g}}}{\hat{i}_{\text{pv}}} = \frac{G_{\text{io-q}}}{1+L_{\text{out-q}}} \tag{5.25}$$

$$G_{\text{ro-q}}^{\text{ff}} = \frac{\hat{i}_{\text{oq}}^{\text{g}}}{\hat{u}_{\text{i-q}}^{\text{ref}}} = \frac{1}{H_{\text{q}}}\frac{L_{\text{out-q}}}{(1+L_{\text{out-q}})} \tag{5.26}$$

It can be noticed based on the small-signal model that the grid-voltage feedforward affects only on the output-to-input transfer function $T_{\text{oi-d-c}}$ and the d and q-components of the output admittance $Y_{\text{o-d-c}}$ and $Y_{\text{o-q-c}}$. The effect of the feedforward on the output admittances will be analysed more in detail in the next subsection. The output-to-input transfer function $T_{\text{oi-d-c}}$ describes how disturbances in the d-component of the output voltage affect the DC-link voltage. The effect of the feedforward on $T_{\text{oi-d-c}}$ is not treated in this thesis but is suggested as a future research topic.

5.3 Output impedance of the PV inverter with grid-voltage feedforward

The d-component of the output impedance (5.16) is a sum of two terms. The second term originates from the use of DC-link voltage control and is not affected by the feedforward. However, the first term can be made equal to zero if the feedforward gain $G_{\text{ff-d}}$ is selected as in (5.27). In other words, a perfectly tuned feedforward cancels out the first admittance term in (5.16).

$$G_{\text{ff-d}}^{\text{ideal}} = \frac{Y_{\text{o-d}}}{G_{\text{co-d}} G_{\text{PWM}}} \tag{5.27}$$

The q-component of the output impedance was given in (5.22). The two negative terms on the second row originate from the use of PLL and are not affected by the feedforward. The admittance term on the first row of (5.22) can be made equal to zero when the feedforward gain $G_{\text{ff-q}}$ is selected as in (5.28). However, the feedforward does not affect the admittance at frequencies below the crossover frequency of the PLL, i.e., at frequencies where the term $(1 - L_{\text{PLL}}/(1 + L_{\text{PLL}}))$ is close to zero.

$$G_{\text{ff-q}}^{\text{ideal}} = \frac{Y_{\text{o-q}}}{G_{\text{co-q}} G_{\text{PWM}}} \tag{5.28}$$

After analysing the ideal feedforward gains in (5.27) and (5.28), it was found out that both gains can be approximated as in (5.29) which is actually a value that is often used in the literature (Park et al., 2008).

$$G_{\text{ff-d}}^{\text{ideal}} \approx G_{\text{ff-d}}^{\text{ideal}} \approx \frac{1}{U_{\text{dc}}} \tag{5.29}$$

The d and q-components of the output impedance were extracted from the switching model of a three-phase PV inverter. The switching model was the same that was used in Chapter 4 having the same parameters as given in Table 4.1.

Fig. 5.5 shows the d-component of the output impedance in three cases; without feedforward and with two different feedforward gains. The DC-gain in the feedforward path was selected as the inverse of the DC-link voltage according to (5.29). Moreover, in the one denoted with the superscript 'ff-LP', the feedforward gain $G_{\text{ff-d}}$ includes a low-pass filter with a cut-off frequency at half the switching frequency (5 kHz). The grid-voltage feedforward increases the magnitude of the output impedance in both cases. However, the effect of the feedforward is reduced at high frequencies when the low-pass

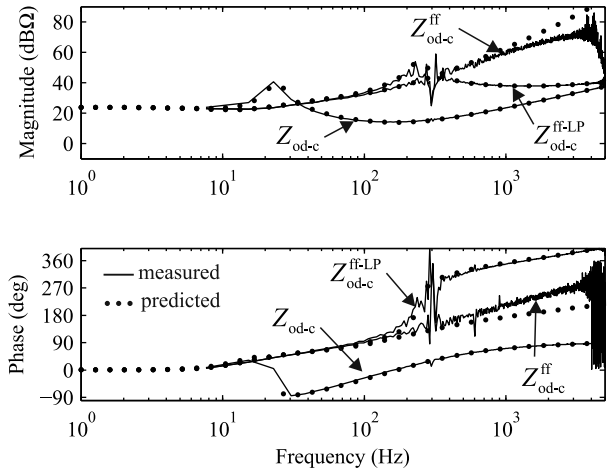

Fig. 5.5: D-component of the output impedance with and without grid-voltage feedforward.

filter is used. The low-pass filter starts deteriorating the effect of the feedforward at already one decade before the cut-off frequency as is expected because the phase of the feedforward gain does not correspond to the ideal feedforward gain in (5.27).

The q-component of the output impedance is shown in Fig. 5.6 with and without grid-voltage feedforward. The same deteoriating effect of the low-pass filter can be seen at high frequencies.

5.4 The effect of grid-voltage feedforward on the impedance-based interactions

The grid-voltage feedforward increases the magnitude of both the d and q-components of the inverter's output impedance. Therefore, the harmonic currents generated by the inverter are reduced as reported, e.g., in (Li et al., 2011; Park et al., 2013). Moreover, an inverter with large output impedance is not so easily affected by impedance-based interactions as will be demonstrated using the switching model.

The inverter was connected to a three-phase voltage source using the same CL-filter as in Chapter 4 with the parameters as given in Table 4.3. The grid inductance was increased from zero to 9 mH in order to cause impedance-based interactions between the input impedance of the filter and the output impedance of the inverter.

Fig. 5.7 shows the ratio of the impedance d-components on the complex plane when the grid inductance is increased to 9 mH. The stability of the inverter was examined in two cases. In the first case, the feedforward was not used and, in the second case, the

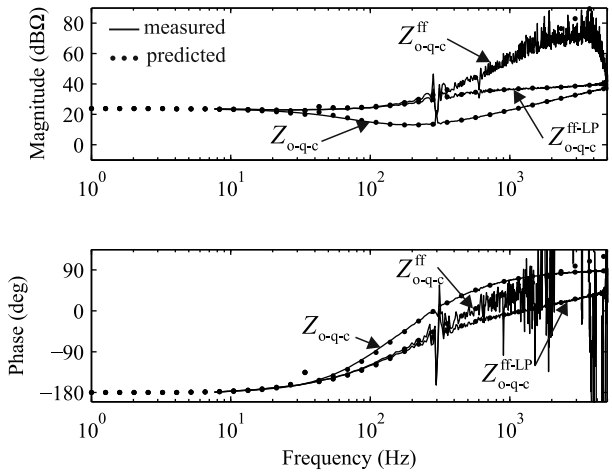

Fig. 5.6: Q-component of the output impedance with and without grid-voltage feedforward.

feedforward with the low-pass filter at half the switching frequency was used. The two cases are denoted in the figure by using the superscripts 'no-ff' and 'ff-LP', correspondingly. The contour does not encircle the critical point (-1,0) and, thus, the inverter is stable in terms of the d-components regardless of the feedforward.

Fig. 5.8 shows the ratio of the impedance q-components in the complex plane. The contour encircles the critical point (-1,0) when the feedforward is not used which means that the inverter is unstable. However, the inverter is stable when the grid-voltage feedforward is used because the contour does not encircle the critical point.

The simulated grid voltages and currents are shown in Fig. 5.9 when the feedforward is suddenly deactivated. The grid current becomes unstable at 0.1s as was predicted based on the small-signal model.

5.5 Conclusions

Three-phase PV inverters often utilize a feedforward measurement from the grid voltages. The feedforward is implemented by adding the sensed d and q-components of the grid voltages to the outputs of the corresponding current controllers. This chapter proposes a method to include the feedforward in the small-signal model of the PV inverter. The analysis shows that the magnitudes of d and q-components of the inverter's output impedance can be increased by tuning the feedforward gain properly. The small-signal model suggests that the ideal feedforward gain is equal to the inverse of DC-link voltage which is also a generally used rule-of-thumb in the literature. However, a low-pass

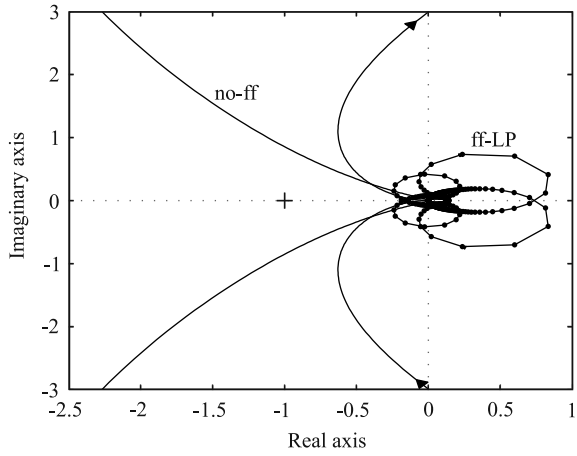

Fig. 5.7: Ratio of the impedance d-components in the complex plane with and without grid-voltage feedforward.

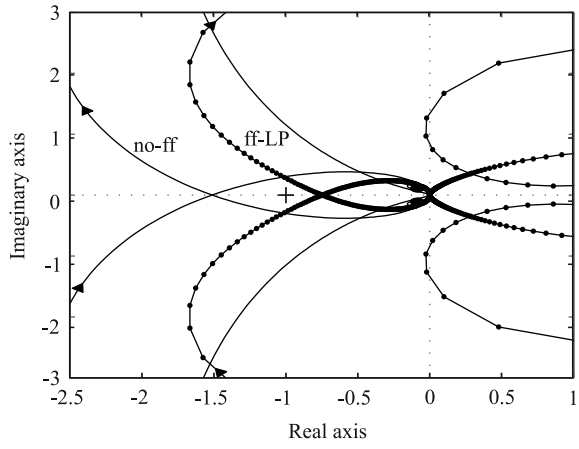

Fig. 5.8: Ratio of the impedance q-components in the complex plane with and without grid-voltage feedforward.

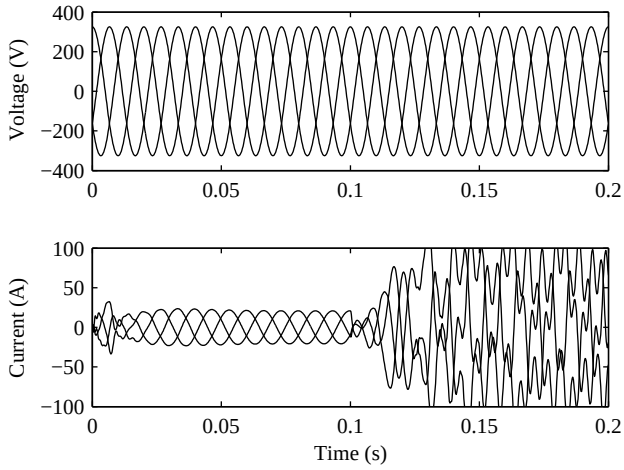

Fig. 5.9: Grid current becomes unstable when grid-voltage feedforward is deactivated.

filter in the grid voltage sensors deteriorates the effect of the feedforward already one decade before the cut-off frequency of the low-pass filter. In any case, the grid-voltage feedforward makes the inverter more resistant to impedance-based interactions due to the increased output impedance.

6 CONCLUSIONS

The amount of grid-connected photovoltaic power systems has increased rapidly over the past decade. The electricity generated by a photovoltaic generator is DC and has to be transformed into three-phase AC to in order to inject power into the grid. The transformation from DC into AC can be done using a three-phase PV inverter. The three-phase inverters have been reported to decrease power quality and to suffer from instability and unintended disconnection from the utility grid in certain conditions.

The conditions for instability can be predicted in the frequency-domain. However, the frequency-domain analysis requires an accurate small-signal model of the inverter. In this thesis the existing small-signal model has been further developed by adding the effect of an upstream DC-DC converter, PLL and grid-voltage feedforward. The model can be used to design the inverter in such a way that the instabilities may be avoided.

6.1 Final conclusions

The effect of a voltage-boosting DC-DC converter on the dynamics of the inverter is analyzed. It is found out that the DC-link control dynamics of the inverter include a right-half-plane pole, just as in the case of a single-stage inverter, which has to be taken into account in the control design. The RHP-pole affects the control dynamics when the DC-DC converter operates in open-loop control mode, i.e., the duty ratio of the converter is determined by the MPPT-algorithm. Moreover, the RHP-pole sets a constraint for the minimum DC-link capacitance that is required for stable operation. The design rule for the DC-link capacitance is upgraded to match the requirements of two-stage inverters. Moreover, the RHP-pole is effectively removed from the control dynamics when the DC-DC converter is operated under input-voltage control mode. Therefore, the constraint related to the minimum capacitance requirement disappears.

The effect of the phase-locked-loop (PLL) on the small-signal model is analyzed. The model is verified by extracting frequency responses from a switching model and from an experimental prototype operating at reduced voltages. The PLL is shown to cause a negative real part in the q-component of the inverter's output impedance. Such behavior makes the inverter vulnerable to impedance-based interactions which can lead to instability. It is shown that the selection of the PLL's bandwidth is of great significance because it determines the frequency-range at which the impedance behaves as a negative

resistor. An inverter with a wide-bandwidth PLL connected to a grid with large inductance value through a CL-filter is shown to become unstable due to the impedance-based interactions.

The effect of the grid-voltage feedforward is included in the small-signal model. It is shown that an inverter with perfectly tuned feedforward has significantly larger output impedance than an inverter without feedforward. The magnitude of both the d and q-components of the output impedance increases. However, the feedforward does not affect the d-component below the crossover frequency of the DC-link voltage control. Moreover, the feedforward does not affect the q-component below the crossover frequency of the PLL. Altogether, the grid-voltage feedforward is shown to make the inverter more resistant to impedance-based interactions.

6.2 Suggested future research topics

Some future research topics are proposed in the following:

- A conventional sinusoidal pulse-width-modulator is assumed in this thesis. However, many commercial inverters utilize a space-vector modulator which utilizes a measurement from the DC-link voltage. The effect of the space-vector modulator on the small-signal model should be studied. Space-vector modulator creates a feedforward loop from the DC-link voltage when the measured DC-link voltage is used to solve the duration of the switching vectors. The dynamic effect of the feedforward loop has not been extensively reported in the literature.

- The effect of more sophisticated PLLs on the dynamics of the inverter should studied, such as the DSOGI-FLL which provides better performance during unbalanced grid voltages.

- The effect of the grid-voltage feedforward on the output-to-input transfer function of the PV inverter $T_{\text{oi-c-d}}$ should be studied more in detail. The feedforward might, e.g., affect the capacitance requirement of the DC-link since the ripple voltages originating due to unbalanced grid voltages would be attenuated. The ideal feedforward gains for this purpose should be derived.

- The small-signal model of the inverter was simplified in this thesis by assuming that the reactive current component is zero and that the crosscoupling transfer functions can be neglected. However, the multivariable nature of the inverter's small-signal model should be taken into account. For instance, the stability analysis should be done in a case where the cross-couplings are not neglected.

REFERENCES

Abbott, D. (2010). Keeping the energy debate clean: how do we supply the world's energy needs?, *Proceedings of the IEEE* **98**(1): 42–66.

Alawasa, K. M., Mohamed, Y. A.-R. I. and Xu, W. (2014). Active mitigation of subsynchronous interactions between PWM voltage-source converters and power networks, *IEEE Transactions on Power Electronics* **29**(1): 121–134.

Alepuz, S., Bordonau, J. and Peracaula, J. (1999). Dynamic analysis of three-level voltage-source inverters applied to power regulation, *IEEE Power Electronics Specialists Conference* **2**: 721–726.

Alepuz, S., Busquets-monge, S., Bordonau, J., Gago, J., González, D. and Balcells, J. (2006). Interfacing renewable energy sources to the utility grid using a three-level inverter, *IEEE Transactions on Industrial Electronics* **53**(5): 1504–1511.

Azmi, S. A., Adam, G. P., Ahmed, K. H., Finney, S. J. and Williams, B. W. (2013). Grid interfacing of multimegawatt photovoltaic inverters, **28**(6): 2770–2784.

Belkhayat, M. (1997). *Stability Criteria for AC Power Systems With Regulated Loads*, PhD thesis, Purdue University, West Lafayette, NI.

Blaabjerg, F., Aquila, A. and Liserre, M. (2004). Small-signal analysis of single-phase and three-phase dc/ac and ac/dc PWM converters with the frequency-shit technique, *IEEE International Symposium on Industrial Electronics* pp. 1291–1296.

Blaabjerg, F., Chen, Z. and Kjaer, S. B. (2004). Power electronics as efficient interface in dispersed power generation systems, *IEEE Transactions on Power Electronics* **19**(5): 1184–1194.

Bordonau, J., Cosan, M., Borojevic, D., Mao, H. and Lee, F. (1997). A state-space model for the comprehensive dynamic analysis of three-level voltage-source inverters, *IEEE Power Electronics Specialists Conference* pp. 942–948.

Bose, B. K. (2010). Global warming: energy, environmental pollution, and the impact of power electronics, *Industrial Electronics Magazine* (March): 6–17.

Bose, B. K. (2013). Global energy scenario and impact of power electronics in 21st Century, *IEEE Transactions on Industrial Electronics* **60**(7): 2638–2651.

Bratcu, A. I., Munteanu, I., Bacha, S., Picault, D. and Raison, B. (2011). Cascaded dc-dc converter photovoltaic systems: power optimization issues, *IEEE Transactions on Industrial Electronics* **58**(2): 403–411.

Burgos, R., Boroyevich, D., Wang, F., Karimi, K. and Francis, G. (2010). On the ac stability of high power factor three-phase rectifiers, *IEEE Energy Conversion Congress and Exposition* pp. 2047–2054.

Carrasco, J. M., Franquelo, L. G., Bialasiewicz, J. T., Galván, E., Guisado, R. C. P., Ángeles, M., Prats, M., León, J. I. and Moreno-alfonso, N. (2006). Power-electronic systems for the grid integration of renewable energy sources : a survey, *IEEE Transactions on Industrial Electronics* **53**(4): 1002–1016.

Castelló, J. and Espi, J. (2012). DSP implementation for measuring the loop gain frequency response of digitally controlled power converters, *IEEE Transactions on Power Electronics* **27**(9): 4113–4121.

Cavalcanti, M., Farias, A., Oliveira, K. C., Neves, F. A. S. and Afonso, J. L. (2012). Eliminating leakage currents in neutral point clamped inverters for photovoltaic systems, *IEEE Transactions on Industrial Electronics* **59**(1): 435–443.

Cespedes, M. and Sun, J. (2009). Renewable energy systems instability involving grid-parallel inverters, *Applied Power Electronics Conference and Exposition* pp. 1971–1977.

Céspedes, M. and Sun, J. (2011). Modeling and mitigation of harmonic resonance between wind turbines and the grid, *IEEE Energy Conversion Congress and Exposition* pp. 2109–2116.

Cespedes, M. and Sun, J. (2014). Impedance Modeling and Analysis of Grid-Connected Voltage-Source Converters, *Transactions on Power Electronics* **29**(3): 1254 – 1261.

Chen, H.-C. and Lin, W.-J. (2014). MPPT and voltage balancing control with sensing only inductor current for photovoltaic-fed, three-level, boost-type converters, *IEEE Transactions on Power Electronics* **29**(1): 29–35.

Chen, X. and Sun, J. (2011). A study of renewable energy system harmonic resonance based on a DG test-bed, *Twenty-Sixth Annual IEEE Applied Power Electronics Conference and Exposition* pp. 995–1002.

Chen, Y. and Smedley, K. (2008). Three-phase boost-type grid-connected inverter, *IEEE Transactions on Power Electronics* **23**(5): 2301–2309.

Chung, S.-k. (2000). A phase tracking system for three phase utility interface inverters, *IEEE Transactions on Power Electronics* **15**(3): 431–438.

Cvetkovic, I., Jaksic, M., Boroyevich, D., Mattavelli, P., Lee, F., Shen, Z., Ahmed, S. and Dong, D. (2011). Un-terminated, low-frequency terminal-behavioral dq model of

three-phase converters, *IEEE Energy Conversion Congress and Exposition* pp. 791–798.

Dhople, S. V., Ehlmann, J. L., Davoudi, A. and Chapman, P. L. (2010). Multiple-input boost converter to minimize power losses due to partial shading in photovoltaic modules, *IEEE Energy Conversion Congress and Exposition* pp. 2633–2636.

Duesterhoeft, W. C., Schulz, M. W. J. and Clarke, E. (1951). Determination of instantaneous currents and voltages by means of alpha, beta, and zero components, *Transactions of the American Institute of Electrical Engineers* **70**(2): 1248–1255.

Enslin, J. H. R. and Heskes, P. J. M. (2004). Harmonic interaction between a large number of distributed power inverters and the distribution network, *IEEE Transactions on Power Electronics* **19**(6): 1586–1593.

Espí, J. M. and Castelló, J. (2013). Wind turbine generation system with optimized dc-link design and control, *IEEE Transactions on Industrial Electronics* **60**(3): 919–929.

Espinoza, J. R., Jobs, G., Perez, M. and Moran, L. A. (2000). Stability issues in three-phase PWM current/voltage source rectifiers in the regeneration mode, *Proceedings of the IEEE International Symposium on Industrial Electronics* pp. 453–458.

Femia, N., Petrone, G., Spagnuolo, G. and Vitelli, M. (2005). Optimization of perturb and observe maximum power point tracking method, *IEEE Transactions on Power Electronics* **20**(4): 963–973.

Femia, N., Petrone, G., Spagnuolo, G. and Vitelli, M. (2009). A technique for improving P&O MPPT performances of double-stage grid-connected photovoltaic systems, *IEEE Transactions on Industrial Electronics* **56**(11): 4473–4482.

Figueres, E., Garcerá, G., Sandia, J., González-espín, F., Rubio, J. C. and Model, A. A. (2009). Sensitivity study of the dynamics of three-phase photovoltaic inverters with an LCL grid filter, *IEEE Transactions on Industrial Electronics* **56**(3): 706–717.

Gelman, R. (2012). 2012 Renewable Energy Data Book, *National Renewable Energy Laboratory, NREL, Tech. Rep.* pp. 1–128.
URL: *www.nrel.gov*

Golnas, A. (2013). PV system reliability: an operator's perspective, *38th IEEE Photovoltaic Specialists Conference* pp. 1–6.

Gu, B.-g. and Nam, K. (2006). A dc-link capacitor minimization method through direct capacitor current control, *IEEE Transactions on Industry Applications* **42**(2): 573–581.

Gu, B. and Nam, K. (2005). A theoretical minimum DC-link capacitance in PWM converter-inverter systems, *IEE Proceedings on Electric Power Applications* **152**(1): 81–88.

Harnefors, L. (2007). Modeling of three-phase dynamic systems using complex transfer functions and transfer matrices, *IEEE Transactions on Industrial Electronics* **54**(4): 2239–2248.

Harnefors, L., Bongiorno, M. and Lundberg, S. (2007). Input-admittance calculation and shaping for controlled voltage-source converters, *IEEE Transactions on Industrial Electronics* **54**(6): 3323–3334.

Heskes, P. J. M., Myrzik, J. M. a. and Kling, W. L. (2010). Harmonic distortion and oscillatory voltages and the role of negative impedance, *IEEE Power Electronic Society General Meeting* pp. 1–7.

Hiti, S., Boroyevich, D. and Cuadros, C. (1994). Small-signal modeling and control of three-phase PWM converters, *IEEE Industry Applications Society Annual Meeting* pp. 1143–1150.

Hiti, S., Vlatkovic, V., Borojevic, D. and Lee, F. (1994). A new control algorithm for three- phase pwm buck rectifier with input displacement factor compensation, *IEEE Transactions on Power Electronics* **9**(2): 173–180.

Ho, C. N.-m., Breuninger, H., Pettersson, S., Escobar, G. and Canales, F. (2013). A comparative performance study of an interleaved boost converter using commercial Si and SiC diodes for PV applications, *IEEE Transactions on Power Electronics* **28**(1): 289–299.

Hohm, D. and Ropp, M. (2000). Comparative study of maximum power point tracking algorithms using an experimental, programmable, maximum power point tracking test bed, *Twenty-Eighth IEEE Photovoltaic Specialists Conference* pp. 1699–1702.

Huang, J., Corzine, K. A. and Belkhayat, M. (2009). Small-signal impedance measurement of power-electronics-based ac power systems using line-to-line current injection, *IEEE Transactions on Power Electronics* **24**(2): 445–455.

Huang, S., Kong, L., Wei, T. and Zhang, G. (2008). Comparative analysis of PI decoupling control strategies with or without feed-forward in SRF for three-phase power supply, *International Conference on Electrical Machines and Systems* pp. 2372–2377.

Huang, Y., Shen, M., Peng, F. Z. and Wang, J. (2006). Z-source inverter for residential photovoltaic systems, *IEEE Transactions on Power Electronics* **21**(6): 1776–1782.

Jain, S. and Agarwal, V. (2007). A single-stage grid connected inverter topology for solar PV systems with maximum power point tracking, *IEEE Transactions on Power Electronics* **22**(5): 1928–1940.

Ji, Y.-H., Jung, D.-Y., Kim, J.-G., Kim, J.-H., Lee, T.-W. and Won, C.-Y. (2011). A real maximum power point tracking method for mismatching compensation in PV array under partially shaded conditions, *IEEE Transactions on Power Electronics* **26**(4): 1001–1009.

Jung, D.-Y., Ji, Y.-H., Park, S.-H., Jung, Y.-C. and Won, C.-Y. (2011). Interleaved soft-switching boost converter for photovoltaic power-generation system, *IEEE Transactions on Power Electronics* **26**(4): 1137–1145.

Karanayil, B., Agelidis, V. G. and Pou, J. (2013). Evaluation of dc-link decoupling using electrolytic or polypropylene film capacitors in three-phase grid-connected photovoltaic inverters, *39th Annual Conference of the IEEE Industrial Electronics Society* pp. 6980–6986.

Kjaer, S. B., Pedersen, J. K. and Blaabjerg, F. (2002). Power inverter topologies for photovoltaic modules-a review, *IEEE Industry Applications Conference* pp. 782–788.

Kolar, J. W., Friedli, T., Krismer, F., Looser, A., Schweizer, M., Friedemann, R. A., Steimer, P. K. and Bevirt, J. B. (2013). Conceptualization and multiobjective optimization of the electric system of an airborne wind turbine, *IEEE Journal of Emerging and Selected Topics in Power Electronics* **1**(2): 73–103.

Kotsopoulus, A., Duarte, J. L. and Hendrix, M. A. M. (2001). A predictive control scheme for DC voltage and AC current in grid-connected photovoltaic inverters with minimum DC link capacitance, *27th Annual Conference of the IEEE Industrial Electronics Society* pp. 1994–1999.

Krein, P. T., Balog, R. S. and Mirjafari, M. (2012). Minimum energy and capacitance requirements for single-phase inverters and rectifiers using a ripple port, *IEEE Transactions on Power Electronics* **27**(11): 4690–4698.

Ledwich, G. and Sharma, H. (2000). Connection of inverters to a weak grid, *IEEE 31st Power Electronics Specialists Conference* pp. 1018–1022.

Leppäaho, J., Nousiainen, L., Puukko, J., Huusari, J. and Suntio, T. (2010). Implementing current-fed converters by adding an input capacitor at the input of voltage-fed converter for interfacing solar generator, *International Power Electronics and Motion Conference* pp. 81–88.

Leppäaho, J. and Suntio, T. (2011). Dynamic properties of PCM-controlled current-fed boost converter in photovoltaic system interfacing, *14th European Conference on Power Electronics and Applications* pp. 1–10.

Li, W., Pan, D., Ruan, X. and Wang, X. (2011). A full-feedforward scheme of grid voltages for a three-phase grid-connected inverter with an LCL filter, *IEEE Energy Conversion Congress and Exposition* pp. 96–103.

Liserre, M., Blaabjerg, F. and Hansen, S. (2005). Design and control of an LCL-filter-based three-phase active rectifier, *IEEE Transactions on Industry Applications* **41**(5): 1281–1291.

Liserre, M., Orabana, V. E., Teodorescu, R. and Blaabjerg, F. (2004). Stability of grid-connected PV inverters with large grid impedance variation, *Twenty-Eighth Annual IEEE Applied Power Electronics Conference and Exposition* pp. 1–6.

Liserre, M., Teodorescu, R. and Blaabjerg, F. (2006). Stability of photovoltaic and wind turbine grid-connected inverters for a large set of grid impedance values, *IEEE Transactions on Power Electronics* **21**(1): 263–272.

Lo Brano, V., Orioli, A., Ciulla, G. and Di Gangi, A. (2010). An improved five-parameter model for photovoltaic modules, *Solar Energy Materials and Solar Cells* **94**(8): 1358–1370.

Luoma, J., Kleissl, J. and Murray, K. (2011). Optimal inverter sizing considering cloud enhancement, *Solar Energy* **86**(1): 421–429.

MacFarlane, A. G. J. and Postlethwaite, I. (1977). The generalized Nyquist stability criterion and multivariable root loci, *International Journal of Control* **25**(1): 81–127.

Mao, H., Boroyevich, D. and Lee, F. (1998). Novel reduced-order small-signal model of a three-phase PWM rectifier and its application in control design and system analysis, *IEEE Transactions on Power Electronics* **13**(3): 511–521.

Martin, D., Nam, I., Siegers, J. and Santi, E. (2013). Wide bandwidth three-phase impedance identification using existing power electronics inverter, *Applied Power Electronics Conference and Exposition* pp. 334–341.

Messo, T., Jokipii, J., Mäkinen, A. and Suntio, T. (2013). Modeling the grid synchronization induced negative-resistor-like behavior in the output impedance of a three-phase photovoltaic inverter, *4th IEEE International Symposium on Power Electronics for Distributed Generation Systems, PEDG´13* pp. 1–8.

Messo, T., Jokipii, J., Puukko, J. and Suntio, T. (2014). Determining the value of dc-link capacitance to ensure stable operation of a three-phase photovoltaic inverter, *IEEE Transactions on Power Electronics* **29**(2): 665–673.

Messo, T., Jokipii, J. and Suntio, T. (2012). Steady-state and dynamic properties of boost-power-stage converter in photovoltaic applications, *3rd IEEE International Symposium on Power Electronics for Distributed Generation Systems, PEDG´12* pp. 1–7.

Messo, T., Jokipii, J. and Suntio, T. (2013). Minimum dc-link capacitance requirement of a two-stage photovoltaic inverter, *IEEE Energy Conversion Congress & Exposition, ECCE´13* pp. 999–1006.

Messo, T., Jokipii, J. and Suntio, T. (2014). Effect of conventional grid-voltage feedforward on the output impedance of a three-phase PV inverter, *International Power Electronics Conference, ECCE-ASIA* pp. 1–8.

Messo, T., Puukko, J. and Suntio, T. (2012). Effect of MPP-tracking dc/dc converter on VSI-based photovoltaic inverter dynamics, *IET Power Electronics, Machines and Drives Conference, PEMD´12* pp. 1–6.

Middlebrook, R. D. (1978). Design techniques for preventing input-filter oscillations in switched-mode regulators, *Fifth National Solid-State Power Conversion Conference* pp. 153–168.

Middlebrook, R. D. and Slobodan, C. (1976). A general unified approach to modelling switching-converter power stages, *IEEE Power Electronics Specialists Conference* pp. 18–34.

Miret, J., Castilla, M., Camacho, A., Vicuña, L. G. D. and Matas, J. (2012). Control scheme for photovoltaic three-phase inverters to minimize peak currents during unbalanced grid-voltage sags, *IEEE Transactions on Power Electronics* **27**(10): 4262–4271.

Nousiainen, L., Puukko, J., Mäki, A., Messo, T., Huusari, J., Jokipii, J., Viinamäki, J., Lobera, D. T., Valkealahti, S. and Suntio, T. (2013). Photovoltaic generator as an input source for power electronic converters, *IEEE Transactions on Power Electronics* **28**(6): 3028–3038.

Park, B.-j., Choi, K.-y. and Kim, R.-y. (2013). An active feedforward compensation for a current harmonics reduction in three-phase grid-connected inverters, *39th Annual Conference of the IEEE Industrial Electronics Society* pp. 400–405.

Park, R. H. (1929). Two-reaction theory of synchronous machines: generalized method of analysis - part I, *Transactions of the American Institute of Electrical Engineers* **48**(3): 194–194.

Park, S.-y., Member, S., Chen, C.-l. and Lai, J.-s. (2008). Admittance compensation in current loop control for a grid-tie LCL fuel cell inverter, *IEEE Transactions on Power Electronics* **23**(4): 1716–1723.

Petrone, G., Spagnuolo, G., Teodorescu, R., Veerachary, M. and Vitelli, M. (2008). Reliability issues in photovoltaic power processing systems, *IEEE Transactions on Industrial Electronics* **55**(7): 2569–2580.

Puukko, J., Messo, T., Nousiainen, L., Huusari, J. and Suntio, T. (2011). Negative output impedance in three-phase grid connected renewable energy source inverters based on reduced-order model, *IET Conference on Renewable Power Generation* pp. 73–73.

Puukko, J., Messo, T. and Suntio, T. (2011). Effect of photovoltaic generator on a typical VSI-based three-phase grid-connected photovoltaic inverter dynamics, *IET Conference on Renewable Power Generation, RPG´11* pp. 1–6.

Puukko, J., Nousiainen, L. and Suntio, T. (2011). Effect of minimizing input capacitance in VSI-based renewable energy source converters, *33rd IEEE International Telecommunications Energy Conference* pp. 1–9.

Rim, C. I., Hu, D. Y. and Cho, G. H. (1990). Transformers as equivalent circuits for switches: general proofs and d-q transformation-based analyses, *IEEE Transactions on Industry Applications* **26**(4): 777–785.

Rockhill, A. A., Liserre, M., Teodorescu, R. and Rodriguez, P. (2011). Grid-filter design for a multimegawatt medium-voltage voltage-source inverter, *IEEE Transactions on Industrial Electronics* **58**(4): 1205–1217.

Roinila, T., Vilkko, M. and Suntio, T. (2010). Frequency-response measurement of switched-mode power supplies in the presence of nonlinear distortions, *IEEE Transactions on Power Electronics* **25**(8): 2179–2187.

Sahan, B., Vergara, A. N., Henze, N., Engler, A. and Zacharias, P. (2008). A single-stage PV module integrated converter based on a low-power current-source inverter, *IEEE Transactions on Industrial Electronics* **55**(7): 2602–2609.

Shen, Z., Jaksic, M. and Mattavelli, P. (2013). Design and implementation of three-phase ac impedance measurement unit (IMU) with series and shunt injection, *Twenty-Eighth Annual IEEE Applied Power Electronics Conference and Exposition* pp. 2674–2681.

Shen, Z., Jaksic, M., Zhou, B. and Mattavelli, P. (2013). Analysis of phase locked loop (PLL) influence on dq impedance measurement in three-phase AC systems, *Twenty-Eighth Annual IEEE Applied Power Electronics Conference and Exposition* pp. 939–945.

Sun, J. (2009). Small-signal methods for ac distributed power systems - a review, *IEEE Transactions on Power Electronics* **24**(11): 2545–2554.

Sun, J. (2011). Impedance-based stability criterion for grid-connected inverters, *IEEE Transactions on Power Electronics* **26**(11): 3075–3078.

Timbus, A., Liserre, M., , Teodorescu, R., Rodriguez, P. and Blaabjerg, F. (2009). Evaluation of current controllers for distributed power generation systems, *IEEE Transactions on Power Electronics* **24**(3): 654–664.

Torres Lobera, D. and Valkealahti, S. (2013). Dynamic thermal model of solar PV systems under varying climatic conditions, *Solar Energy* **93**: 183–194.

Tse, C. K. (1998). *Linear Circuit Analysis*, Addison Wesley Longman, Harlow, England.

Urtasun, A., Sanchis, P. and Marroyo, L. (2013). Adaptive voltage control of the dc/dc boost stage in PV converters with small input capacitor, *IEEE Transactions on Power Electronics* **28**(11): 5038–5048.

Vighetti, S., Ferrieux, J.-P. and Lembeye, Y. (2012). Optimization and design of a cascaded dc/dc converter devoted to grid-connected photovoltaic systems, *IEEE Transactions on Power Electronics* **27**(4): 2018–2027.

Villalva, M., de Siqueira, T. and Ruppert, E. (2010). Voltage regulation of photovoltaic arrays: small-signal analysis and control design, *IET Power Electronics* **3**(6): 869.

Visscher, K. and Heskes, P. (2005). A method for operational grid and load impedance measurements, *International Conference on Future Power Systems* pp. 1–4.

Wang, F., Duarte, J. L., Hendrix, M. and Ribeiro, P. (2011). Modeling and analysis of grid harmonic distortion impact of aggregated DG inverters, *IEEE Transactions on Power Electronics* **26**(3): 786–797.

Wen, B., Boroyevich, D., Burgos, R. and Mattavelli, P. (2013). Input impedance of voltage source converter with stationary frame linear current regulators and phase-locked loop, *2013 IEEE Energy Conversion Congress and Exposition* pp. 4207–4213.

Wen, B., Boroyevich, D., Mattavelli, P., Shen, Z. and Burgos, R. (2012). Experimental verification of the Generalized Nyquist stability criterion for balanced three-phase ac systems in the presence of constant power loads, *IEEE Energy Conversion Congress and Exposition* pp. 3926–3933.

Wyatt, J. L. and Chua, L. O. (1983). Nonlinear resistive maximum power theorem, with solar cell application, *IEEE Tranasactions on Circuits and Systems* **C**(11): 824–828.

Xiao, W., Dunford, W., Palmer, P. and Capel, A. (2007). Regulation of photovoltaic voltage, *IEEE Transactions on Industrial Electronics* **54**(3): 1365–1374.

Xiao, W., Ozog, N. and Dunford, W. G. (2007). Topology study of photovoltaic interface for maximum power point tracking, *IEEE Transactions on Industrial Electronics* **54**(3): 1696–1704.

Xue, M., Zhang, Y., Kang, Y., Yi, Y., Li, S. and Liu, F. (2012). Full feedforward of grid voltage for discrete state feedback controlled grid-connected inverter with LCL filter, *IEEE Transactions on Power Electronics* **27**(10): 4234–4247.

Yang, B., Zhao, Y. and He, X. (2010). Design and analysis of a grid-connected photovoltaic power system, *IEEE Transactions on Power Electronics* **25**(4): 992–1000.

Yazdani, A., Rita, A., Fazio, D., Ghoddami, H., Russo, M., Kazerani, M., Jatskevich, J., Strunz, K., Leva, S. and Martinez, J. A. (2011). Modeling guidelines and a benchmark for power system simulation studies of three-phase single-stage photovoltaic systems, *IEEE Transactions on Power Delivery* **26**(2): 1247–1264.

Zhang, S., Jiang, S., Lu, X., Ge, B. and Peng, F. Z. (2014). Resonance issues and damping techniques for grid-connected inverters with long transmission cable, *IEEE Transactions on Power Electronics* **29**(1): 110–120.

A TRANSFER FUNCTIONS OF THE DC-DC CONVERTER

The transfer functions of the voltage-boosting DC-DC converter at open loop are as given in (A.1)–(A.7).

$$Z_{\text{in-o}} = \frac{1}{L_1 C_1} \left(L_1 s + R_1 - r_{\text{C1}}\right) \left(r_{\text{C1}} C_1 s + 1\right) \frac{1}{\Delta^{\text{DC-DC}}} \tag{A.1}$$

$$T_{\text{oi-o}} = \frac{D'}{L_1 C_1} \left(r_{\text{C1}} C_1 s + 1\right) \frac{1}{\Delta^{\text{DC-DC}}} \tag{A.2}$$

$$G_{\text{ci-o}} = -\frac{\left(U_{\text{dc}} + U_{\text{D}}\right)}{L_1 C_1} \left(r_{\text{C1}} C_1 s + 1\right) \frac{1}{\Delta^{\text{DC-DC}}} \tag{A.3}$$

$$G_{\text{io-o}} = \frac{D'}{L_1 C_1} \left(r_{\text{C1}} C_1 s + 1\right) \frac{1}{\Delta^{\text{DC-DC}}} \tag{A.4}$$

$$Y_{\text{o-o}} = \frac{D^{'2}}{L_1} s \frac{1}{\Delta^{\text{DC-DC}}} \tag{A.5}$$

$$G_{\text{co-o}} = -I_{\text{pv}} \left(s^2 - \frac{1}{L_1} \left(\frac{D' \left(U_{\text{dc}} + U_{\text{D}}\right)}{I_{\text{pv}}} - R_1\right) s - \frac{1}{L_1 C_1}\right) \frac{1}{\Delta^{\text{DC-DC}}} \tag{A.6}$$

$$\Delta^{\text{DC-DC}} = s^2 + \frac{R_1}{L_1} s + \frac{1}{L_1 C_1} \tag{A.7}$$

B TRANSFER FUNCTIONS OF A THREE-PHASE PV INVERTER

Transfer functions of a three-phase photovoltaic inverter are given in (B.1)–(B.16) without the parasitic resistances of the switches, DC-link capacitor and the inductors.

$$Z_{\text{in}} = \frac{1}{C_{\text{dc}}} \left(s^2 + \omega_{\text{s}}^2\right) \frac{1}{\Delta^{\text{DC-AC}}} \tag{B.1}$$

$$T_{\text{oi-d}} = \frac{3D_{\text{d}}}{2C_{\text{dc}}L} \left(s - \frac{D_{\text{q}}}{D_{\text{d}}}\omega_{\text{s}}\right) \frac{1}{\Delta^{\text{DC-AC}}} \tag{B.2}$$

$$T_{\text{oi-q}} = \frac{3D_{\text{q}}}{2C_{\text{dc}}L} \left(s + \frac{D_{\text{d}}}{D_{\text{q}}}\omega_{\text{s}}\right) \frac{1}{\Delta^{\text{DC-AC}}} \tag{B.3}$$

$$G_{\text{ci-d}} = -\frac{I_{\text{dc}}}{C_{\text{dc}}D_{\text{d}}} s \left(s + \frac{3U_{\text{dc}}D_{\text{d}}^2}{2I_{\text{dc}}L}\right) \frac{1}{\Delta^{\text{DC-AC}}} \tag{B.4}$$

$$G_{\text{ci-q}} = -\frac{\omega_{\text{s}}I_{\text{dc}}}{C_{\text{dc}}D_{\text{d}}} \left(s + \frac{3U_{\text{dc}}D_{\text{d}}^2}{2I_{\text{dc}}L}\right) \frac{1}{\Delta^{\text{DC-AC}}} \tag{B.5}$$

$$G_{\text{io-d}} = \frac{D_{\text{d}}}{C_{\text{dc}}L} \left(s + \frac{D_{\text{q}}}{D_{\text{d}}}\omega_{\text{s}}\right) \frac{1}{\Delta^{\text{DC-AC}}} \tag{B.6}$$

$$Y_{\text{o-d}} = \frac{1}{L} \left(s^2 + \frac{3D_{\text{q}}^2}{2C_{\text{dc}}L}\right) \frac{1}{\Delta^{\text{DC-AC}}} \tag{B.7}$$

$$Y_{\text{o-qd}} = \frac{\omega_{\text{s}}}{L} \left(s - \frac{I_{\text{dc}}}{C_{\text{dc}}U_{\text{dc}}}\right) \frac{1}{\Delta^{\text{DC-AC}}} \tag{B.8}$$

$$G_{\text{co-d}} = \frac{U_{\text{dc}}}{L} s \left(s - \frac{I_{\text{dc}}}{C_{\text{dc}}U_{\text{dc}}}\right) \frac{1}{\Delta^{\text{DC-AC}}} \tag{B.9}$$

$$G_{\text{co-qd}} = \frac{U_{\text{dc}}\omega_{\text{s}}}{L} \left(s - \frac{I_{\text{dc}}}{C_{\text{dc}}U_{\text{dc}}}\right) \frac{1}{\Delta^{\text{DC-AC}}} \tag{B.10}$$

$$G_{\text{io-q}} = \frac{D_{\text{q}}}{C_{\text{dc}}L}\left(s - \frac{D_{\text{d}}}{D_{\text{q}}}\omega_{\text{s}}\right)\frac{1}{\Delta^{\text{DC-AC}}} \tag{B.11}$$

$$Y_{\text{o-dq}} = -\frac{\omega_{\text{s}}}{L}\left(s + \frac{I_{\text{dc}}}{C_{\text{dc}}U_{\text{dc}}}\right)\frac{1}{\Delta^{\text{DC-AC}}} \tag{B.12}$$

$$Y_{\text{o-q}} = \frac{1}{L}\left(s^2 + \frac{3D_{\text{d}}^2}{2C_{\text{dc}}L}\right)\frac{1}{\Delta^{\text{DC-AC}}} \tag{B.13}$$

$$G_{\text{co-dq}} = -\omega_{\text{s}}s\left(\frac{U_{\text{dc}}}{L} + \frac{2I_{\text{dc}}^2}{3C_{\text{dc}}D_{\text{d}}^2U_{\text{dc}}}\right)\frac{1}{\Delta^{\text{DC-AC}}} \tag{B.14}$$

$$G_{\text{co-q}} = \frac{U_{\text{dc}}}{L}\left(s^2 + \frac{3D_{\text{d}}^2}{2C_{\text{dc}}L}\right)\frac{1}{\Delta^{\text{DC-AC}}} \tag{B.15}$$

$$\Delta^{\text{DC-AC}} = s\left(s^2 + \frac{3\left(D_{\text{d}}^2 + D_{\text{q}}^2\right)}{2C_{\text{dc}}L} + \omega_{\text{s}}\right) \tag{B.16}$$

C TRANSFER FUNCTIONS OF A THREE-PHASE CL-FILTER

The transfer functions of the three-phase CL-filter are given in (C.1)–(C.17) without parasitic resistances.

$$Z_{\text{in-d}} = (R_{\text{d}}C_{\text{f}}s + 1)\left[\frac{s}{C_{\text{f}}}\left(\omega_{\text{s}}^2 + s^2\right) + \frac{1}{C_{\text{f}}^2 L_{\text{f}}}\left(R_{\text{d}}C_{\text{f}}s^2 + s + R_{\text{d}}C_{\text{f}}\omega_{\text{s}}^2\right)\right]\frac{1}{\Delta^{\text{f}}} \tag{C.1}$$

$$Z_{\text{in-qd}} = \frac{\omega_{\text{s}}}{C_{\text{f}}}(R_{\text{d}}C_{\text{f}}s + 1)\left(s^2 + \omega_{\text{s}}^2 - \frac{1}{C_{\text{f}}L_{\text{f}}}\right)\frac{1}{\Delta^{\text{f}}} \tag{C.2}$$

$$Z_{\text{in-dq}} = -\frac{\omega_{\text{s}}}{C_{\text{f}}}(R_{\text{d}}C_{\text{f}}s + 1)\left(s^2 + \omega_{\text{s}}^2 - \frac{1}{C_{\text{f}}L_{\text{f}}}\right)\frac{1}{\Delta^{\text{f}}} \tag{C.3}$$

$$Z_{\text{in-q}} = (R_{\text{d}}C_{\text{f}}s + 1)\left[\frac{s}{C_{\text{f}}}\left(\omega_{\text{s}}^2 + s^2\right) + \frac{1}{C_{\text{f}}^2 L_{\text{f}}}\left(R_{\text{d}}C_{\text{f}}s^2 + s + R_{\text{d}}C_{\text{f}}\omega_{\text{s}}^2\right)\right]\frac{1}{\Delta^{\text{f}}} \tag{C.4}$$

$$T_{\text{oi-d}} = \frac{(R_{\text{d}}C_{\text{f}}s + 1)}{C_{\text{f}}^2 L_{\text{f}}^2}\left[(R_{\text{d}}C_{\text{f}}s + 1) + L_{\text{f}}C_{\text{f}}\left(s^2 - \omega_{\text{s}}^2\right)\right]\frac{1}{\Delta^{\text{f}}} \tag{C.5}$$

$$T_{\text{oi-qd}} = \frac{\omega_{\text{s}}}{C_{\text{f}}L_{\text{f}}^2}(R_{\text{d}}C_{\text{f}}s + 1)(2L_{\text{f}}s + R_{\text{d}})\frac{1}{\Delta^{\text{f}}} \tag{C.6}$$

$$T_{\text{oi-dq}} = -\frac{\omega_{\text{s}}}{C_{\text{f}}L_{\text{f}}^2}(R_{\text{d}}C_{\text{f}}s + 1)(2L_{\text{f}}s + R_{\text{d}})\frac{1}{\Delta^{\text{f}}} \tag{C.7}$$

$$T_{\text{oi-q}} = \frac{(R_{\text{d}}C_{\text{f}}s + 1)}{C_{\text{f}}^2 L_{\text{f}}^2}\left[(R_{\text{d}}C_{\text{f}}s + 1) + L_{\text{f}}C_{\text{f}}\left(s^2 - \omega_{\text{s}}^2\right)\right]\frac{1}{\Delta^{\text{f}}} \tag{C.8}$$

$$G_{\text{io-d}} = \left[\frac{R_{\text{d}}}{L_{\text{f}}}\left(s^3 + \frac{R_{\text{d}}}{L_{\text{f}}}s^2 + \omega_{\text{s}}^2 s + \frac{R_{\text{d}}}{L_{\text{f}}}\omega_{\text{s}}^2\right) + \frac{1}{C_{\text{f}}L_{\text{f}}}\left(s^2 + \frac{2R_{\text{d}}}{L_{\text{f}}}s + \frac{1}{C_{\text{f}}L_{\text{f}}} - \omega_{\text{s}}^2\right)\right]\frac{1}{\Delta^{\text{f}}} \tag{C.9}$$

$$G_{\text{io-qd}} = \frac{\omega_{\text{s}} R_{\text{d}}}{L_{\text{f}}} \left(s^2 + \frac{2}{C_{\text{f}} R_{\text{d}}} s + \omega_{\text{s}}^2 \right) \frac{1}{\Delta^{\text{f}}} \tag{C.10}$$

$$G_{\text{io-dq}} = -\frac{\omega_{\text{s}} R_{\text{d}}}{L_{\text{f}}} \left(s^2 + \frac{2}{C_{\text{f}} R_{\text{d}}} s + \omega_{\text{s}}^2 \right) \frac{1}{\Delta^{\text{f}}} \tag{C.11}$$

$$G_{\text{io-q}} = \left[\frac{R_{\text{d}}}{L_{\text{f}}} \left(s^3 + \frac{R_{\text{d}}}{L_{\text{f}}} s^2 + \omega_{\text{s}}^2 s + \frac{R_{\text{d}}}{L_{\text{f}}} \omega_{\text{s}}^2 \right) + \frac{1}{C_{\text{f}} L_{\text{f}}} \left(s^2 + \frac{2R_{\text{d}}}{L_{\text{f}}} s + \frac{1}{C_{\text{f}} L_{\text{f}}} - \omega_{\text{s}}^2 \right) \right] \frac{1}{\Delta^{\text{f}}} \tag{C.12}$$

$$Y_{\text{o-d}} = \frac{1}{L_{\text{f}}} \left(s^3 + \frac{R_{\text{d}}}{L_{\text{f}}} s^2 + \left(\frac{1}{C_{\text{f}} L_{\text{f}}} + \omega_{\text{s}}^2 \right) s + \frac{\omega_{\text{s}}^2 R_{\text{d}}}{L_{\text{f}}} \right) \frac{1}{\Delta^{\text{f}}} \tag{C.13}$$

$$Y_{\text{o-qd}} = \frac{\omega_{\text{s}}}{L_{\text{f}}} \left(s^2 + \omega_{\text{s}}^2 - \frac{1}{C_{\text{f}} L_{\text{f}}} \right) \frac{1}{\Delta^{\text{f}}} \tag{C.14}$$

$$Y_{\text{o-dq}} = -\frac{\omega_{\text{s}}}{L_{\text{f}}} \left(s^2 + \omega_{\text{s}}^2 - \frac{1}{C_{\text{f}} L_{\text{f}}} \right) \frac{1}{\Delta^{\text{f}}} \tag{C.15}$$

$$Y_{\text{o-q}} = \frac{1}{L_{\text{f}}} \left(s^3 + \frac{R_{\text{d}}}{L_{\text{f}}} s^2 + \left(\frac{1}{C_{\text{f}} L_{\text{f}}} + \omega_{\text{s}}^2 \right) s + \frac{\omega_{\text{s}}^2 R_{\text{d}}}{L_{\text{f}}} \right) \frac{1}{\Delta^{\text{f}}} \tag{C.16}$$

$$\Delta^{\text{f}} = s^4 + k_3 s^3 + k_2 s^2 + k_1 s + k_0, \tag{C.17}$$

where

$$\begin{aligned} k_3 &= \frac{2R_{\text{d}}}{L_{\text{f}}} \\ k_2 &= \frac{R_{\text{d}}^2}{L_{\text{f}}^2} + \frac{1}{C_{\text{f}} L_{\text{f}}} + 2\omega_{\text{s}}^2 \\ k_1 &= \frac{R_{\text{d}}}{L_{\text{f}}} \left(\frac{1}{C_{\text{f}} L_{\text{f}}} + 2\omega_{\text{s}}^2 \right) \\ k_0 &= \frac{1}{C_{\text{f}}^2 L_{\text{f}}^2} - \frac{2\omega_{\text{s}}^2}{C_{\text{f}} L_{\text{f}}} + \frac{R_{\text{d}}^2 \omega_{\text{s}}^2}{L_{\text{f}}^2} + \omega_{\text{s}}^4. \end{aligned} \tag{C.18}$$

D LABORATORY SETUP

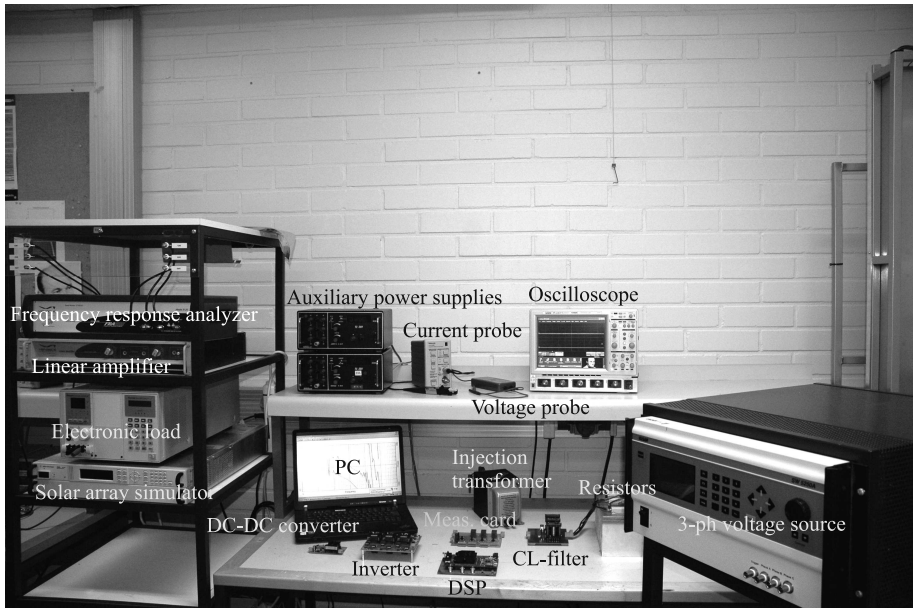

Fig. D.1: Laboratory setup.

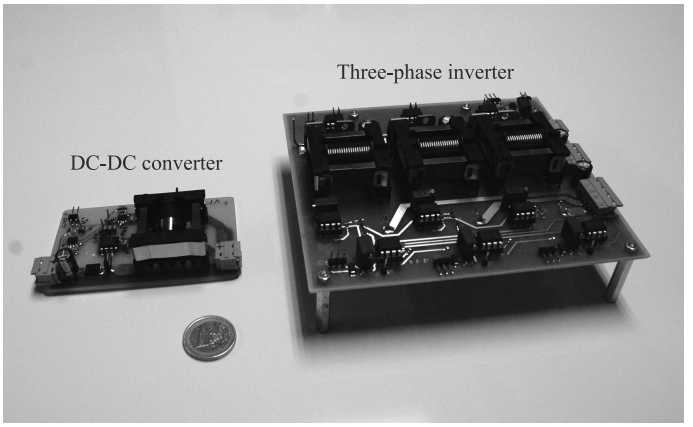

Fig. D.2: Experimental converters.

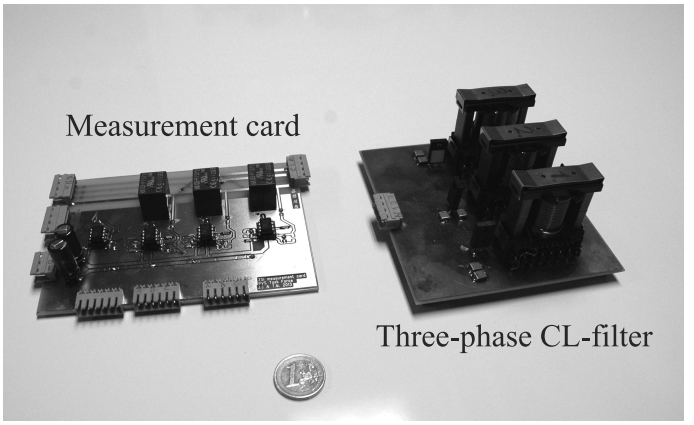

Fig. D.3: Measurement card and three-phase CL-filter.

Tampereen teknillinen yliopisto
PL 527
33101 Tampere

Tampere University of Technology
P.O.B. 527
FI-33101 Tampere, Finland

ISBN 978-952-15-3325-9
ISSN 1459-2045